2-2023

New Porous Nanomaterials For Battery and Supercapacitor

Yixian Pei

NEW POROUS NANOMATERIALS FOR BATTERY AND SUPERCAPACITOR APPLICATIONS

by

Yixian Pei, B.S.

A Dissertation Presented in Partial Fulfillment
of the Requirements of the Degree
Doctor of Philosophy

COLLEGE OF ENGINEERING AND SCIENCE
LOUISIANA TECH UNIVERSITY

February 2023

LOUISIANA TECH UNIVERSITY

GRADUATE SCHOOL

October 7, 2022
Date of dissertation defense

We hereby recommend that the dissertation prepared by

Yixian Pei, B.S.

entitled **New Porous Nanomaterials**

For Battery and Supercapacitor

Applications

be accepted in partial fulfillment of the requirements for the degree of

Doctor of Philosophy in Engineering, Micro & Nanoscale Systems Conc.

Shengnian Wang
Supervisor of Dissertation Research

Shengnian Wang
Head of Engineering

Doctoral Committee Members:
Dr. Yuri Lvov
Dr. Adarsh Radadia
Dr. Nan Nan
Dr. Prabhu Arumugam

Approved:
Hisham Hegab
Dean of Engineering & Science

Approved:
Ramu Ramachandran
Dean of the Graduate School

ABSTRACT

Lithium-Sulfur batteries have a high energy storage capacity while their sulfur cathode suffers large volume change, polysulfides dissolution and shuttle effect, and capacity fading during long-term cycling. To help lock sulfur and mitigate these problems, we introduced halloysite, a natural clay material with a nanotube format, to disperse and confine sulfur nanoparticles as well as to suppress the dissolution and migration of polysulfides. Halloysite was made conductive by covering it with a glucose-derived carbon skin. Sulfur nanoparticles were then trapped in both the lumen and outside surface of individual nanotubes with a loading dosage up to 80 %. In this new halloysite/sulfur composites cathode, the hollow nanostructure of halloysite provides space to allow dimension changes of encapsulated sulfur nanoparticles during repeated lithiation while limiting their size up to the diameter of nanotube lumen (i.e., 25 nm or less). The stacked halloysite clusters further create many nanoscale voids to divide the sulfur-electrolyte interface into isolated domains and increase the migration tortuosity in electrolytes to suppress the dissolution and shuttle effect of polysulfides. These features together contribute to improved cycling stability, retaining nearly ~84% of the starting capacity over 250 cycles, though the diffusion of lithium ions going in and out of nanotubes show some differences.

In project 2, we worked on the anode development for LIBs. Silicon-rich (e.g., >30 wt.%) anodes are desired to leverage the current capacity of lithium-ion batteries (LIBs) towards commercial cell performance requirements in critical markets, such as the transportation sector. A new type of nanofiber-in-microfiber silicon/carbon composite electrode was prepared and

tested as a potential silicon-rich anode candidate. A co-axial electrospinning setup was used to produce a unique hybrid composite fiber configuration, in which silicon nanoparticles were suspended in a polymer solution to serve as the middle stream while the sheath stream was comprised of another polymer solution. Polyvinyl alcohol (PVA) was chosen as the silicon dispersion fluid because of its limited viscosity increase even at a very high solid allowance, which after carbonization held those nanoparticles together as short, branched nanofibers. Polyacrylonitrile (PAN) sheath fluid helped wrap the formed short, silicon-rich nanofiber bundles to form a nonwoven, ductile microfiber mat. After being carbonized into composite anodes, the silicon-rich nanofibers were used to host the majority of lithium ions while their thin carbon skin, originating from carbonized PVA, promotes conductivity and charge transfer. The nanofibrous morphology and the mesoscale space in between help accommodate the notorious volume expansion issues in silicon anodes during lithiation/delithiation processes. The outside PAN-derived microfibers provide structural support for the encapsulated silicon-rich nanofibers and simultaneously serve as the three-dimensional current collector. The new composite anodes were confirmed on their unique fibrous configuration and improved electrochemical performance. With 40 wt% Si, such silicon-rich, nanofiber-in-microfiber anodes achieve ~900 $mAhg^{-1}$ reversible capacity and ~90% capacity retention over 250 cycles by effectively balancing challenges on silicon-rich fibrous anode and electrode pulverization.

Beside battery research, we also worked on supercapacitors with high power density in project 3. Despite the great benefits plastics have brought to our modern lives, a large volume of plastic wastes increasingly threatens our environment and human health. Through a hydrothermal carbonization and crystallization process involving nitric acid and ethanol, drinking bottles made of polyethylene terephthalate were successfully converted into carbon

quantum dots (CQDs) and thin carbon sheets simultaneously, with the former well dispersed and intercalated in the latter as a ball-sheet carbon structure (BSCs). The formed unique, connected, and conductive carbon network allows rapid transport of ions and electrons besides their large surface area and numerous ion hosting sites. The electrodes made of such a plastic ball-sheet carbon structure (PBSCs) therefore exhibit pseudocapacitance behavior with the specific capacity reaching 237 F/g at the charge rate of 1 A/g. Superior cycling stability on the energy storage was also found. Our method offers a new avenue to upcycle some plastic wastes as valuable energy storage systems, to help boost the recycling of plastic waste, and move forwards to the sustainable deployment of various clean energy resources.

APPROVAL FOR SCHOLARLY DISSEMINATION

The author grants to the Prescott Memorial Library of Louisiana Tech University the right to reproduce, by appropriate methods, upon request, any or all portions of this Dissertation. It is understood that "proper request" consists of the agreement, on the part of the requesting party, that said reproduction is for his personal use and that subsequent reproduction will not occur without written approval of the author of this Dissertation. Further, any portions of the Dissertation used in books, papers, and other works must be appropriately referenced to this Dissertation.

Finally, the author of this Dissertation reserves the right to publish freely, in the literature, at any time, any or all portions of this Dissertation.

Author _____

Date _____

DEDICATION

Thanks to my parents, Pei Zhenan and Zhang Suying, who supported me in all aspects and encouraged me to face any challenges.

Thanks to my academic adviser, Dr. Shengnian Wang, who guided me in this interesting research experience, especially about innovation and organizing ideas.

I appreciate my friends and classmates: Liao Haixu, Liu Xuan, Naim, Naureen, Clay, Wang Yuxin and Zhang Anyi. We helped each other with joy, hard work, and perseverance in both our research and in our lives.

TABLE OF CONTENTS

LIST OF FIGURES

LIST OF TABLES

ACKNOWLEDGMENTS

I would like to thank my supervisor Dr. Shengnian Wang for his guidance and support throughout my Ph.D. study. He always gives me innovative ideas and helps me to overcome the technical challenges of executing experiments and finishing my dissertation. I would also like to thank my committee members, Dr. Lvov, Dr. Radadia, Dr. Arumugam, and Dr. Nan for their valuable advice and feedback on this dissertation.

I appreciate Dr. Yusuf Darrt for his hard work in the application of halloysite in lithium-sulfur batteries. We collaborated happily and shared a lot of experience in material treatment. My special thanks go to the members of Dr. Wang's research group who assisted in this work, Haixu Liao, Dr. Xuan Liu, Dr. Yuxin Wang, Dr. An-Yi Chang, Clay Guan, Liping Hua, Sean Nations, and Cody Baxter. We worked together and supported each other in the lab, in school, and in our daily lives.

I am grateful to Ms. Debbie Wood and Mr. Davis Bailey in IFM for their generous help and support. I am grateful to all professors who taught me classes at Louisiana Tech University. They generously shared their knowledge that inspired me to ask deeper questions and think critically.

Finally, I want to thank my parents, Pei Zhenan and Zhang Suying for their love and support in all aspects.

CHAPTER 1

INTRODUCTION

1.1 Research Hypothesis

1.1.1 Critical Problems

Lithium-ion batteries have been widely used in various portable electronic products and electric vehicles because of their high energy density and long cycle life. In lithium-ion batteries, lithium ions migrate from anode to cathode through the electrolyte, making lithium-rich states in the cathode during charging. When discharging, lithium ions move in the opposite direction.

The cathode material of lithium-ion batteries accounts for about 40% of the total cost and decides the maximum energy storage capacity. Current commercial cathode materials of lithium-ion batteries include lithium cobalt oxide, lithium manganate oxides, and lithium iron phosphate. However, a practical capacity of 150-175 mAh/g limits the viability of these cathode materials for applications that demand higher energy density such as electric vehicles and stationary power stations (Nelson *et al*., 2019; Ahmadi *et al*., 2014). Among some promising cathode candidates, a sulfur cathode has a theoretical specific capacity of 1,673 $mAhg^{-1}$, or around five times the amount of lithium-ion batteries' commercial cathodes. However, the current sulfur cathode, when paired with lithium metal anode to establish the Li-S battery system, still suffers great technical challenges, namely low conductivity, parasitic shuttle reactions induced by dissolution of

lithium polysulfides (Li_2S_x, $4 \leq x \leq 8$), large volumetric expansion (~80%) upon lithiation, and self-discharge issues. The presence of large grains of sulfur particles in most sulfur cathodes and their tendency to aggregate and grow in size during cycling restricts the diffusion of Li^+ ions and the transformation kinetics between sulfur and lithium sulfur (Li_2S) during charge/discharge processes.

As for the anode materials of lithium-ion batteries, various carbon materials are used to host lithium ions. The performance of these carbon electrodes heavily depends on their carbon structures, the raw synthesis materials, and the material treatment methods. Because the electrical potential of carbon is very close to that of metal lithium, when the battery is overcharged, metal lithium easily precipitates on the surface of carbon electrodes to allow the formation of dendrites, which causes a short circuit and runaway of the battery temperature. Therefore, it is of great importance to find new anode materials that can host lithium at a slightly positive potential; they must also be cheap, reliable, and have a high specific capacity.

Supercapacitor is another attractive chemical energy storage system which has the highest power density, which makes it especially suitable for the load balancing device of electric vehicles. It works either as an electric double layer capacitor or oxidation-reduction pseudo-capacitor. Compared with battery-based energy-storage systems, it has faster charge and discharge speed and longer cycling life. But its energy density is much smaller than that of a battery. Therefore, the main direction of basic research and industrial development of a supercapacitor is to further improve its energy capacity while maintaining its high-power characteristics.

1.1.2 Objectives

Objective 1: We choose the use of halloysite nanotubes (HNTs) to host sulfur and serve as the cathode of lithium sulfur batteries for two reasons: one, they have a lumen size of 15 to 20 nm, which can be used to hold and confine sulfur particles (their layered structure offers large surface area to hold insoluble sulfur species so that they remain in small size and good dispersion status during the charge/discharge processes), and two, the halloysite nanotubes are further assembled into clusters. The formed nanoscale voids help divide electrolyte and solid-electrolyte interphases into isolated domains that add an extra diffusion barrier to suppress the dissolution and migration of polysulfides.

Objective 2: We adopt silicon/carbon composite nanofibers as a natural solution of challenges that are associated with these two types of anode materials when used alone, while inheriting some merits from each of them (carbon for high electrical conductivity and silicon for high lithium capacity). High silicon content is essential for composite anodes for their potential large energy capacity, but the continuous addition of silicon nanoparticles in a polymer solution would lead to a dramatic increase of the fluid viscosity during the fiber production and technical difficulty for the processing. It may also result in collapsed composite nanofibers or nanofibers of ductility loss. This sets the maximum allowance of silicon content in a particular polymer solution. We made some efforts on mitigating this processing dilemma by carefully designing a new nanofiber-in-microfiber architecture and prepared it via a coaxial electrospinning process. We then tested this silicon-rich, composite electrode as anodes of lithium-ion batteries to pair with high-capacity cathodes to leverage the overall capacity.

Objective 3: For supercapacitors, studies have shown that an electrode material itself and its architecture features, such as large surface area, rich active sites, and good electrochemical conductivity, are critical to achieve superior electrochemical performance. One-dimensional (e.g., carbon fibers) or two-dimensional (e.g., graphene) carbon materials with a connected network generally have good electrical conductivity, but they also have relatively limited surface area, high cost, and low manufacturing capacity. Zero-dimensional carbon such as carbon nanoparticles can provide a flexible, specific surface area attributed to their tunable size, size distribution, and shape. However, their discrete nature requires assistance of conductive non-active additives or other carbon structures to make a working electrode. Coupling different carbon materials is a practical way to combine the advantages from each individual carbon format to achieve superior storage capacity, high conductivity, and excellent cycling stability.

1.2 Approaches

Based on these hypotheses, halloysite nanotubes were first treated with sulfuric acid to expand their lumen. Graphite-like carbon skin was then introduced on the nanotube surface through a hydrothermal treatment of glucose to increase the conductivity of halloysite nanotubes. Sulfur was dissolved in EDA or toluene and loaded into those treated halloysite nanotubes afterwards. This ensures good sulfur utilization and less capacity fading during charge/discharge cycles.

For silicon anodes, the nanofiber-in-microfiber composite mat was prepared using a coaxial electrospinning process followed by carbonization in a nitrogen atmosphere. The produced carbon/silicon composite electrode effectively balances the issues between electrode pulverization and high reversible capacity. Promising electrochemical

performance and capacity retention were achieved for silicon-rich anodes at an intermediate charge rate.

For the supercapacitors, plastic waste was transformed into stable carbon quantum dots and sheets with a large number of functional groups via hydrothermal reaction under the help of small molecules with hydroxyl groups. With enhanced conductivity and unique ball-sheet structure, they were used as supercapacitor electrodes to host ions and achieved relatively high capacity.

1.3 Structure

Chapter 1 outlines the central problems and objectives of this research project. It also briefly introduces our research approaches and the organization of this dissertation. Chapter 2 provides a literature review of relevant research fields. This review includes recent research work on the cathode and anode of rechargeable lithium batteries and carbon-based electrode materials for supercapacitors. Chapter 3 demonstrates our concept of confining sulfur particles in clay nanotubes with improved cathode performance of lithium-sulfur batteries. Chapter 4 demonstrates the production of nanofiber-in-microfiber structure in carbon/silicon composites and proves its advantages as anode with high silicon content. Chapter 5 demonstrates high performance supercapacitors of a novel ball-sheet carbon structure derived from waste plastics. Chapter 6 summarizes the results of the entire dissertation and recommends some relevant future research directions.

CHAPTER 2

LITERATURE REVIEW

2.1 Lithium Batteries

Efficient, effective, and economical energy storage systems remain one of the major challenges in the deployment of clean and abundant alternate energy technologies like wind, ocean, and solar power on a large scale (Tang *et al*., 2021). Their performances are often evaluated on two important parameters: energy density (i.e., specific energy) and power density (specific power). Energy density describes the amount of electricity an energy storage system can deliver, while power density measures the rate at which it may deliver the electric current. Among different systems, lithium-ion batteries may offer desired energy density, while supercapacitors show superior power density. Specifying individual battery or capacitor system, these two parameters are largely governed by the choice of electrode materials and/or their architectures (Raza *et al*., 2021).

In Li-ion batteries (LIBs), electrons are released on the anode by oxidation and travel through an external circuit to the cathode where the reduction reactions occur. Lithium ions migrate between the two electrodes in the electrolyte solution like ion shuttles to close the entire electric circuit. Commercial LIBs often consist of a graphite anode with a theoretical capacity of 372 mAh/g and a cathode made of lithium metal oxide or phosphate, such as $LiCoO_2$, $LiMn_2O_4$, or $LiFePO_4$, with a theoretical capacity of 300 mAh/g or less. They have been widely used in portable electronic devices such as

cellular phones, digital cameras, laptops, and tablets for high energy density (~double that of NiCd Batteries), less memory effect, and low self-discharge (Zhao *et al*., 2021). However, a practical capacity of 150-175 mAh/g limits their viability for even higher energy-density electricity storage systems such as electric vehicles and stationary power stations (Ryu *et al*., 2021).

Given the energy storage is largely governed by the choice of cathode, many other cathode materials have been investigated to increase the overall energy storage level. When sulfur is used (in most cases, paired with lithium ribbon anode, designated as Li-S batteries), it can offer a theoretical specific capacity as high as 1,673 mAh/g, or around five times that of existing LiB cathodes. The abundance and low-cost of sulfur (Chung *et al*., 2019) also makes Li-S batteries more attractive to transform the current battery-based market. However, a sulfur cathode suffers from low conductivity, parasitic shuttle reactions induced by dissolution of lithium polysulphides (Li_2S_x, $4 \leq x \leq 8$), large volumetric expansion (~80%) upon lithiation, and self-discharge (Helen *et al*., 2015). The potential for dendrite growth of lithium metal on the anode may also lead to short circuits and serious fire risk (Zhao *et al*., 2017). To suppress the growth of lithium dendrites and mitigate the consequent safety risk, pre-lithiated sulfur, or lithium sulfides (Li_2S), may be used as the cathode material to pair with commercial graphite anode of LiBs or many other promising anode candidate materials, such as silicon-based anode. However, other technical challenges such as “sulfur shutting” must also be tackled in Li-S batteries to move the commercialization forward.

Besides batteries, supercapacitors are another attractive energy storage system for their fast charge/discharge rates, high power density, and long cycle life (Manthiram *et*

al., 2013). Most supercapacitor electrodes are made of either porous carbon or metal oxides (Veerakumar *et al*., 2020). Studies have shown that the electrode material itself and its architectural features, such as large surface area, rich active sites, and good electrochemical conductivity, are critical to achieve superior electrochemical performance for supercapacitors. Various formats of carbon materials dominate the supercapacitor electrodes because of their excellent conductivity, rich active sites, and good chemical stability (Zhou *et al*., 2021).

2.2 Cathode Materials for Rechargeable Lithium Batteries

A typical Li-ion battery electrode has the electric collector (e.g., aluminum or copper foil) coated with a slurry mixture of powders of active materials, conductive additive, and a polymer binder. The cathode material is the most important part of a lithium-ion battery as it decides the total lithium storage and is the key performance indicator of the rechargeable battery such as cycle life and safety. Commercial LIBs use cathodes made of layered metal oxides and spinel metal oxides. Lithium iron phosphate ($LiFePO_4$), lithium manganate ($LiMn_2O_4$), and lithium cobalt oxide ($LiCoO_2$) have been commercially produced and used as the cathode of lithium-ion batteries. As a polyanion cathode material, $LiFePO_4$ has the advantages of high capacity, low price, rich sources of raw materials, environmental friendliness, excellent thermal stability, and cyclic charge and discharge performance. Because of this, they have become one of the preferred materials for high-capacity batteries. However, the low working voltage limits its energy storage density. $LiFePO_4$ material has an olivine structure, which determines that lithium ions can only diffuse along the direction of one-dimensional channels in its crystal, so the diffusion coefficient of lithium ions in $LiFePO_4$ material is very low. At the same time,

due to the lack of free gap atoms and holes in the crystal structure, the electronic conductivity of $LiFePO_4$ material is very low. Therefore, it is necessary to modify the characteristics of $LiFePO_4$ material to improve its diffusion ability of lithium ions and electronic conductivity (Zhang *et al.*, 2011). $LiMn_2O_4$ has a spinel structure. The transmission process of lithium ions in $LiMn_2O_4$ has a three-dimensional characteristic with high electronic conductivity and diffusion rate. $LiMn_2O_4$ also has good thermal stability, besides its rich sources of raw materials and low price. However, in the circulation process of $LiMn_2O_4$ will appear Jahn-Teller distortion. Mn^{3+} will undergo a disproportionation reaction to generate Mn^{2+} and dissolve in the electrolyte so that the spinel structure of $LiMn_2O_4$ is destroyed. This leads to rapid deterioration of the storage performance during high temperature circulation (Kim *et al.*, 2008). $LiCoO_2$ has good magnification performance and a layered structure of α-$NaFeO_2$, which gives high theoretical gram capacity and energy density. However, its thermal stability is poor, and the raw cobalt source is limited and expensive. With homogeneous doping technologies, other elements can be evenly distributed in cobalt lithium oxide to better support its layered structure. This helps improve the structural stability and cycle stability of cobalt lithium oxide (Moses *et al.*, 2007). Compared with the original metal oxide, ternary material has good thermal safety performance and cycle stability. $LiNi_x\ Co_yMn_{1-x-y}O_2$ has a layered structure similar to $LiCoO_2$. Because Ni, CO, and Mn jointly occupy the 3B position in the lattice, it forms a ternary material made of nickel, cobalt, and manganese. Such ternary materials have higher energy density, lower cost, and better safety performance than $LiCoO_2$. Increasing the content of Ni can improve the gram capacity of these ternary materials, while adding more Co can improve the conductivity of the hybrid

material. Lifting the content of Mn can improve the structural and thermal stability of the ternary material to boost the performance of cycling and reduce battery cost (Cheng *et al.*, 2017).

Unlike the lithium metal oxide cathode, elemental sulfur is used in the cathode of lithium-sulfur batteries, in which it reacts reversibly with Li^+ (**Figure 2-1**). Sulfur cathodes have many major problems. Elemental sulfur (S_8) and its complete discharge state (Li_2S) are an electrical and ionic insulator (for sulfur, its conductivity is $2.5*10^{-30}$ S/cm), which is difficult to activate. The poor wettability of S_8 in common organic electrolytes makes it unable to have good contact with the electrolyte to complete the electrochemical reaction, resulting in low utilization rate of sulfur. The intermediate products generated in the discharge process (i.e., polysulfides) easily dissolve in the organic electrolyte, which leads to a shuttle effect, the loss of sulfur on the cathode side, and slow corrosion of lithium negative electrodes. The discharge products (Li_2S_2 and Li_2S) will precipitate from the electrolyte, agglomerate on the surface of the electrodes, and block the contact between the active material and the electrolyte. The surface of metal lithium anode may generate lithium dendrites, leading to safety problems. Lastly, during charging and discharging, some lithium becomes inactivated and irreversible "dead" lithium.

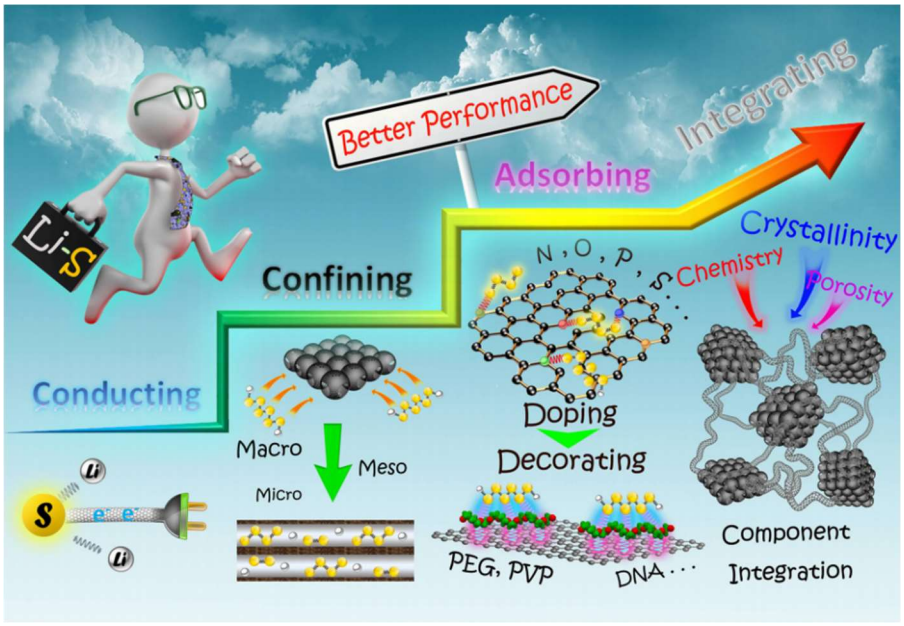

Figure 2-1: Roadmap towards better performance of carbon materials for Li-S batteries. (Liang *et al.*, 2015)

2.2.1 Modification of Carbon/Sulfur Cathode Materials

To sequester the intermediate polysulfide, porous carbon was applied to help trap polysulphides and provide conductive paths for electrons (Chung *et al.*, 2015; Ma *et al.*, 2015). Various porous carbon materials were explored not only because of their good conductivity, but also the high specific surface area and strong physical adsorption of sulfur on the surface as a sulfur carrier. Because of its low melting point and sublimation nature (the melting point of sulfur is 155 ℃), sulfur molecules can easily diffuse in pores or network voids of porous carbon materials by a simple heating method. The carbon materials used to host sulfur include mesoporous carbon, mesoporous carbon spheres, hollow carbon spheres, carbon nanotubes, carbon fibers, and graphene. In terms of morphology, they can be divided into mesoporous, hollow, layered, nanotubes, and other carbon materials. Wang *et al.* prepared one macroporous activated carbon sulfur composite as early as 2002 (Wang *et al*, 2002). The first discharge specific capacity of

sulfur in their system is 800mAh/g, but it decays to 440 mAh/g in the second cycle, and decays significantly afterwards.

Mesoporous carbon materials may provide larger specific surface area and pore volume besides their stable structure and good electrical conductivity, which makes them more suitable as sulfur carriers in Li-S batteries. In 2009, the Canadian Nazar team successfully used ordered mesoporous carbon CMK-3 as the sulfur-carrying matrix. CMK-3 carbon has a regular connected carbon rod structure with a gap width between those carbon rods about 3nm, as shown in **Figure 2-2** (Kim *et al*, 2014). Sulfur can easily penetrate the regular pore structure of CMK-3 when heated so that the sulfur loading dosage of the prepared sulfur carbon composites can reach as high as 70% (mass ratio). The size of sulfur particles in this composite is limited to 1 um. To further improve the electrochemical performance of the composites, a layer of polyethylene glycol (PEG) was coated on the surface of the S/CMK-3 composite (**Figure 2-2**). The PEG coating inhibits the volume change during charge and discharge, improves the conductivity of the composites, and reduces the dissolution of polysulfides in the electrolyte solution. The first discharge specific capacity of this composite cathode reached 1320mAh/g, which decayed slightly to 1100 mAh/g after 20 cycles. Jayaprakash *et al.* synthesized mesoporous carbon microspheres/sulfur composites with 69.75% sulfur by a template method. With a charge and discharge between 3.1~1.7V, the specific discharge capacity at 5C was 1071 mAh/g and 974 mAh/g of the first and 100th cycles, respectively, giving a retention rate of 91%. The coulomb efficiency of the 100th cycle was 94%, indicating that polysulfides were not dissolved in organic electrolyte.

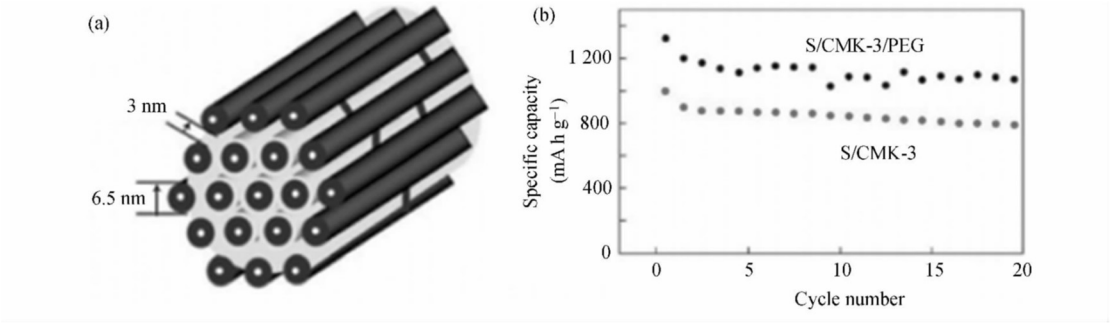

Figure 2-2: MK-3 structure diagram [a] and battery cycle performance curve [b] (Kim *et al*, 2014)

The strong adsorption of microporous carbon may also mitigate the dissolution of polysulfides to achieve good cycling stability. The surface area of microporous carbon can be extremely large with their small pore size so that sulfur can be highly dispersed in it. Zhang *et al.* made carbon microsphere/sulfur composite materials with a sulfur loading of 42%, and the utilization rate of sulfur reached up to 80%. The composite was cycled 500 times between 3.0 and 1.0V with a current rate of 0.4A/g, and the specific capacity was kept at 650 mAh/g. Its excellent cycling performance can meet the requirement for commercial battery systems.

Multi-walled carbon nanotubes (MWCNTs) and graphene also have a high specific surface area and good adsorption capacity. Their use in sulfur cathodes can significantly improve overall conductivity and cycling performance. Yin *et al.* had MWCNTs uniformly dispersed in PAN matrix to form chemical bonds during in-situ polymerization to receive pyrolysis pPAN-S/ MWCNT composites. The composite was tested at 0.1C with a specific capacity of the first discharge 697 mAh/g, and the capacity retention rate was 85% after 50 cycles. J.Z.Wang *et al*. directly compounded graphene and sulfur through a thermal treatment. However, because it is difficult to disperse sulfur uniformly in graphene, the cycling performance of their material was very poor. H.Wang

et al. synthesized S/graphene composites with multiple steps: sulfur particles were first coated with PEG, and a layer of graphene modified by carbon black after a low degree oxidation was then coated outside. This composite was tested at 0.2C, and its discharge specific capacity of the first and 100th cycles were 750 mAh/g and 600 mAh/g, respectively.

2.2.2 Sulfur/Conductive Polymer Composite

Conductive polymer materials can also be used as electrode materials for secondary batteries because of their good conductivity and electrochemical reversibility (Shacklette *et al*, 1987). In Li-S batteries, conductive polymer framework can not only improve the conductivity of elemental sulfur and inhibit the migration and diffusion of polysulfide ions, but also increase the stability of electrode materials. Conductive polymers including polypyrrole (PPY), polyaniline (PANi), PAN, and polythiophene (Pth) were used to prepare sulfur/conducting polymer composites by two methods: one is to synthesize conductive polymers with special nanostructures, such as tubular, reticular, dendritic and mesoporous spheres, before dispersing sulfur in their pores or network voids, while the other is to wrap sulfur nanoparticles with conductive polymers directly. This method must make sulfur reach a small enough size to achieve the coating effect. Sulfur nanoparticles are generally synthesized by chemical deposition processes. F. Wu *et al.* studied the effect of PTH content on coated sulfur particles for the electrochemical performance of the composite cathodes. When the sulfur content is 71.9% and the PTH content is 18.1%, the electrochemical performance reached its best. At a charge/discharge window of 3.0~1.0V and current of 100 mA/g, the discharge specific capacity was 1119.3 mAh/ g and 830.2 mAh/ g in the first and 80th cycles, respectively. Wang *et al.*

took acetylene black as the core, which was grafted PANi conductive network on the surface. Sulfur was then loaded through a simple chemical deposition method to form a multi-core-shell S/PANi structure. The biggest advantage of this composite material is that it has a large sulfur load (87%, mass fraction, and the sulfur load on the cathode can be as high as 6 mg/cm^2). The capacity of this cathode material was maintained at 835 mAh/g after 100 cycles.

2.2.3 Sulfur/TiO_2 Core-shell Composite Cathode Material

Cui Yi's group of Stanford University designed a new type of lithium sulfur battery using sulfur titanium dioxide (S-TiO_2) cathode material with an egg yolk-shell structure (**Figure 2-3**) (Liu *et al.*, 2012). When discharging at 0.5C, the initial specific capacity is 1030 mAh/g. After more than 1000 cycles, the coulomb efficiency is 98.4%. The capacity attenuation of this cathode per cycle is only 0.033%. The advantage of this egg yolk-shell structure is that its internal void part can withstand the excessive expansion of sulfur during the lithium process, so as to protect the structural integrity of the shell, minimize the dissolution of polysulfides, and enable the battery to have a high capacity retention rate.

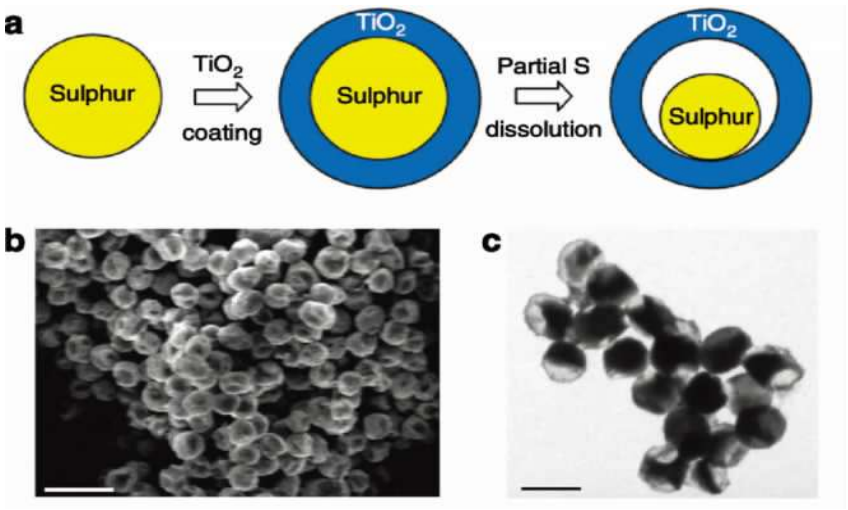

Figure 2-3: Synthesis and characterization of S/TiO_2 egg yolk shell nanostructures. (Liu *et al.*, 2012)

2.3 Anode Materials of Rechargeable Lithium Batteries

Lithium metal (a theoretical capacity of ~3,860 mAh/g) is the pair anode material in Li-S batteries. However, it poses many performance and safety issues, such as continuous breakdown and instability of the solid electrolyte interphase (SEI) layer from shape and volume changes of the lithium electrode and the non-uniform lithium deposition and dissolution during cycling. As a consequence, gradual growth of lithium dendrites and decaying of cycling efficiency occur. The deposition of polysulfides that migrate from the cathode makes the situation worse by continuously increasing the anode impedance. Despite some progress in lithium protection, unstable SEI and growing dendrites remain severe issues with lithium metal anodes during cycling (Li *et al.*, 2018).

The search for alternate anode materials focuses mainly on carbon and silicon, two common candidates that are also used in lithium-ion batteries. Traditional graphite anodes are not suitable in Li-S batteries due to incompatibility with the electrolyte system of Li-S batteries (Gupta *et al.*, 2020). Exceptions were found on non-graphitized hard

carbon in ether-based electrolytes. However, such studies mainly focus on silicon material. Si has high theoretical capacity (~3,579 mAh/g based on $Li_{15}Si_4$) (Beattie *et al.*, 2007). Together, with its rich reserve on Earth and suitable voltage platform, these merits make Silicon an attractive anode candidate to replace graphite anode in the next generation of rechargeable lithium batteries.

However, silicon-based materials also have some problems. The alloying reactions that bring ultra-high specific capacity also cause drastic volume change to silicon. For example, the theoretical volume expansion of the $Li_{15}Si_4$ alloy phase is about 300%. For a single silicon particle, the volume of amorphous Li_xSi formed in the outer layer will expand during lithium intercalation, but the inner layer will not. This will cause huge stress in individual silicon particles, resulting in cracking, continuous generation of fresh silicon surface, and growth of the solid electrolyte layer (SEI) after its exposure to electrolytes (**Figure 2-4a**). As a consequence, extra lithium ions are consumed, and the transport of lithium ions slows down. As for the whole electrode, the expansion and contraction of Si particles during charge/discharge processes will squeeze or pull multiple surrounding particles in the electrode, causing them to lose contact with the electrical current collector to become “dead” silicon (**Figure 2-4b**) and quickly reduce the overall capacity during cycling (Jiao *et al.*, 2020). These issues make it difficult for silicon to be commercialized as an anode material in rechargeable lithium batteries.

Such issues could be mitigated with nanostructured Si paradigms in the format of nanoparticles or nanowires. However, the synthesis of nanosilicon relies on PECVD and other expensive equipment, which makes the production very costly because of the harsh processing conditions and limited scalability of desired material configuration for mass

production. In addition, nanosilicon materials also suffer intrinsic low conductivity (Zhang *et al.*, 2016). These shortcomings limit the use of nanosilicon to a certain extent. Therefore, low-cost and high-yield synthesis technology for nanosilicon is needed.

Considering their working principles, it is necessary to improve both the electron and ion mobility of an active material in an electrode. A certain amount of nitrogen and fluorine doping can improve the carrier mobility and lithium storage capacity of the electrode material in Li-ion batteries. A porous structure also increases the number of accessible sites on the electrode material to shorten the transport time of lithium ions. So, it is ideal to design a composite electrode material with a microstructure that combines silicon with another material of good conductivity and high porosity to carry the merits from both materials. Reasonable structural design of nanosilicon/carbon materials, such as a hollow core-shell or 3D porous structure, may significantly reduce the volume expansion and contraction caused by lithium ion intercalation as well as other challenges in silicon-based anodes to achieve better electrochemical performance. Various silicon/carbon composites were investigated with different fabrication methods to race for these desired architectures.

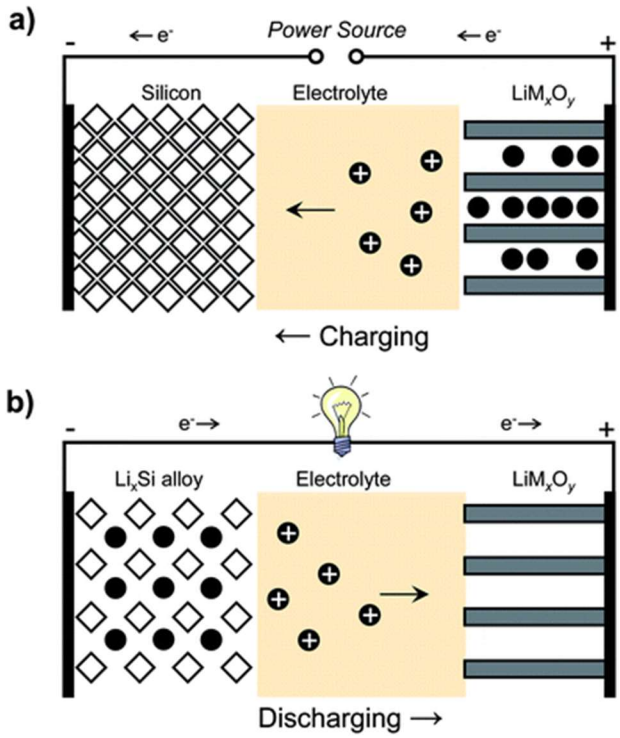

Figure 2-4: Schematic of a lithium battery containing a silicon anode and lithium metal oxide cathode during a) charging and b) discharging. (Szczech. *et al*, 2010)

2.3.1 Chemical Vapor Deposition

Chemical vapor deposition (CVD) is often used to prepare coatings of nanomaterials on silicon to inhibit the volume change issues to a certain extent and achieve good cycling performance. The advantage of this method is that the coating thickness outside each particle is very uniform and there is almost no exception of unencapsulated silicon. Common organic raw coating materials such as ethanol, methane, and benzene can be flexibly selected. The disadvantage of CVD coating is that the production capacity is small, and the outcome of the volume accommodation is quite limited. Yoshio *et al.* 2020 used CVD to decompose benzene vapor at 1000℃ to repeatedly deposit carbon shells on the surface of Si particles and obtained Si/C composites with an average particle size of 18 μm, a carbon content of 20%, and a

specific capacity of 800 mAh/g. Since Si particles were embedded in the mesh nanopore of C, more Li_xSi alloy participated in the discharge reaction to remove more lithium ions and the composite material showed a higher initial coulombic efficiency.

2.3.2 Hydrothermal Method

A hydrothermal method refers to the addition of water and powder materials in a closed container before the aqueous solution is heated and pressurized by the self-generated vapor so that insoluble materials at normal conditions can be dissolved and recrystallized in high-temperature and high-pressure conditions. Hydrothermal methods can transform amorphous carbon material into a crystalline state with uniform size and without calcination and grinding steps, which may prevent the formation of structural defects and the introduction of impurities. Demir *et al.* used glucose as a carbon source and created a carbon coating on prefabricated silicon nanoparticles with a particle size of 20~50 nm by a one-step hydrothermal method. In order to improve the stability and conductivity, the nanocomposite was further carbonized under nitrogen protection for 2 hours to achieve complete carbonization. Hari *et al.* 2019 synthesized Si/C-TiO_2 composite by a hydrothermal method with carbon-coated silicon and TiO_2 powders separately; Si-TiO_2 composite anode materials were then prepared by the same method. It was found that TiO_2 particles uniformly covered the surface of Si and Si/C, acting as a buffer layer to accommodate the generated stress when the volume of Si changes during lithiation. Zhou *et al.* 2020 first synthesized Si and monoclinic TiO_2 (TiO_2-B) by a hydrothermal method that formed a Si@TiO-B "core-shell" composite material, which was then mixed with CNTs and calcined to prepare interconnected Si@TiO_2-B/CNTs composite anodes. In the prepared anodes, CNTs were uniformly dispersed and attached

to Si@TiO_2-B nanoparticles. Such an ideal uniform nanostructure effectively avoids component separation and allows its internal components to play their roles so that the cycle stability of the assembled electrode is improved.

2.3.3 The Ball Milling Method

The ball milling method is easy to use, but the specific capacity, capacity retention rate, and cycling stability of electrodes made by ball-milled materials are low. When combined with other methods, the electrode performance can be effectively improved. Cabello *et al.* Prepared silicon@graphite composite materials by wet ball milling for negative electrodes. The addition of grinding aids made particles evenly distributed without agglomeration. Yoshio *et al.* 2020 milled micron-sized silicon particles together with graphite and silver particles for 5 hours to prepare silicon/carbon nanocomposites that contain 10% (mass fraction) silver. Its reversible specific capacity reached 600mAh/g at maximum, which gradually decreased during cycling. Adding graphite (**Figure 2-5**) and reducing the size of silicon particles further improved the cycling performance. Liu *et al.* used rice husk as the raw material to synthesize SiO_2 by acid hydrolysis and high-temperature reaction in an Ar/H_2 (4%, volume percentage) atmosphere at 970℃. The interconnected silicon nanoparticles were successfully embedded in the SiO_2 matrix and the formed Si/SiO_2 powders were then etched by hydrofluoric acid to form mesoporous silicon, which was milled with carbon nanotubes to obtain CNT/Si composites. Zhang *et al*. 2009 also synthesized porous Si/C composites by wet ball milling of Si powder and sucrose. The anodes made of these composite materials achieved a capacity of 2028 mAh/g and a 91.7% capacity retention after 100 cycles.

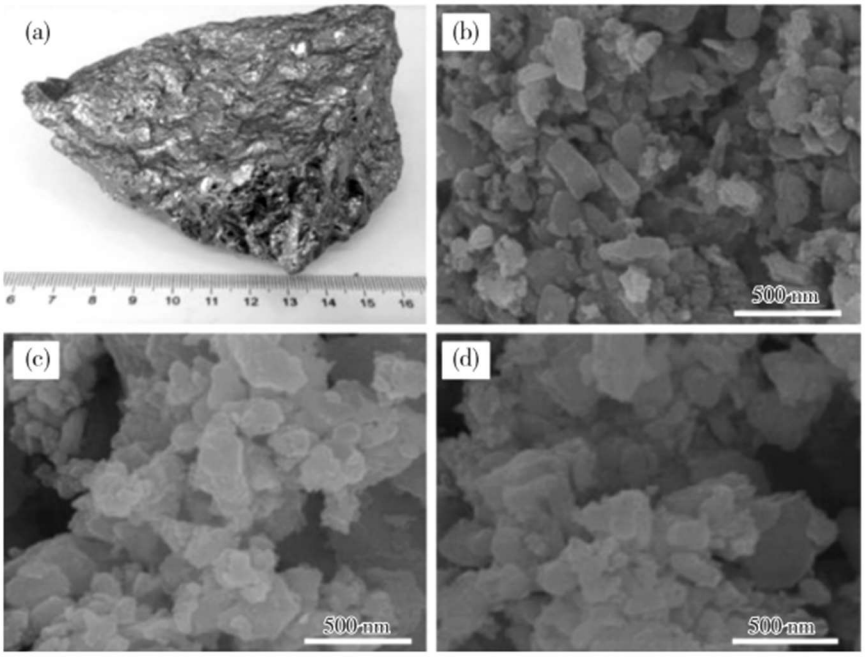

Figure 2-5: (a)The photograph of bulk metallic silicon (MS); SEM microscopy image of (b) the milled MS, (c) the milled MS-G, (d)MS-G@C. (Sun & Wang *et al.*, 2016)

2.4 Electrode Materials for Supercapacitors

Compared with traditional capacitors, the energy density of supercapacitors is 10 ~ 100 times higher and can release a large current in a short time (that is, high specific power). (**Figure 2-6**) Besides its high specific capacitance and specific power, the wider operating temperature range and longer cycle life also make it another good candidate for an energy storage system. Compared with lithium-ion batteries, it has the advantages of faster charging speed, higher charging efficiency, longer cycle life, and less environmental pollution. The electrochemical performance of supercapacitors is largely decided by the electrode material and paired electrolytes. Carbon, transition metal oxides, and conductive polymers dominate the electrode materials of supercapacitors. Among them, carbon materials have high cycle stability, transition metal oxides have large specific capacitance, high energy, and power density, and conductive polymers have high

conductivity. By organically combining the advantages of carbon materials, transition metal oxides, and conductive polymers, multi-component composite electrode materials were prepared, and the assembled supercapacitors can meet the actual requirements on the energy and power density for specific applications after the preparation process is optimized.

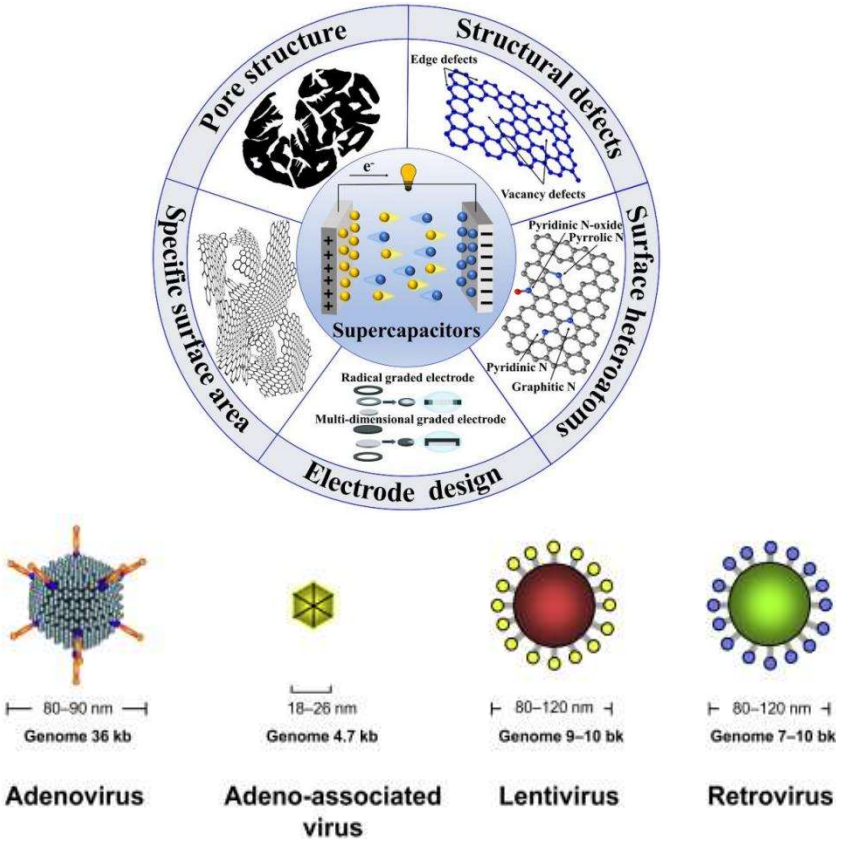

Figure 2-6: Influencing factors on the electrochemical performances of porous carbon-based supercapacitors. (Luo *et al.,* 2021)

2.4.1 Activated Carbon

Activated carbon has the advantages of high conductivity, large specific surface area, and good chemical stability. Its preparation process is simple and mature, and can be made by very diversified raw materials. Various hydrocarbon resources, such as

coconut shell, rice hull, cola and other carbon-rich materials, can be made into activated carbon and demonstrate good electrochemical properties when used as supercapacitor electrodes. However, the nonuniform pore size distribution and low utilization of specific surface area often led to large variance on the supercapacitor performance. Jurewicz *et al.* 2004 mentioned that the electrochemical performance of capacitors is mainly determined by the total surface area contributed by pores of various sizes in the activated carbon; micropores provide a high specific surface area for adsorbed ions, while mesopores provide large pathways for fast ion migration. Therefore, carbon materials with good electrochemical properties require reasonable pore size distribution. Activated carbon with a controllable pore structure was prepared from sucrose using a MCM-48 template, which gives a specific surface area of 2000m^2/g. Its specific electric capacity in 1M H_2SO_4 reached 206 F/g. Yin *et al.* 2016 obtained three-dimensional porous carbon by activating coconut fiber with KOH, whose specific surface area reached 2898 m^2/g after being activated with 4:1 mass ratio of KOH to carbon. At a current density of 0.1 A/g, its specific capacitance reaches 206 F/g. Even when the current density increases to 10 A/g, the specific capacitance still has 76% of the initial specific capacitance. It has an outstanding specific energy of 53 Wh/kg and a high specific power of 8224 W/kg. Zhang *et al.* 2016 synthesized activated carbon with a specific surface area of 2326.4m^2/g and a micro-mesoporous structure by activating petroleum coke with KOH. When the current density increases from 1 A/g to 50 A/g, its specific capacitance decreases by 48%. In order to improve the specific capacitance, a hydroquinone/activated carbon composite electrode was prepared by physical adsorption of hydroquinone. With a current density of

50 A/g, the specific capacitance was 300.2 F/g and the specific energy reached 19.5 Wh/kg in a H_2SO_4 solution.

2.4.2 Activated Carbon Fibers

Activated carbon fibers (CNFs) that are made from wood, polymer resin, and asphalt are also used as supercapacitor electrodes after being stabilized at a low temperature and then carbonized. It has better conductivity and lower density than activated carbon (about 0.1 g/cm^3 when compared to that of activated carbon, which falls around 0.5 g/cm^3). CNFs have good chemical stability, a porous fiber network, and low expansibility so that adhesives may not be required when used as the electrode. Kim *et al.* 2004 used an electrospinning technology to prepare nanofiber films. After stable carbonization, carbon nanofibers showed a specific surface area of 500-1220 m^2/g and its specific capacitance reached 35-202 F/g. Liu *et al.* 2016 used a natural biomass ecological cotton fiber as the raw material and made use of the expansion behavior of biomass to synthesize conducive carbon fibers, with layered porous structures that have a pore diameter close to 2.63 nm and a specific surface area of 584.49m^2/g. The specific capacitance of electrodes made of their material was 221.72 F/g when measured at a current density of 0.3 A/g. After 6000 cycles the specific capacitance decreased by only 4.6% at a current density of 2 A/g. Huang *et al.* 2016 prepared highly porous activated carbon fibers by cedar sawdust with high specific surface area (2395 m^2/g). After being activated by KOH steam and made into electrodes, the supercapacitors showed a specific capacitance of 242 F/g at a low current density of 0.5 A/g. At the specific power of 250 W/kg, the specific energy of this mesoporous activated carbon fiber electrode reached 8.4 Wh/kg. Even when the specific power was reduced to 2.5 W/kg, the specific energy still

had an 80% retention rate. In addition, such activated carbon fiber electrodes showed good cycle stability. Its specific capacitance decreased by only 8.2% after being cycled 10000 times at a current density of 3 A/g.

2.4.3 Graphene

Graphene has many unique properties, such as large specific surface area, high conductivity, and good chemical and thermal stability, which have attracted extensive attention as electrode materials for supercapacitors. In the practical graphene electrodes, due to the strong van der Waals force between graphene sheets, agglomeration often occurs and the specific surface area is therefore reduced. This makes it difficult to be soaked by electrolyte. To mitigate these shortcomings, graphene is usually mixed with metal oxide particles, doped with conductive polymers, or introduced with relevant functional groups. In the preparation of graphene-based electrodes, it is necessary to reduce the disordered stacking of graphene sheets to increase the effective area of the electric double layers in supercapacitor applications. For example, Kady *et al.* 2012 put two carefully made graphite oxide films into the ordinary DVD drive respectively (**Figure 2-7(a,b,c)**). After laser irradiation, the graphite oxide film on the drive was reduced to graphene, which showed a conductivity of 1738s/m, a specific surface area of 1520 m^2/g, high strength, and good flexibility. After placing the two graphene films in the electrolyte to form a supercapacitor (**Figure 2-7(d)**), the resulting capacitor had a large storage capacity and only a 3% capacitance decay after 10,000 charging and discharging cycles. Sliwak *et al.* 2016 doped nitrogen into reduced graphene oxide via a hydrothermal method, with a nitrogen content of 10.9% ~ 13.4% (atomic fraction). The specific capacitance of this nitrogen doping composite (13.4% atomic fraction) showed a

244 F/g capacitance at a scanning rate of 100 mV/s after being made as a supercapacitor electrode. In comparison, the specific capacitance of the reduced graphene oxide without nitrogen doping was only 70% of the former. After 5000 cycles of charge and discharge, the specific capacitance of the former was 92% of the initial capacitance.

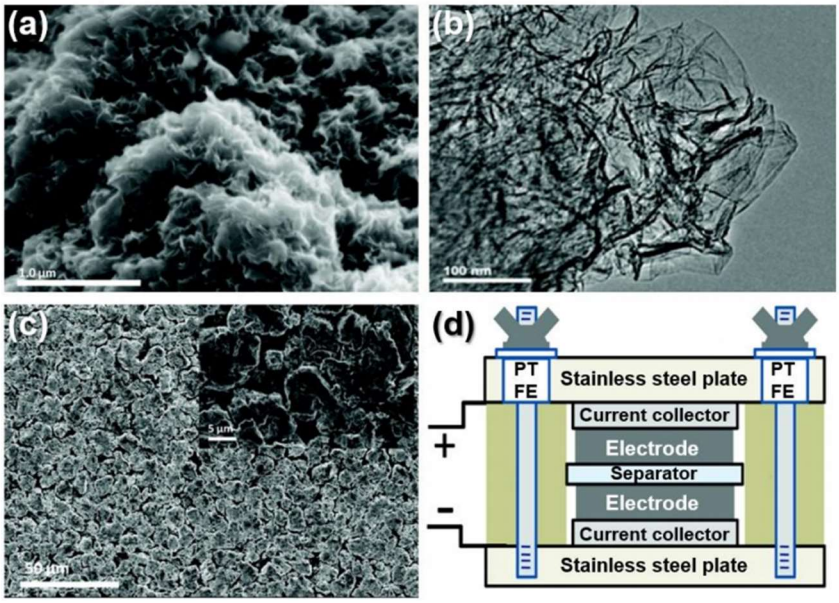

Figure 2-7: SEM (a) and TEM (b) images of individual graphene particles, respectively, (c) SEM image of graphene electrode, and (d) scheme of graphene-based supercapacitor. (Stoller *et al.*, 2008)

2.4.4 Carbon Aerogel

Carbon aerogel is a new type of amorphous porous carbon material, which has a large specific surface area, good conductivity, uniform pore distribution, and good chemical stability. Carbon aerogel is usually amorphous with a rich pore structure and is considered an ideal electrode material for double-layer supercapacitors. However, its complex synthesis process, high cost, and difficulty in large-scale production have restricted its commercialization. Pekala first synthesized carbon aerogel in 1987. Saliger *et al.* 1998 obtained carbon aerogels by thermal decomposition of phenolic resin under

supercritical conditions. The specific capacitance of their carbon aerogels in sulfuric acid solution reached 160 F/g. Ma *et al.,* 2016 prepared interconnected, layered porous carbon aerogels, in which a large number of three-dimensional carbon nanospheres formed in the layered porous structure. Low resistance and short diffusion distance were found to benefit its conductivity and ion transport. In a 6M KOH electrolyte, at a current density of 0.05 A/g, the measured specific capacitance was 368 F/g. When the current density rose to 100 A/g, the specific capacitance was still 228 F/g. After 10000 cycles, the specific capacitance was still 98.4%, which fully demonstrates its good cycle stability.

2.4.5 Transition Metal Oxides Supercapacitors

The energy storage mechanism of transition metal oxides materials in supercapacitors is mainly based on the reversible Faraday reactions, including electron transfer between electrode materials and electrolyte, which makes the energy storage similar to a high quasi-capacitance supercapacitor. In recent years, for environmental protection and economic considerations, scientists began to look for low-cost, pollution-free transition metal oxides as alternative electrode materials of supercapacitors. At present, MnO_2, NiO, CoO, Co_3O_4, etc. are extensively studied. Some composites of cobalt and nickel oxides, such as spinel nickel cobaltate ($NiCo_2O_4$), have rich active sites, high conductivity, low price, and environmental friendliness. However, most transition metal oxides usually have defects. For one, the electronic structure defects make the conductivity of the electrode material very low. High resistivity increases the thin-layer resistance and charge transfer resistance, especially under high current density. This causes significant voltage drop, which is undesired in practice. Second, it is difficult to accurately control the specific surface area, pore distribution, and porosity of transition

metal oxides. Finally, pseudo capacitance is generated on both the surface and inside of the whole electrode, thus its capacitance and energy density are higher than the electrodes with the electric double layers. For example, with the same working area and size of electrodes, the capacitance of a pseudo capacitor can be 10 ~ 100 times higher that of a double-layer capacitor. In order to solve these problems, researchers usually combine transition metal oxides with highly conductive carbon materials to improve the overall conductivity, specific capacitance, and power and energy density of electrode materials. Liu *et al.* used GO and $MnSO_4$ as raw materials to prepare flower-shaped MnO_2/graphene composites by electrochemical deposition. In a three-electrode system, the specific capacitance of the composites reached 595.7 F/g at a current density of 1 A/g (Liu *et al*., 2014). A flexible supercapacitor with MnO_2 nanosheets directly grew on the conductive CNFs, which showed great potential in the fields of portable and wearable devices. A specific capacitance of 634.5 F/g was achieved at a current rate of 2.5 A/g. After 3000 cycles of operation, its capacitance retention reached 95. 2% (Yu *et al*., 2016). In another case, a thin layer of CNTs was grown on Ni nanowires by electron beam deposition (CVD). MnO_2 nanosheets were then deposited on the surface of CNTs by a simple solution reduction method. The introduction of CNTs greatly improved the conductivity of this material. Under an appropriate load, the specific capacitance of MnO2@CNTs/Ni reached an amazing 1072 F/g at a current of 1 A/g (Sun *et al*., 2017).

CHAPTER 3

CONFINING SULFUR PARTICLES IN CLAY NANOTUBES WITH IMPROVED CATHODE PERFORMANCE OF LITHIUM-SULFUR BATTERIES

3.1 Introduction

Efficient and cost-effective battery systems are crucial to store and utilize clean, abundant, and long-term alternate energy from the wind, ocean, and sun (Armand *et al.*, 2008; Dunn *et al*., 2011; Thackeray *et al*., 2012; Choi *et al*., 2012). Among different types of batteries, rechargeable lithium-sulfur batteries (Li-S) show promising potential as a mobile energy supply because of their high energy storage capacity (a theoretical specific capacity of 1,673 $mAhg^{-1}$, or around five times that of existing lithium-ion batteries, LIBs) (Manthiram *et al.*, 2014). However, current Li-S batteries still suffer great technical challenges on their sulfur cathode, namely low conductivity, parasitic shuttle reactions induced by dissolution of lithium polysulfides (Li_2S_x, $4 \leq x \leq 8$), large volumetric expansion (~80%) upon lithiation, and self-discharge issues (Mikhaylik *et al.*, 2004; Yamin *et al*., 1988; Aurbach *et al*., 2009; Gao *et al*., 2011; Barchasz *et al.*, 2012). Tremendous efforts have been made in the past decade to tackle these problems, including the adoption of sulfur/carbon composites to promote sulfur cathode conductivity (Evers *et al.*, 2012; Yang *et al.*, 2017; Liang *et al*., 2099; Jayaprakash *et al*., 2011; Wang *et al*., 2013; Lee *et al.*, 2013; Huang *et al*., 2015; Wang *et al*., 2002) and the introduction of additional layers (Su Y. *et al.*, 2012; Su *et al*., 2012; Song *et al*., 2015;

Wang *et al*., 2014; Guo *et al.*, 2013) or sophisticated porous structures (Wang *et al.*, 2011; Ji *et al.*, 2009; Dorfler *et al*., 2010; Zheng *et al*., 2011; Song *et al*., 2016; WeiSeh *et al.*, 2013; Tan *et al*., 2017; Li *et al*., 2018) to slow down or lock intermediate polysulfides to reduce their shuttle effect. However, the presence of large grain sulfur particles in common cathode materials and their tendency to aggregate and grow in size restricts the diffusion of Li^+ ions and transformation kinetics between sulfur and lithium sulfur (Li_2S). To overcome such sulfur utilization issues, some pioneer scientists found that ultra-small sulfur nanoparticles anchored on a conductive carbon host in monodispersed status are effective to achieve almost theoretical discharge performance (Xin *et al.*, 2012; Chen *et al*., 2015; Zhang *et al*., 2014). Their results also reveal that a slight increase of the size of sulfur nanoparticles could quickly forfeit such advantages: a nearly 25% loss of the initial capacity when sulfur nanoparticles of 5 nm are replaced by 40 nm ones (Chen *et al.*, 2015). Given the unavoidable dimension evolution of sulfur species and their gradual erosion from host carriers during long-term cycling, continuous capacity fading still exists. The unsolved polysulfide shuttle effect and deposition of Li_2S when alternating between charge and discharge cycles further worsen the electrical contact issue within sulfur cathodes, particularly at high current rates. How to maintain the dimensions of sulfur nanoparticles with satisfactory sulfur utilization and capacity retention remains unsolved for Li-S batteries.

Here we introduce a new type of nanostructure to help lock sulfur size and suppress the migration of polysulfides in Li-S batteries. A natural tubular nanoclay material, halloysite (or HNTs), is used to offer desired nanoscale space to host sulfur particles. Halloysites are primarily found in volcanic-derived soils and/or carbonate rocks

in tropical regions for their favorable environment (i.e., high temperature, high water vapor pressure, and high CO_2 concentration) towards hydrothermal alteration of aluminosilicate minerals into a roll-up tubular nanostructure (Kerr *et al.*, 1952). With a unit configuration of $Al_2Si_2O_5(OH)_4$, these natural nanotubes have the outer surface of each roll composed of SiO_2 and the inner surface of Al_2O_3, which, when hydrated, carries negative and positive charges, respectively (Lazzara *et al.*, 2018). As shown in **Figure 3-1a**, halloysite nanotubes have a gap between neighboring roll layers of 7-10 Å, an average diameter 15-20 nm for the central lumen, and an average length of 0.5-2 μm, which vary with their original sources and processing methods. Such a unique one-dimensional, hollow nanostructure and oppositely charged internal and external surfaces allow flexible loading of many different functional materials for applications in composites, electronic materials, drug delivery, and personal care products (Lvov *et al.*, 2016; Lin *et al.*, 2017; Lun *et al*., 2018; Liu *et al*., 2016). For sodium ion battery application, their conductive halloysite nanotubes, cathode materials were synthesized by wrapping a layer of polypyrrole (PPy) via in situ polymerization, and they could maintain a capacity of 126 mAh g−1 after 280 cycles at current density of 200 mA g^{-1} (Cao *et al.*, 2021). As for Li-S batteries, due to the permission of fast migration of Li^+ ions in their charged nanotube geometry, polyethylene oxide based solid electrolyte composites with 5-10 wt.% of halloysites show increased ionic conductivity at room temperature (~$1.5*10^{-4}$S/cm), inaddition to their enhanced tensile strength (50-60 MPa) (Lin *et al.*, 2017; Lun *et al*., 2018). Besides their unique ion transport pathways, we hypothesize that the appropriate lumen size of halloysites could provide desired space to confine sulfur nanoparticles when used in the cathodes of Li-S batteries

(**Figure 3-1b**). Their layered structure offers a large surface area for insoluble sulfur species to retain their small size and good dispersion status during their transformation cycles. These halloysite nanotubes further assemble into clusters, creating many nanoscale voids, which help divide electrolyte and solid-electrolyte interphases into isolated domains and add an extra diffusion barrier for polysulfides to suppress their dissolution and migration (**Figure 3-1c**). To increase sulfur loading dosage and cut Li^+ ion diffusion distance, halloysites are first etched by sulfuric acid to expand the hollow chamber space of nanotubes and shorten their length. Prior to serving as the host of sulfur particles, a thin conductive carbon layer is coated on the surface of halloysite nanotubes through a hydrothermal method using glucose as the precursor (Owoseni *et al.*, 2015; Du *et al*., 2019). This carbon skin on individual nanotubes provides the needed electrically conductive network inside the assembled halloysite clusters during charge and discharge processes. Sulfur is introduced by wet impregnation with sulfur nanoparticles initially dissolved in either toluene or ethylenediamine (EDA). The obtained composite materials are finally mixed with other cathode additives and assembled into coin batteries for electrochemical performance tests.

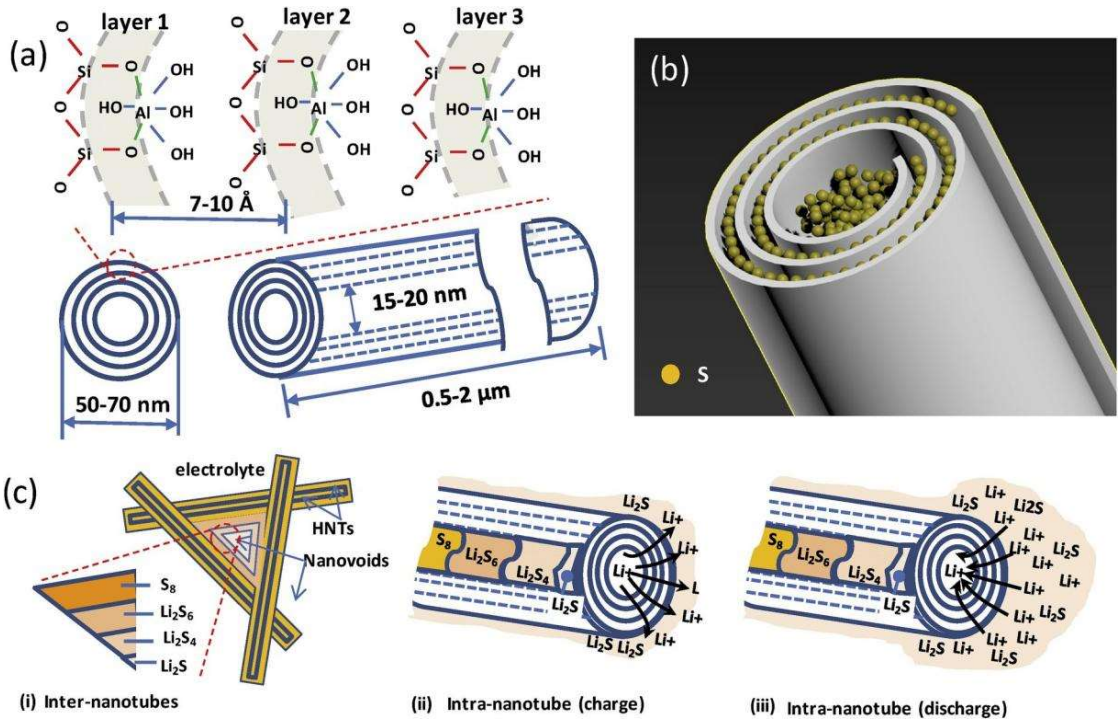

Figure 3-1: Schematic of dimensions and structure of halloysite nanotubes (a), sulfur loading and confinement inside halloysites (b), and charge and discharge situations in halloysite/sulfur composites cathode (c). Subpanel c(i) illustrates polysulfides profile in an isolated inter-nanotube domain created by assembled halloysite clusters; subpanels c(ii) and c(iii) illustrate polysulfides profile inside and near the entrance of an individual halloysite nanotube during charge and discharge process, respectively. Electrolyte is not shown in these schematics and only the Li_2S layer is highlighted near the entrance of a nanotube.

3.2 Experimental

3.2.1 Materials and Reagents

Halloysite nanotubes with a length of 300-600 nm, external diameter of 50-60 nm and inner lumen diameter of 10-15 nm were supplied by Applied Minerals Inc., NY. Sucrose, sulfur, ethylene diamine (EDA), toluene, N,N-dimethylformamide (DMF, 99.8%), bis(trifluoromethane-sulfonyl)imide (LiTFSI), $LiNO_3$, lithium hexafluorophosphate ($LiPF_6$, 99.99%), 1,3-Dioxanes (DOL) and Dimethoxyethane (DME, with DOL: DME, 1:1 by vol%), were purchased from Sigma-Aldrich (St Louis,

MO). Aluminum foil (250 μm thick), microporous polypropylene membrane (25μm thick) separator, and coin cells were purchased from MTI Corporation (Richmond, CA). All chemicals and materials were used without further purification or treatment unless specified.

3.2.2 Halloysite Preparation

Stock halloysite powders were first grinded in mortar to break up and remove large aggregates. The fine halloysite nanotubes were then treated with sulfuric acid (0.5-3 M) at 50-90℃ for 4-8 hours as described elsewhere (Abdullayev *et al*., 2012). The acid-etched samples were further filtered, washed, and dried prior to next step treatment. To increase halloysite conductivity, graphite-like carbon skin was introduced on the nanotube surface through a glucose hydrothermal treatment. Briefly, halloysites are loaded into a glucose aqueous solution (1.0 wt.%) and hydrothermally treated at 160℃ for 4 hours in a Teflon-lined autoclave. The dried samples were calcined in a quartz tube reactor at 800℃ for 3 hours at a heating rate of 3℃/min in a N_2 gas flow.

3.2.3 Sulfur Loading in Halloysites

Sulfur was loaded into halloysite nanotubes by solution impregnation. Sulfur powder was first dissolved in EDA or toluene to form a sulfur solution. The acid-etched halloysite nanotubes' powder was then mixed with a sulfur solution with a halloysite/sulfur ratio of 1:4 and incubated under strong agitation for 6 hours. After vacuum drying overnight, the powder was further moved into a quartz tube furnace. The furnace temperature was then elevated to 180℃ at a heating rate of 5℃/min under a N_2 environment. After reaching the desired temperature, the HNTs/sulfur samples were held there for another 2 hours to remove the solvent and re-disperse the sulfur coating

uniformly in the composites. The actual sulfur mass in the obtained HNTs/sulfur composites cathode was quantified with TGA prior to electrochemical measurement.

3.2.4 Material Characterization

Scanning electron microscopy (SEM) images were taken using a Hitachi S-4800 instrument. All samples (except halloysites with carbon skin) were sputter coated with gold to reduce the potential charging effect. The energy-dispersive X-ray spectroscopy (EDS) was conducted by the TEAM EDS analysis system integrated on SEM at 15kV.

Transmission electron microscopy (TEM) images were taken on a JEM-1400 TEM operated at 100 kV and a Hitachi H-9500 high-resolution TEM (HRTEM) at 300 kV. Samples were suspended in ethanol and dispersed on a copper grid coated with lacey carbon film before TEM imaging and analysis.

Nitrogen adsorption isotherms of halloysites were obtained at liquid N_2 temperature on a Micromeritics ASAP 2020 Surface Area and Porosity Analyzer. Before measurements, samples were degassed at 300 ℃ for 3 hours. The total surface area was calculated according to the Brunauer-Emmett-Teller (BET) method, and the pore volume and size distribution were obtained by the Barrett-Joyner-Halenda (BJH) analysis of the adsorption branch of the isotherm.

X-ray diffraction (XRD) patterns were recorded on a Bruker D8 Advance X-ray diffractometer using Cu Kα radiation at room temperature at 40 kV and 40mA. Data was collected with the 2θ range of 6-60°at a step size of 0.02°.

Thermo-gravimetric analysis (TGA) was done to monitor the weight loss of composite samples using a TGA 2050 Thermogravimetric Analyzer (TA Instruments,

Inc). The thermal scanning was performed from 30 to 600℃ at a ramp rate of 10℃/min in the air environment.

3.2.5 Battery Performance Tests

The sulfur cathode material was prepared by mixing 80 wt.% of HNTs/sulfur, 10 wt% of super P carbon black, and 10 wt% of polyvinylidene fluoride (PVdF) binder in N-methyl-2-pyrrolidone (NMP). The obtained slurry was then spread on a flat aluminum foil surface and dried in a vacuum oven at 120 ℃ for 12 hours to completely remove solvent. The dried samples were cut into discs and moved to an argon gas filled glove box prior to battery assembly.

The electrolyte was prepared by dissolving 1 M bis(tri-fluoromethanesulfonyl)imide (LiTFSI) and 0.1 M $LiNO_3$ in a mixture of 1,3-Dioxanes (DOL) and Dimethoxyethane (DME, with DOL: DME, 1:1 by vol%), with a microporous polypropylene membrane (25 μm thick) being used as the separator. The CR2032 coin cells were assembled, with the prepared HNTs/sulfur composites as the cathode and a lithium disc as the anode, in an argon-filled glove box. Their electrochemical performance was evaluated by galvanostatic charge/discharge cycling under different current rates. A voltage range of 1.8 and 2.8 V versus Li /Li was used in charge and discharge tests, with the specific capacity calculated based on the actual mass of sulfur content measured by TGA prior to assembly, with a typical load of ~2-10 mg. Electrochemical impedance spectroscopy (EIS) measurements were conducted on Auto-lab PGSTAT302 N electrochemical workstation (Metrohm, Switzerland).The ac perturbation signal was set at 10mV with a frequency range of 10^{-1}-10^{5}Hz.

3.3 Results and Discussion

3.3.1 Etched Halloysite Nanotubes

Halloysites are one type of natural clay mineral that has a similar chemical structure to kaolinite ($Al_4Si_4O_{10}(OH)_8nH_2O$, n=0 or 2) but different morphology. Unlike kaolinite's layered flakes, halloysites have aluminum oxide and silicon oxide layers alternatively swirling into multiple-layer rolls with a large lumen (**Figure 3-1**). Their one- dimensional hollow nanotube structure carries an aluminoxane octahedral lumen surface and a silica outer wall in hydrated states so that positive and negative charges are shown in the inner and outer surface, respectively. As shown in **Figure 3-2a&b**, halloysites used in this work originally have an external diameter of ~60 nm, a central lumen of ~15 nm and a length varying from 450 to 650 nm. The spacing between neighbor layers is ~0.70 nm (inset in **Figure 3-2b**). Such a hollow tubular structure gives a specific surface area of 52.7m^2g^{-1}, a pore volume of 0.163cm^3g^{-1}, and an average pore size of 17.8nm, calculated based on N_2 BET adsorption isotherm (**Table 3-1**). To expand the lumen space and shorten the nanotube length, halloysites were further etched with H_2SO_4 to remove some layers of aluminoxane inner rolls. This contributes to a decrease of the specific surface area to ca 44.8m^2g^{-1}, an increase of the pore volume to 0.205cm^3g^{-1}, and an increase in average pore size to 18.9nm (**Table 3-1**). As shown in **Figure 3-2c&2d**, the length and inner diameter of the central lumen of the etched halloysites is averagely changed to 250-350 nm and 15-25 nm, respectively (inset in **Figure 3-2d**). Their unique nanotube geometry, appropriate lumen size, and uniform lumen size distribution make them favorable sulfur confinement hosts for battery applications.

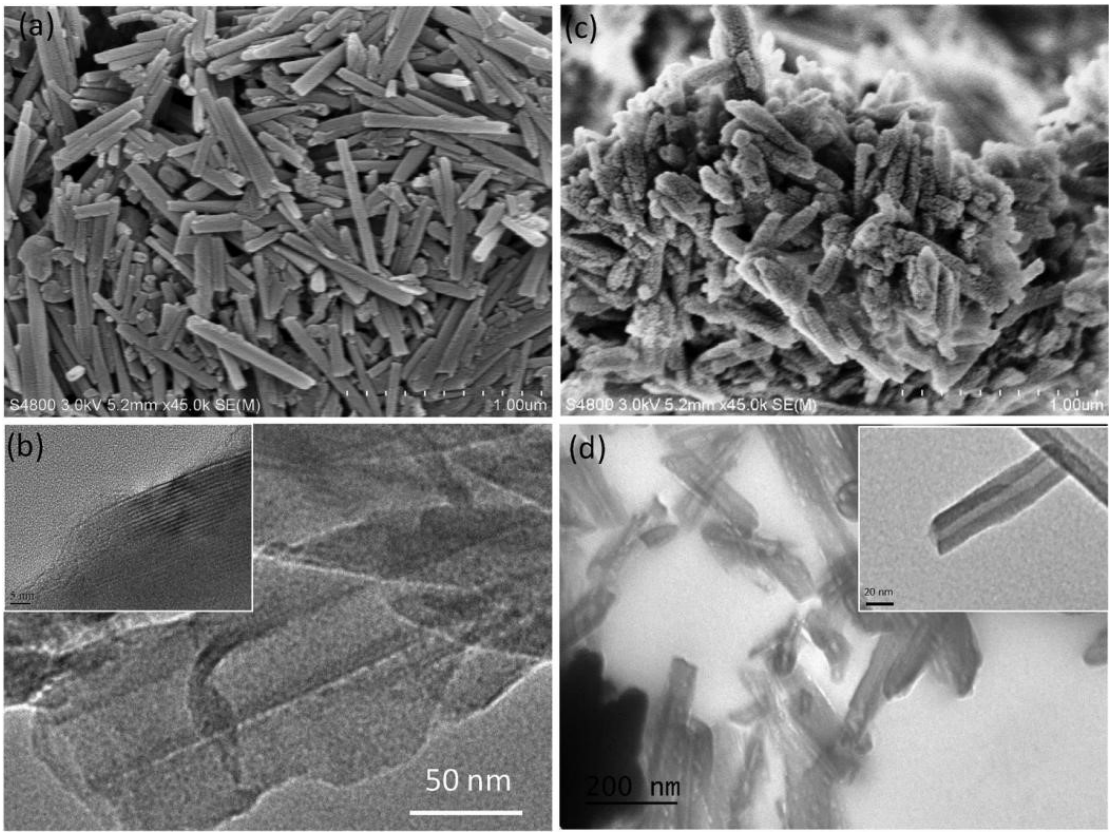

Figure 3-2: SEM (a,c) and TEM (b, d) images of halloysites: (a-b) untreated and (c-d) H_2SO_4 etched ones. Inset in panel (b) is the HR TEM image of halloysites.

Table 3-1: The texture properties of halloysite nanotubes (HNTs) and their etched counterparts (E-HNTs).

Sample	BET (m^2g^{-1})	Pore Vol (cm^3g^{-1})	Pore Size (nm)
HNTs	52.7	0.163	17.8
E-HNTs	44.8	0.205	18.9

3.3.2 Carbon Coating and Sulfur Loading in Halloysite Nanotubes

Before sulfur loading, glucose is coated on individual halloysite nanotubes and further converted into graphite-like carbon skin to make them electrically conductive. As shown in **Figure 3-3a**, a thin carbon covering is clearly seen on an individual halloysite nanotube, which presents as thin graphite flakes in some locations. The electrical resistance of these carbon-coated halloysites is ~400Ω, which is significantly different compared to the uncoated counterparts' electrical resistance of ~11MΩ (Note: to prepare these samples for resistance measurement, only PVDF binder was used to cast halloysites on aluminum foil; no conductive additives were added). These results demonstrate the successful production of conductive halloysites. Overlaps among different carbon-coated halloysites in their assembled nanotube clusters create an electrically conductive network to facilitate charge and discharge performance of the received composite cathode materials.

Sulfur was loaded into the halloysites through a solution impregnation method for both untreated and acid etched halloysites. Elemental sulfur was initially dissolved in an appropriate solvent and quickly mixed with halloysite powders for 6 hours. In this way, sulfur is introduced both in the inner lumen and on the outer surface of the halloysite nanotubes (**Figure 3-3b&3-4**). For sulfur loaded inside the central lumen space of halloysites, their size varies from several nanometers to around the diameter of lumen due to the space restriction, as shown in **Figure 3-3b**. We would like to underline that the TEM image in **Figure 3-3b** is a unique one because it shows directly loaded sulfur particles occupying approximately one half of the lumen volume. Earlier, direct inner loading of halloysite was demonstrated only with metal particles, which have high

affinity when compared with a ceramic tube's walls (Glotov *et al*., 2017). Sulfur encapsulated in the lumen of halloysites is estimated as ca. 10 wt. % loading respective to the total tube's mass. We assume that an essential part of sulfur is deposited at nanotubes' external surface. Without geometric restriction, sulfur nanoparticles located outside halloysites reach 30 nm or bigger (**Figure 3-4d)**. Further annealing process helps improve the coating uniformity of sulfur on their host surface. EDS element mapping images in low magnification clearly reveal the overall homogeneous dispersion of sulfur particles in the composites, rather than a mixture of large aggregates of halloysites and sulfur particles (**Figure 3-3c**). During this annealing process, the sulfur coating outside the surface of individual halloysites also tends to fuse together with the nanotubes. This leads to neighbor halloysites assembling into clusters and creating many nanoscale isolated voids in between (**Figure 3-4**). These nanovoids, when occupied by liquid electrolyte and later formed solid-electrolyte interphase (SEI) during battery tests, provide restricted space to withhold early dissolved polysulfides instead of their quick dilution in bulk electrolyte solution, as schematically illustrated in **Figure 3-3c**. This contributes to a high viscous local environment around the halloysite host to slow down further polysulfide dissolution. The additional migration tortuosity created by these isolated nanodomains also delays polysulfide shuttle towards the anode. All these features together help suppress associated polysulfide issues in Li-S batteries, which is beneficial for their long-term cycling stability.

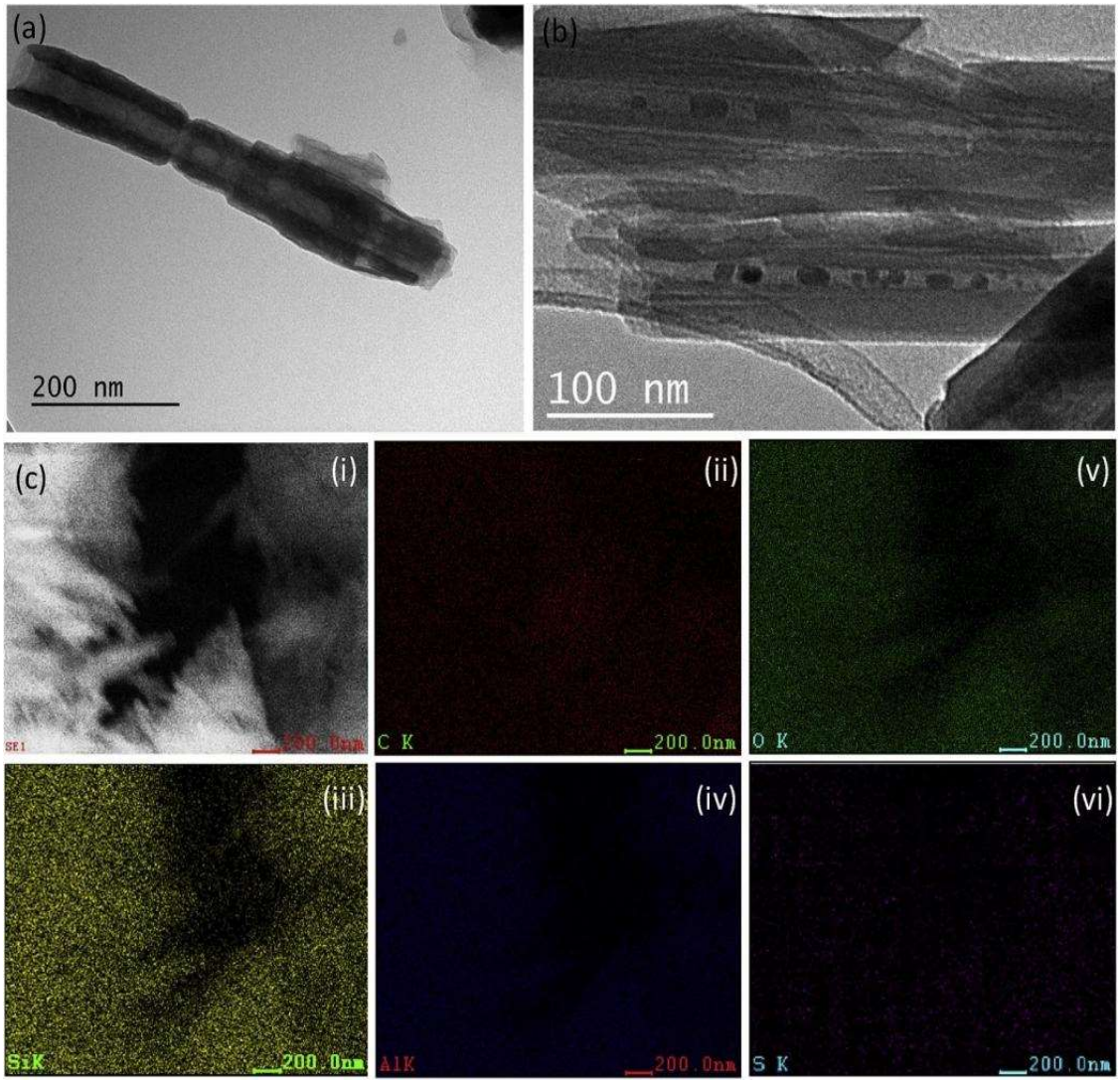

Figure 3-3: TEM images of (a) halloysites with glucose- derived carbon coating and (b) sulfur-loaded halloysite/sulfur composites; (c) EDS element mapping images of sulfur-loaded halloysite/sulfur composites. In panel c, subpanel c(i) is a SE image of halloysite/ sulfur composite location where element mapping analysis was done and subpanel. c(ii-vi) are x-ray images for carbon, oxygen, silicon, aluminum, and sulfur elements, respectively.

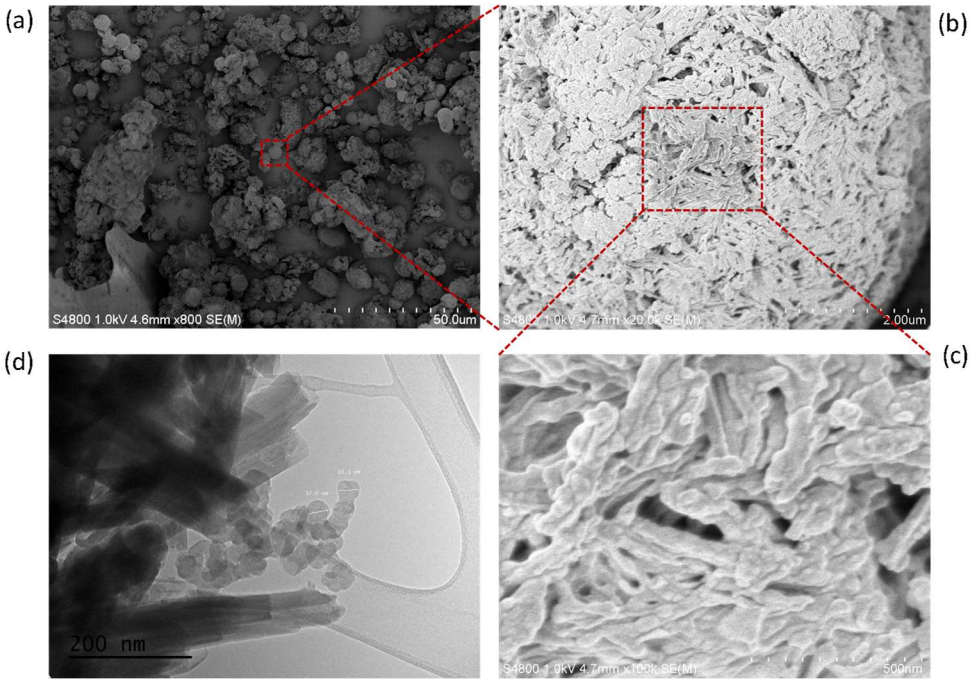

Figure 3-4: (a-c) SEM images and (d) a TEM image of halloysite/sulfur composites. In panel d, those spherical objects outside halloysite nanotubes are sulfur nanoparticles.

The XRD spectrum of HNT/sulfur composites exhibits both characteristic peaks from sulfur and halloysites (**Figure 3-5a**). The strong sulfur peaks indicate the high sulfur load on halloysites, while the actual loading dosage varies with available surface area, pore volume of halloysites, and their wettability to the sulfur solution. Two different solvents, toluene and EDA, which can dissolve sulfur completely, were used for sulfur loading in this work. As shown in **Figure 3-5b**, for untreated halloysite nanotubes, sulfur loading dosage is 7.6% when a sulfur/toluene solution is used as the loading media and 30% when a sulfur/EDA solution is used. Due to the hydrated status of the halloysite surface, the higher loading dosage with a sulfur/EDA solution is probably attributed to two different effects. One comes from the strong hydrophilicity of halloysites, whose outer surface is mostly composed of SiO_2 and the inner surface of Al_2O_3. When hydrated,

halloysites carry many hydroxyl group pendants on the surface with moisture condensed on it. As EDA is completely soluble in water, the capillary forces help the sulfur/EDA solution reach deep in the nanotubes to have more sulfur loaded. The other effect lies on the strong acidity of halloysites on their lumen surface. The inner surface of a halloysite lumen has Al_2O_3 dominates, which provide positive charges and solid acidity. Their acidic sites, when interacting with alkaline compounds like EDA, help pull them out of the sulfur-EDA complex so that sulfur can disperse over the framework of the halloysites. To prove the strong interactions between halloysites and EDA, a TGA measurement was done on a halloysite sample pre-adsorbed EDA. This EDA/halloysites sample was first placed in an ultra-dry glove box filled with Ar gas. Water content was less than 0.1 ppm prior to the TGA test to avoid moisture condensation inside the halloysites. As shown in **Figure 3-6**, the weight loss contributed by EDA desorption shifts to a higher temperature position (note: the boiling point of EDA is 116℃), revealing the strong surface interactions of EDA and halloysites.

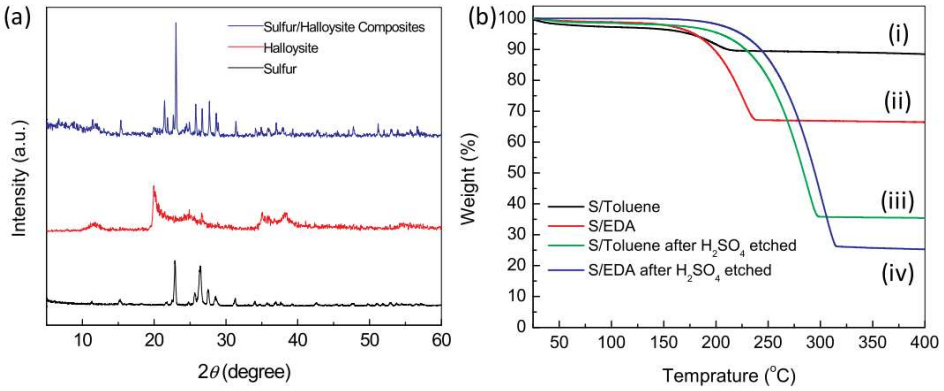

Figure 3-5: (a) XRD spectrum of halloysite/sulfur composites with spectra of halloysites and sulfur are also included for comparison purpose; (b) TGA spectra of sulfur- loaded halloysites with various sulfur solutions: (I, ii) sulfur in toluene and (iii, iv) sulfur in ethylene diamine; (i, iii) halloysite nanotubes without H 2SO4 etching and (ii, iv) with H2SO4 etching.

The H_2SO_4 etching further increases lumen diameter and volume of the halloysite nanotubes (**Table 3-1**). As a result, the sulfur loading capacity in etched halloysites is further improved. As shown in **Figure 3-5b**, the loading dosage of sulfur in etched halloysites reaches 62.5 wt. % and 75.5% for a sulfur/toluene and sulfur/EDA loading solution, respectively. For all sulfur loaded in halloysites, a portion of ca 10 wt. % is estimated to be located inside the lumen of the nanotubes, while the rest is located outside. Such estimation was made by calculating the mass percentage change after sulfur filled the hollow space of halloysites. Assuming an average halloysite diameter is 60 nm, the weight percentage of sulfur, if completely filling the lumen of a halloysite nanotube, is around 9% (assuming 20 nm in diameter of the etched halloysite lumen) and ~14% (in diameter of the etched halloysite lumen) when the density of sulfur and halloysites are adopted as 2.0 and 2.5 g/cm^3, respectively (note: halloysite density varies between 2.0 and 2.65 g/cm^3, depending on their original sources). To verify our estimation experimentally, sulfur-loaded halloysite samples were washed with abundant toluene

multiple times, each lasting for 10 minutes. As shown in **Figure 3-7**, the weight loss of halloysite/sulfur composites on the TGA curves is ~15% after one washing step, which reduces to ~7% when conducting an additional washing step. In comparison, the weight loss of sulfur/halloysites composites after deep washing (24 hour immersion in toluene) is only~2%, which is believed to be contributed by solvent residue in halloysites. Based on these results, we believe that after the first washing step, most sulfur attached to the outer surface is washed away and that 15% weight loss is contributed mainly by sulfur inside the lumen of halloysites and some leftover on the outer surface of the halloysites. After the second washing step, all sulfur on the outer surface and some inside the halloysite nanotubes is washed away. These results are inconsistent with our calculation estimation on sulfur loading dosage in halloysite lumen based on its dimensions. Nevertheless, the highest loading dosage from the sulfur/ EDA solution makes them preferred to serve as cathode materials. Therefore, in the battery test, sulfur was loaded into etched halloysite nanotube samples through EDA media unless specified.

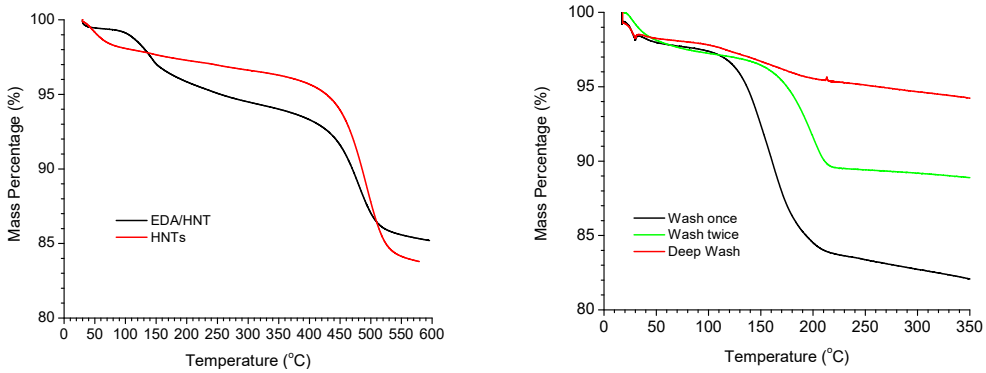

Figure 3-6: (a) TGA result of EDA adsorbed halloysites. The TGA result of bulk halloysites is also shown for comparison purposes. (b)TGA of sulfur-loaded halloysites after various washing steps.

3.3.3 Battery Testing Performance

The electrochemical performance of the HNTs/sulfur composites cathode was done via galvanostatic charge/discharge experiments. **Figure 3-7a&b** shows the voltage profiles (plot of potential against specific capacity) at the end of the 1st, 10th, 20th, and 50th galvanostatic charge/discharge cycle of the composite cathodes for halloysite nanotubes of two different lengths (one with an average length of 450-650 nm and the other of 250-350 nm). For each case, two typical potential plateaus during the lithiation process are clearly shown on the discharge curves: a short one around 2.3-2.25 V and a long one near 2.1V, attributed to the transformation of S_8 to Li_2S_4 and L_2S_4 to L_2S species, respectively. The first-cycle charge capacity of composites with long halloysites reaches 949 mAh g^{-1}, which is higher than the composites with short nanotubes (831 $mAhg^{-1}$). However, similar discharge capacity was achieved (long nanotube cathode: 722 $mAhg^{-1}$; short nanotube cathode: 737 $mAhg^{-1}$). This gives a low initial coulombic efficiency (i.e., discharge capacity/charge capacity) of 76% for composites having long nanotubes and 89% for those with short nanotubes. Such low coulombic efficiency continues in the composite cathode including long halloysite nanotubes during late cycling tests (**Figure 3-7a**). But for composites with etched, short halloysite nanotubes (i.e., with a length/diameter ratio of 10 or less), their coulombic efficiency quickly approaches nearly 100% in late cycles (**Figure 3-7b**). Their specific capacity for both charge and discharge steps also shows a good retention ratio in the next 50 cycles. Such improvements are attributed to the different migration situations of Li^+ ions for entering or leaving nanotubes of various length-to-diameter ratios, which will be discussed in the

next section. With satisfactory discharge/charge performance, only composite cathodes with short, etched halloysite nanotubes were shown in rate and stability cycling tests.

Good rate performance was also achieved for those composites with short halloysite nanotubes. As shown in **Figure 3-7c**, a specific capacity around 710 mAh g^{-1} is obtained at a current rate of 0.1C with satisfactory coulombic efficiency. Such sustained charge/discharge capacity can be fully recovered when the current rate is reduced back to 0.1C after a sequential increase of the current rate to 0.5C, 1C, and 2C. Unlike largely matched charge and discharge capacity at small current rates (0.1C and 0.5C), elevated current rates (1C and 2C) cause obvious capacity differences between discharge and charge steps, with a coulombic efficiency dropped to 92-94% (**Figure 3-7c**). Similar to what happened in the composite cathode with long halloysite nanotubes, fast charge/ discharge rates also cause similar migration issues of Li^+ ions inside nanotubes and heterogeneous lithiation levels along the depth direction of nanotubes. Nonetheless, the charge and discharge capacity at the same current rate is sustained with only minor variations, indicating the lithiation or delithiation situations in the composites are similar to what occurred during short-term cycling. Long-term cycling stability was also confirmed with those HNTs/sulfur composites. For over 250 cycles, the capacity of the composite cathode retains 84% of 657 $mAhg^{-1}$ and nearly 100% of the coulombic efficiency (**Figure 3-7d**). Similar capacity retention performance is also found in composite cathodes made by halloysites without carbon coating (**Figure 3-8**). However, because of their low conductivity, the overall capacity of composite cathodes involving uncoated halloysites is much smaller than those using carbon-coated ones. These electrochemical results suggest that the utilization of sulfur is greatly improved in this

new type of HNTs/sulfur composite during long-term cycling. This improvement can be attributed to the two important roles of halloysites in the composite cathode: (i) the confinement effect of the hollow tubular structure of halloysites, which preserves the size of sulfur nanoparticles in their nanotube lumen to suppress the size evolution during cycling; (ii) the nanoscale voids created by assembled halloysite clusters, known as inter-nanotubes, which help create many small, isolated domains around solid-electrolyte contact area to down regulate the dissolution of polysulfides and add an extra diffusion barrier for the dissolved polysulfides to further slow down their migration.

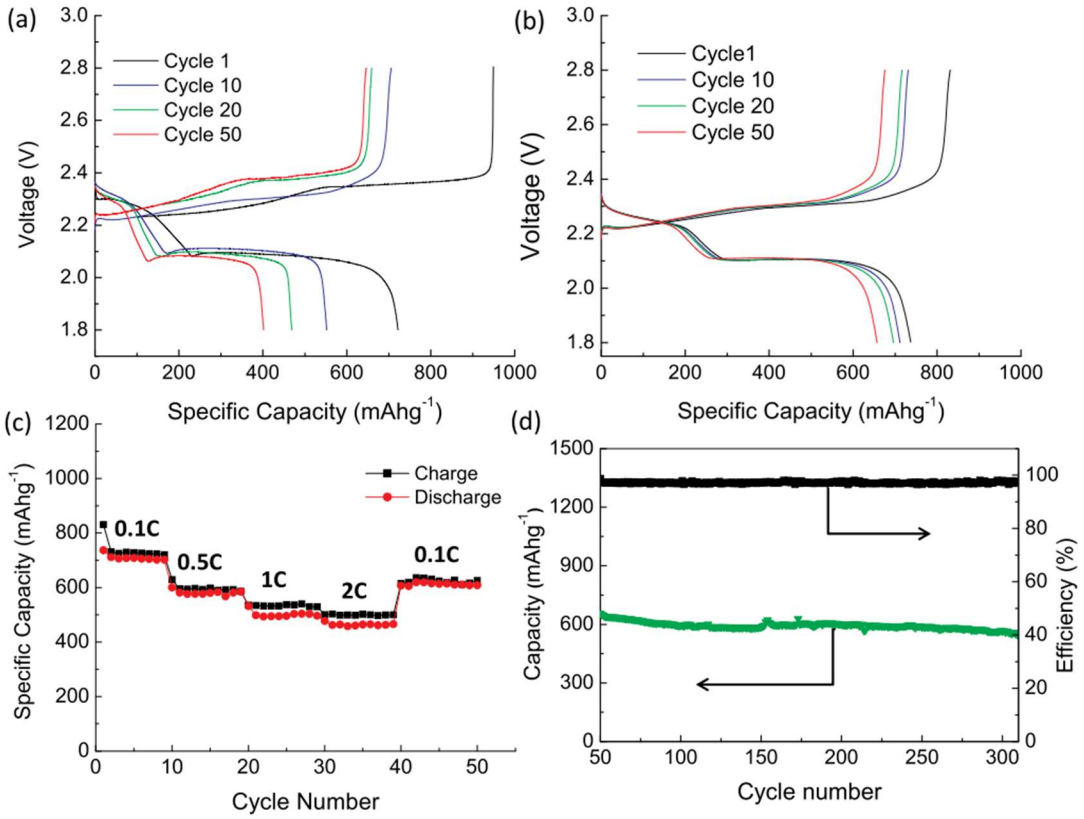

Figure 3-7: (a) The voltage profiles for the 1st, 10th, 20th, and 50th galvanostatic charge-discharge cycles of sulfur/halloysites composite cathode with long halloysite nanotubes (a) and short halloysite nanotubes (b); Different current rates (c) and cycling performances/coulombic efficiency (d) of the same composite cathode used in panel (b).

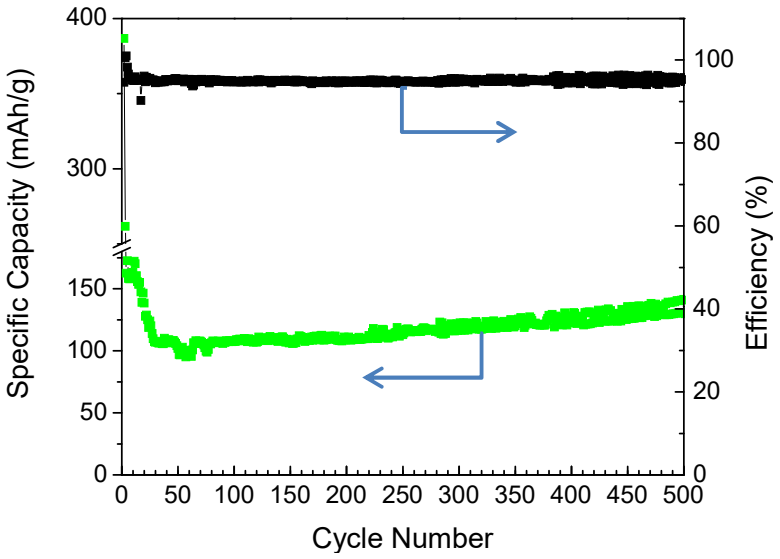

Figure 3-8: The cycle performance of sulfur/halloysite (uncoated) cathode.

To better understand the effect of charge/discharge cycles on the electrochemical performance of Li-S batteries, Electrochemical Impedance Spectra (EIS) were collected to analyze the electrochemical behaviors of HNTs/sulfur composite cells after pre-cycling (10 cycles) and long-term cycling (200 cycles) tests. The Nyquist plots exhibit a semi-circle in the high-medium frequency region for both cells (**Figure 3-9a**). An equivalent circuit model, consisting of electrolyte resistance (R_E), SEI layer resistance (R_{SEI}), and charge transfer resistance (R_{CT}), was applied to fit the EIS spectrum data of the composite cells (**Figure 3-9b**). As shown in **Figure 3-9c**, the resistance contributed by the electrolyte and SEI layer is relatively small when compared to the charge transfer resistance in this HNTs/sulfur composite cathode, both before and after long-term cycling. A small initial R_E with a moderate increase of R_E value after 200 cycles demonstrates the sustained conductance of the electrolyte and electronic contact of the composite cathode, thanks to the successful suppression of polysulfide dissolution and migration in electrolytes. A small initial R_{SEI} with a relatively large increase of its value

after long-term cycling suggests that the diffusion of Li^+ ions to the surface of the active material has a noticeable effect. A large R_{CT} after long-term cycling indicates slow charge transfer kinetics, most likely caused by gradual deposition of insulating Li_2S and Li_2S_2 near the entrance of halloysite nanotubes.

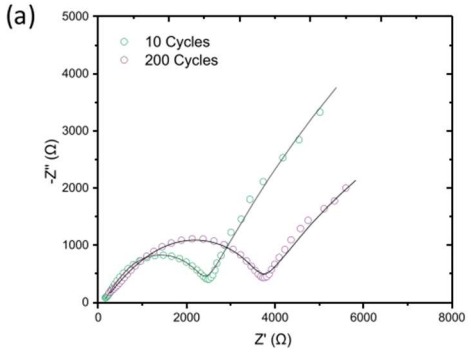

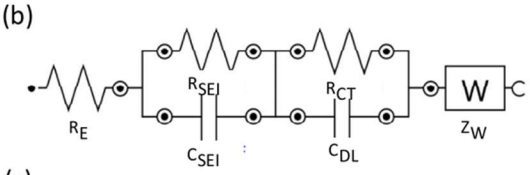

(c)

Cycle	R_s (Ω)	R_{SEI} (Ω)	R_{CT} (kΩ)	Zw
10	156	199	1.56	108
200	246	550	2.53	171

Figure 3-9: Electrochemical Impedance Spectra characterization of halloysite/sulfur composite cathode. (a,b) Nyquist plots of EIS profile for halloysite/sulfur composite cathode after 10 cycles (a) and 200 cycles (b); (c) equivalent circuits for fitting of Nyquist plots. R_E: the internal electrolyte resistance, R_{SEI}: the SEI layer resistance, R_{CT}: the charge-transfer resistance.

The EIS results reveal that the major resistance comes from the charge transfer interface, suggesting the polysulfide concentration in SEI and electrolytes is relatively low when insulating Li_2S and Li_2S_2 species are deposited on the solid surface, particularly near nanotube entrances (**Figure 3-10**). This is attributed to the unique diffusion behaviors of Li^+ ions in HNT/sulfur composites. In this new composite cathode, sulfur is loaded both inside and outside of halloysite nanotubes. The sulfur particles that are deposited on the external surface of nanotubes experience similar interactions with Li^+ ions as in many other nanostructured cathode materials. One main function of halloysite nanotubes is to aid in the dispersal of the active material, increasing their exposure area to the incoming Li^+ ions so that their uptake speed and capacity are

enhanced. The assembled clusters of halloysites also create increased inter-nanotube space which is occupied by liquid electrolyte and the solid-electrolyte interphase (SEI). These separated nanodomains force the dissolved polysulfides to stay close to the solid surface instead of diluting into the bulk electrolyte solution. The assembled halloysites themselves also create additional diffusion barriers by increasing migration tortuosity for those dissolved polysulfides. As a result, the shuttle effect of the polysulfides is suppressed and the associated fading capacity during battery charge and discharge processes is mitigated.

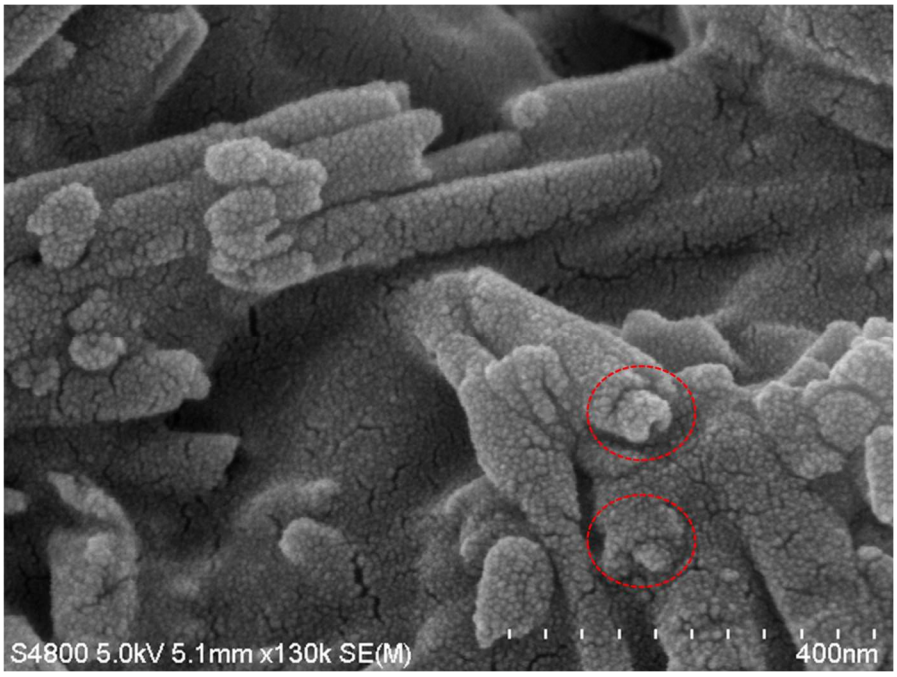

Figure 3-10: A SEM image of halloysite cathode material after cycling. The circled area shows particle aggregations near nanotube entrance.

However, sulfur encapsulated in halloysite nanotubes faces some different migration situations. As Li^+ ions move out of nanotubes, insulating Li_2S and Li_2S_2 species transform to polysulfides, starting from the entrance of the nanotube host. The high solubility of these products in the electrolyte solution promotes the movement of Li^+ ions

from nanotubes during the charge step **Figure 3-1c**(ii)). When the discharge process initiates, the opposite transformation reactions occur and Li^+ ions continuously arrive at the openings of halloysite nanotubes. However, due to the restrictive geometry at the entrances of nanotubes, excessive Li^+ ions accumulate both within and outside of the nanotubes. The enriched Li^+ ions in these regions allow the earlier formed polysulfides with low lithiation degree to continue their transformation into a fully lithiated, insoluble species (i.e., Li_2S and Li_2S_2). When such transformations occur too quickly, the newly formed solid, fully lithiated species build extra barriers to slow down the further migration of Li^+ ions into the deep lumen space of halloysites (**Figure 3-1c**(iii)). As a result, fewer Li^+ ions can reach unreacted sulfur deep in nanotubes during the discharge stage. This leaves some lean lithium sulfur species behind, resulting in a smaller capacity during the discharge step. As this uptake difference of Li^+ ions between charge and discharge stages is attributed to the high-aspect ratio geometry of halloysite nanotubes, inward migration into nanotubes (i.e., discharge) becomes more challenging for composites possessing long nanotubes. A large difference in the discharge and charge capacity is shown in each cycle for those composites, and a rapid capacity decay occurs as cycling continues (**Figure 3-7a**). Inversely, composites with short nanotubes achieve much better capacity retention ratio and coulombic efficiency (**Figure 3-7b**). However, if the current rate increases (i.e., 1C and 2C), both composites with long and short nanotubes experience similar migration of Li^+ ions, where outward movement from nanotubes (during charge step) is easier than inward into nanotubes (during discharge step). As shown in **Figure 3-7c**, an obvious difference in charge and discharge capacity is clearly observed for the composites with short halloysite nanotubes at 1C and 2C current

rates. In battery applications, high current rates are essential for charging steps to avoid long wait times, while inter- mediate current rates are often preferred in the discharge stage for extended capacity use of batteries. Therefore, HNTs/sulfur composites with different Li^+ ion diffusion behaviors between charge and discharge stages show high potential for use as cathode material in Li-S batteries.

3.4 Conclusions

To conclude, a new variety of core-shell clay nanotube-HNT/sulfur composites is introduced to confine and disperse highly loaded sulfur nanoparticles. The available nanoscale space in both the lumen of halloysite nanotubes and between assembled halloysite clusters also helps sup- press the dissolution and migration of polysulfides in liquid electrolyte solution. Through appropriate treatment, the sulfur loading in the composites could reach as high as 80 wt.%, in which around 10% encapsulated inside the nanotubes with the rest remaining outside. When assembled as the cathode of Li-S batteries, the HNTs/sulfur composites successfully improved the cycling stability, retaining ~84% of the starting capacity for over 250 cycles. The migration difference of Li^+ ions in and out of the hollow nanostructure of halloysites depends on the length of nanotubes and the current rate of discharge. Those with small aspect ratios show good sulfur utilization and no obvious capacity fading at intermediate discharge rates.

CHAPTER 4

NANOFIBER-IN-MICROFIBER CARBON/SILICON COMPOSITE ANODE WITH HIGH SILICON CONTENT FOR LITHIUM-ION BATTERIES

4.1 Introduction

Rechargeable lithium-ion batteries (LIBs) currently dominate the mobile electronics market because of their high energy density, long cycle life, and promising power performance (Placke *et al.*, 2017; Chen *et al.*, 2020; Choi *et al.*, 2016). However, commercial LIBs have been stretched nearly to their limit, employing metal oxide cathodes and graphite anodes that do not yet meet the energy density (energy/volume) and specific capacity (energy/weight) demands of other critical energy storage applications, such as electric transportation or stationary power storage, which require much higher energy/power capacity (Ahmad *et al.*, 2021; Tarascon *et al.*, 2001; Thackeray *et al*., 2012). Tremendous efforts have been made over the past decade in the search for new active materials and/or more desirable configurations of electrodes for LIBs (Park *et al.*, 2010; Jeong *et al*., 2011; Kasavajjula *et al*., 2007; Endo *et al*., 2000). Adoption of silicon/carbon composites seems to be the natural conclusion for use in anodes, due to their potential to inherit carbon's high electrical conductivity and silicon's high lithium capacity (Zhang *et al.*, 2004; Szczech *et al*., 2011; Li *et al*., 1999). Among various silicon/carbon composite anode materials, nanostructured silicon such as

nanoparticles (Nava *et al.*, 2016; Zhang *et al*., 2021; Jia *et al*., 2020) and nanowires (Chan *et al.*, 2008; Xu *et al*., 2010; Wu *et al*., 2012) are preferred formats to mitigate the adverse challenges of silicon anodes, namely electrode pulverization and capacity loss during repeated charge/discharge cycles due to dramatic volume change (more than 300%) and consequent stress induction (Wu *et al.*, 2012). Despite improvements in capacity retention and cycling stability, the adoption of nanostructured silicon still faces many challenges in compliance with existing manufacturing lines. The synthesis of silicon nanowires generally involves wet-chemical processes, toxic silane gas, and/or templates (Chan *et al.*, 2010; Xie *et al*., 2011; Magasinski *et al*., 2010), which are often expensive and undesirable for large scale production. Although silicon nanoparticles are available in large-scale, dispersing them in carbon matrix via simple mechanical mixing or ball milling did not work well to improve cycling stability and capacity retention, particular for large energy density demands with high silicon content (Chae *et al.*, 2020; Schmuch *et al.*, 2018; Zhang *et al*., 2021). Composites with "core-shell", "shell-core-shell", or "yolk-shell" structure with silicon nanoparticles or nanowires in carbon nanofibers were found to work better (Huang *et al.*, 2021; Ye *et al.*, 2021; Chen *al*., 2021 Hwang *et al.*, 2012; Liu *et al*., 2012). Their one-dimensional nanostructure network allows quick transport of lithium ions to active elements (e.g., silicon) and high insertion/extraction efficiency (Wang *et al.*, 2015). Moreover, the continuous, interconnected network structure allows them to serve as the sole current collector, requiring no additional binding materials (Deng *et al.*, 2007).

Despite a successful proof-of-concept, these composite nanofiber materials still leave much to be desired in terms of processing and manufacturing for high throughput

and desired performance (Agubra *et al.*, 2016; Luo *et al.*, 2017; Li *et al.*, 2017). High silicon content is essential for anodes of large energy capacity, but their continuous addition in polymers can lead to many challenges, such as a dramatic increase of the processing fluid viscosity during fiber production, collapsed nanofibers, or loss of ductility in nanofibers. This automatically sets a maximum silicon mass allowance in a particular polymer solution. For example, the most popular carbon nanofiber material, polyacrylonitrile (PAN), allows up to 40% of mass content in its N, N-dimethylformamide (DMF) solution with a reasonable processing pressure drop during fluid transport (Wang *et al.*, 2015). In contrast, a polyvinyl alcohol (PVA) aqueous solution allows up to 80% silicon content while still retaining an acceptable processing viscosity (Kim *et al.*, 2014). However, high carbon loss of PVA during further carbonization can make the carbon/silicon nanofibers derived from PVA/Si composites easily lose flexibility or even pulverize their nanofiber structure. When their silicon content becomes very high, binding materials must be added to stitch the broken short composite nanofibers together. To achieve composite nanofibers with high silicon content and ductility of long fiber network, we present a new silicon/carbon composite configuration with high silicon content and flexible fibrous mat morphology. The nanofiber-in-microfiber composite fiber mats were prepared through a coaxial electrospinning process. A PVA aqueous solution was used as the middle electrospinning fluid with silicon nanoparticles (25-50% content) dispersed throughout prior to electrospinning. A PAN/DMF (5-10 wt.%) solution was introduced in the sheath stream to wrap up the silicon-rich nanofibers and serve as a ductile shell to help hold the fibrous structure of silicon-rich composites inside after great mass loss during later carbonization

in N_2 gas. In these core-shell silicon/carbon composite nanofibers, silicon nanoparticles serve as the active materials for Li ion host; PVA helps hold the silicon nanoparticles in a short nanofiber format; and PAN works as the outer layer of composites nanofibers to retain their fibrous morphology and provide the essential electron conductivity and flexibility needed to serve as anodes without metal collectors. The produced nanofiber-in-microfiber carbon/silicon composite nanofibers were further tested for their electrochemical performance.

4.2 Experimental

4.2.1 Chemicals

Polyacrylonitrile (PAN, average MW 150,000), N, N-dimethylformamide (DMF, 99.8%), Polyvinyl alcohol (PVA, average MW 75,000), lithium hexafluorophosphate (LiPF6, 99.99%), ethylene carbonate (EC, 99%), and diethyl carbonate (DEC, 99%), were purchased from Sigma-Aldrich (St Louis, MO). Si nanoparticles with an average diameter of ~20nm were purchased from MTI Corporation (Richmond, CA). All chemicals were used without further purification unless specified.

4.2.2 Materials Preparation

The nanofiber-in-microfiber composite mat was prepared using a coaxial electrospinning process, followed by carbonization. Typically, PAN/DMF (2-5 wt.%) and PVA/H_2O (10 wt.%) solutions were first prepared. Si nanoparticles (25-50 wt.%) were then dispersed in the pre-made PVA aqueous solution under agitation. The PVA/Si suspension was then loaded as the inner fluid of the co-axial electrospinning setup (**Figure 4-1**) and pumped at a flow rate of 0.75 ml h^{-1} through the center metallic nozzles. A PAN/DMF solution was loaded as the sheath fluid. A directional current electric bias

(24 kV) was added between the central metallic needle end and a grounded aluminum pan collector with a needle-to-collector distance of 15 cm through Gamma ES-40P power supply (Gamma High Voltage Research, Inc). The electrospun composite fibers (denoted as "PAN/Si/PVA") were then collected and stabilized in air at 280 °C for 6 h (with a heating rate of 5 °C min^{-1}). The fiber mats were further carbonized at 700 °C for 1 h in argon gas (with a heating rate of 2 °C min^{-1}) to produce nanofiber-in-microfiber carbon/silicon composite nanofibers (denoted as "C/Si composite fibers" in later description). For comparison purposes, PVA/Si composite nanofibers (without the addition of PAN coating) were also prepared and carbonized in the same process (denoted as "PVA/Si").

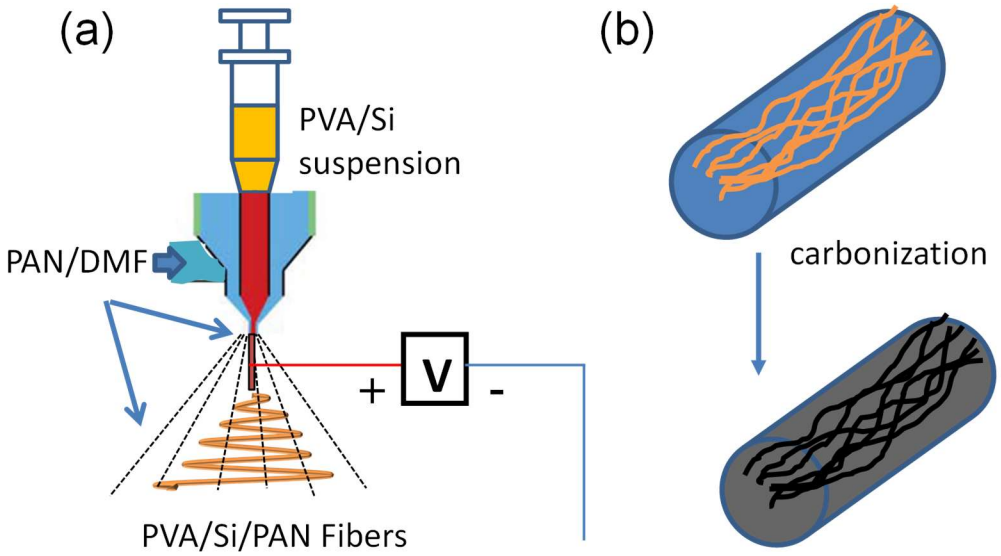

Figure 4-1: Schematic of the coaxial electrospinning process in the manufacture of nanofiber-in-microfiber composite fiber mat (a) and nanofiber bundles in microfiber configuration of the formed 3D anode.

4.2.3 Characterization

Scanning electron microscopy (SEM) images were taken using a Hitachi S-4800 instrument at 1.0 kV. All samples were sputter coated with gold to reduce the potential charging effect. The energy-dispersive X-ray spectroscopy (EDS) was conducted by TEAM EDS analysis system installed on SEM at 10 kV. The cross-section structure of composite fibers was characterized by transmission electron microscopy (TEM, JEOL 1400, JEOL).

Thermo-gravimetric analysis (TGA) was done to monitor the weight loss of nanofiber samples using a TGA 2050 Thermogravimetric Analyzer (TA Instruments, Inc). The thermal scanning was performed from 30 to 800 °C at a ramp rate of 10 °C min^{-1} in an air environment.

The X-ray photoelectron spectroscopy (XPS) analysis was done on a Scienta Omicron instrument with the following operation conditions: 10 sweeps for the survey scans and 200 sweeps for each of C 1s, Si 2p and N 1s detailed scans. The pass energy was set to 40 eV with a step size of 0.2 eV and a dwell time of 200 milliseconds for all samples.

4.2.4 Electrochemical Performance Evaluation

Electrochemical performance was evaluated using the standard 2032 coin cells (MTI Corp). The produced nanofiber mats (~3 mg) were used as the working electrode directly without adding any binder or conductive materials. These mats are mechanically flexible and can be easily bent, folded, or rolled into a wound spiral configuration (Figure 1b). Lithium chips of 250 μm in thickness (MTI Corp) and polypropylene membrane of 25 μm in thickness (Celgard, LLC) were used as the counter electrode and separator,

respectively. The electrolyte solution used in tests was 1 M $LiPF_6$ in 1:1 (v/v) EC: DEC. Coin cells were assembled in a high-purity argon-filled glove box. The galvanostatic charge/discharge characteristics were recorded with an MTI battery-testing system (model number BST8-WA) in a voltage range of 0.01-2.0 V with a current density of 50 mAg^{-1} at room temperature.

4.3 Results and Discussion

4.3.1 Morphology of PVA/silicon Nanofiber

The morphology of composites composed of PVA/silicon nanofiber bundles in PAN microfibers are shown in **Figure 4-2**. As the PAN outer layer is thick enough to fully wrap up PVA/silicon nanofibers, the composite microfibers have a taut, smooth surface (**Figure 4-2a**). The average diameter of these composite microfibers varies from 5-9 μm, on which silicon nanoparticles or polymer nanofibers are attached in a scattered formation. Within the microfibers, the cellular structure of the PVA/silicon nanofibers can be clearly seen (**Figure 4-2b**). To reveal how PVA/silicon nanofibers were wrapped inside PAN microfibers, TEM images of the composite microfibers were taken. As shown in **Figure 4-2c**, PVA/silicon nanofibers with an average diameter 300-600nm are present with well-reserved nanofiber morphology. Silicon nanoparticles are encapsulated in individual PVA nanofibers like bead chains (**Figure 4-2c**). Occasional aggregations are found inside nanofibers at entangled locations (inset of **Figure 4-2c**). Element mapping was done using EDS to further reveal the dispersion status of silicon nanoparticles in composite microfibers. As shown in **Figure 4-2d**, silicon nanoparticles distribute uniformly in the carbon domains of the composite microfibers.

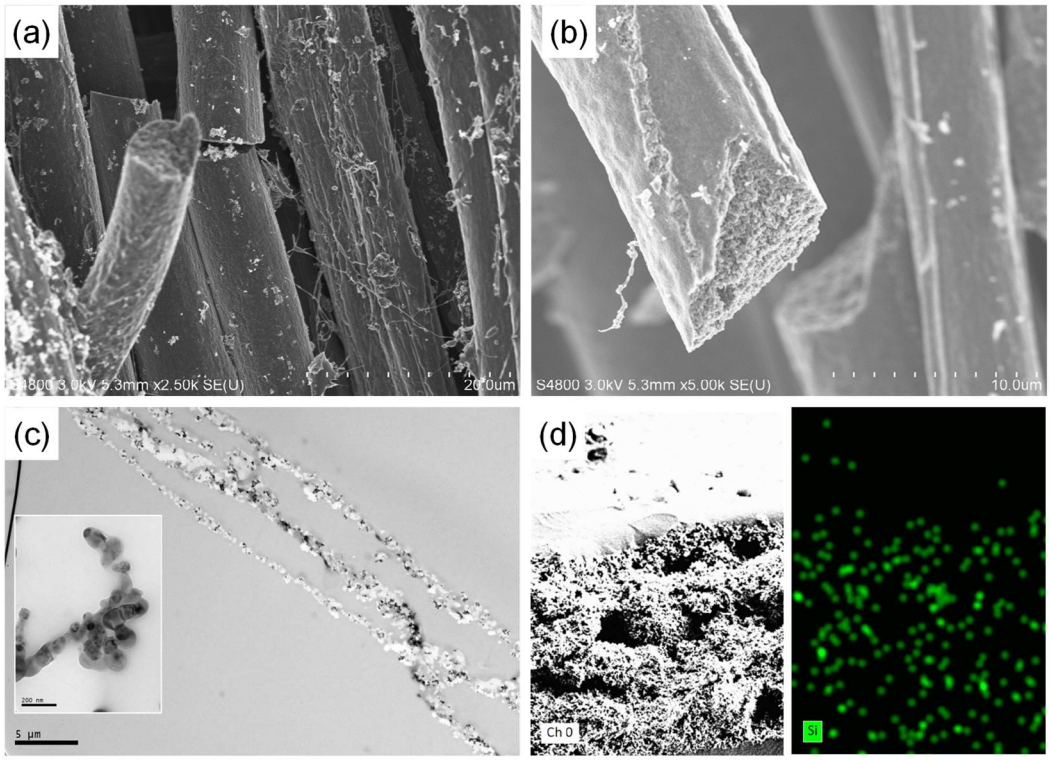

Figure 4-2: SEM (a, b), TEM (c), and EDS elemental mapping (d) images of PVA/Si/PAN fibers with an original Si/PVA ratio of 1:3.

4.3.2 SEM Analysis

As carbonization leaves only a thin carbon skin on PVA/silicon nanofibers to maintain their integrity, the carbonized composites were further used to discover the overall assembly status of silicon nanoparticles in original composite fibers. PVA/silicon nanofibers with different initial silicon-to-polymer mixing ratios were made by replacing the sheath fluid with solvent only in the co-electrospinning setup. A comparison was made of both the large and microscale morphology of the composite nanofibers before and after carbonization with SEM images. As shown in **Figure 4-3a**, when the silicon content is low (e.g., Si/PVA=1:3 or 25wt.%), the composite nanofibers show the typical smooth surface of the electrospun nanofibers. After carbonization, Si nanoparticles are found to align as short, sub-micrometer nanofibers with their fibrous branches held

together by PVA-derived carbon skin (**Figure 4-3b&3c**). The produced carbon/silicon composite nanofiber mats are very flexible because of the thick carbon skin and strong linkages left in the nanofiber network. When more silicon nanoparticles are added in the electrospinning solution (e.g., Si/PVA=2:3 or 40 wt.%), some aggregates begin appearing randomly throughout the electrospun nanofibers, resulting in a rough and uneven surface, though most silicon nanoparticles are still encapsulated in composite nanofibers (**Figure 4-3d**). Silicon domains grow larger in some locations and their fibrous morphology therefore becomes less obvious (**Figure 4-3e&3f**). The diameter of those short silicon fibers increases slightly due to denser nanoparticle aggregates and possible dislocations of neighbor silicon domains during PVA calcination. Such aggregation becomes more serious when the initial silicon/PVA mixing ratio is increased to 1:1 (or 50 wt.%). Many cage-like islands, 1-2 μm in size with silicon nanoparticles stitched together by

composite nanofibers, emerge in the composite nanofiber network (**Figure 4-3g**). More dense silicon domains appear with less fiber-like morphology (**Figure 4-3h&3i**). The free space between silicon branches largely shrinks, though very thin nanofibers connecting different silicon-rich domains can still be seen in some locations.

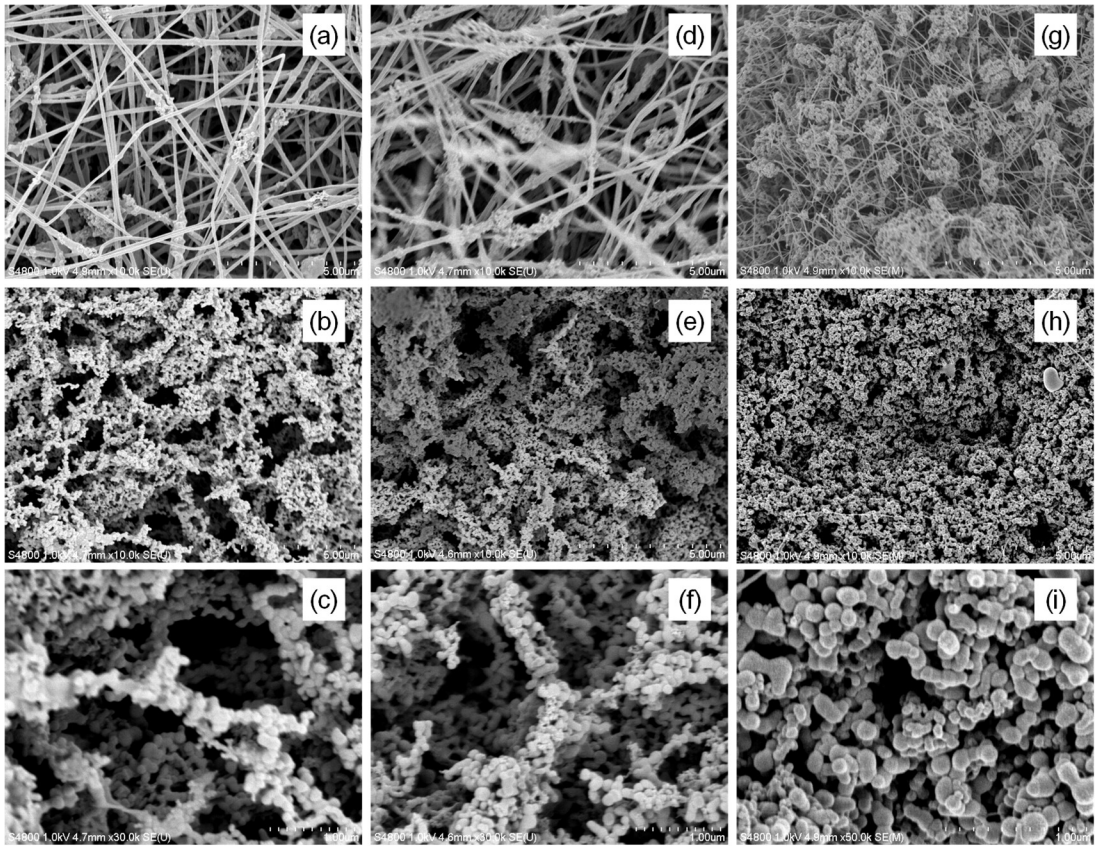

Figure 4-3: SEM images of PVA/Si nanoparticle composite nanofibers with a Si/PVA ratio of (a) 1:3; (c) 2:3; (e) 3:3 and their carbonized counterparts (b), (d), (f), respectively.

4.3.3 EDS Quantitative Analysis

During carbonization, a large percentage of carbon in PVA/silicon nanofibers was lost, which affected the silicon/carbon ratio in composites. EDS analysis (**Figure 4-4a**) shows that, for a sample of PVA/Si composite nanofibers with an original carbon/silicon ratio of 2:1 before carbonization (C: 62 wt.%; Si: 32 wt.%), the ratio changed to 3.3:1 after carbonization (C: 22 wt.%; Si: 72 wt.%). Although carbonization raised the eventual Si content, it in turn reduced the ductility of those nanofibers on many occasions. Unlike the composite nanofibers with a silicon content of 25 wt.% or 40 wt.%, the composite nanofibers with 50 wt.% silicon content had to be handled with great care to avoid

pulverization, though their shape and morphology were reserved on the substrate after carbonization. This similarity to composite anodes made of physically mixed conductive carbon and silicon nanoparticles disqualifies their use as a flexible 3D current collector. After introducing a layer of PAN to wrap up the PVA/silicon nanofiber bundles, the produced composite microfibers become ductile again after carbonization. With nearly 40-60 % of the original carbon molecules retained after cyclization of carbon atoms, this PAN-derived fibrous shell provides mechanical strength to the composite microfiber mat while protecting the thin silicon/carbon nanofibers inside, holding them in position to avoid pulverization. The silicon/carbon ratio of the carbonized PVA/Si/PAN composite fibers was measured by TGA. As shown in **Figure 4-4b**, the TGA curves for all composite fibers have a clear weight loss stage between 250-450 ^{o}C due to the burn out of carbon content. The weight loss percentage matches closely to the polymer content in the original PVA/silicon nanofibers. The PAN microfiber shell that encapsulates PVA/silicon nanofiber bundles makes up for the lost carbon from PVA carbonization in the final silicon/carbon composites. Not only does it retain the needed flexibility and conductivity for anode material of LiBs, but it also contains composite fibers with similarly high silicon content to original polymer suspensions for processing.

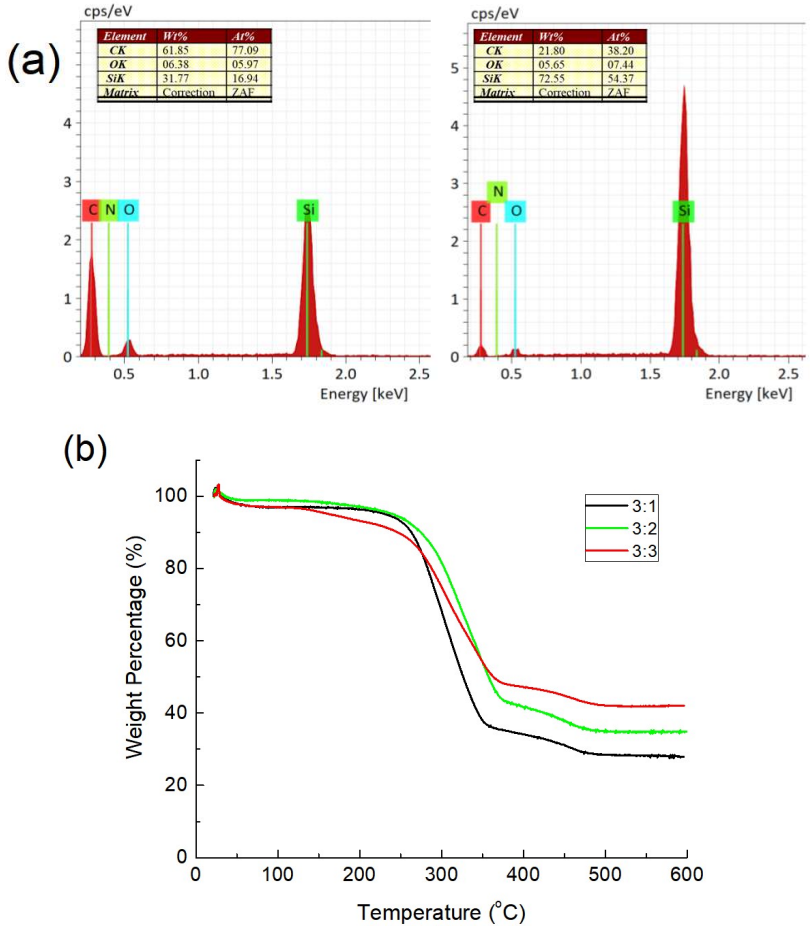

Figure 4-4: EDS quantitative analysis (a) of PVA/Si/PAN fibers before and after carbonization with an original Si/PVA ratio of 1:3. (b) TGA analysis of carbon/silicon fibers with various carbon/silicon ratios.

4.3.4 The XPS Spectrum Analysis

The XPS spectrum of the carbonized PAN encapsulated PVA/Si nanofibers shows clearly the N 1s peak beside the major peaks of carbon, oxygen, and silicon elements when compared to the survey spectrum of the PVA/Si nanofiber sample (**Figure 4-5a**). A contribution of ~4.4% to the total mass in the composite fibers proves the presence of nitrogen. Further deconvolution of the N 1s spectrum in a high-resolution scan reveals the existing pyridinic (398.4 eV) and pyrrolic (400.4 eV) groups, confirming the presence of cyclization of PAN skin on the surface of those composite fibers (**Figure 4-5b**). The Si

2p spectrum displays two main peaks centered at 99.5 eV and 103.6 eV, corresponding to pure Si (S^0) and SiO_2 phase (S^{4+}), respectively, as shown in **Figure 4-5c&5d**. Other subpeaks in between are attributable to non-stoichiometric SiOx bonds. In the PVA/Si composite nanofibers a large percentage of SiO_2 phase (~65%) was found on the surface Si nanoparticles (**Figure 4-5d**), while in PVA/Si/PAN composite fibers, this percentage drops to ~ 50% (**Figure 4-5c**). Two major processes most likely contribute to the SiO_2 shell. The first is the native passive layer on the surface of Si nanoparticles, which is unavoidable given their initial presence in an aqueous solution. Although HF pre-etching prior to mixing with the PVA solution can help strip this native oxide layer, Si nanoparticles will be quickly oxidized due to this extended period in the PVA solution. The processes of drying and stabilizing the formed PVA/Si composite nanofibers in air at elevated temperature which follow may also contribute additional oxidation. This step, however, is necessary before polymer carbonization to help form high-quality carbon fibers. Compared to PVA/Si nanofibers, the extra PAN coating seems to mitigate this second oxidation process during fiber stabilization, leaving less oxidized Si nanoparticles in the composite fibers. With lower lithiation capacity of SiO_2 phase than Si, the PVA/Si/PAN composite anode with less oxidized Si nanoparticles contributes more capacity in LIBs than the PVA/Si counterpart (see next charge/discharge section later for details).

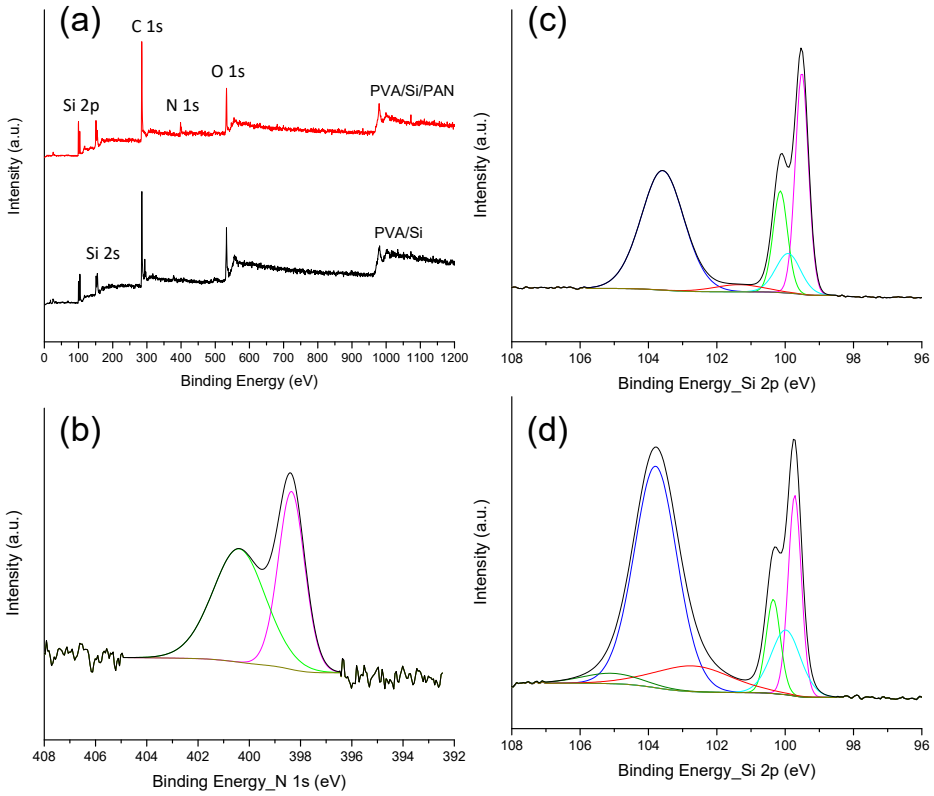

Figure 4-5: XPS analysis of carbon/silicon composite nanofibers (3:3): (a) survey scans of PVA/Si/PAN and PVA/Si composite fibers; (b-d) detailed scans of N 1s (b) and Si 2p (c) of PVA/Si/PAN fibers. Si 2p spectrum of PVA/Si nanofibers.

4.3.5 The Electrochemical Performance

The electrochemical performance of these nanofiber-in-microfiber composite anodes was tested via galvanostatic charge/discharge experiments. **Figure 4-6** shows the voltage profiles (plot of potential against specific capacity) at the end of 1st, 2nd, 10th, 50th, and 100th galvanostatic charge/discharge cycles of carbon/silicon composite nanofibers with initial silicon/carbon ratios from 1:3 (25 wt.%) to 1:1 (50 wt.%). For the first cycle, the charge and discharge capacity of the PVA/Si/PAN composite fibers with 50 wt.% Si reached 3406 mAh g^{-1} and 2401 mAh g^{-1}, respectively. By comparison, composite fiber anodes with 40 wt.% Si show 2458 mAh g^{-1} (charge) and 1749 mAh g^{-1} (discharge), while those with 25 wt.% Si had the lowest capacity at only 2048 mAh g^{-1}

(charge) and 1463 mAh g^{-1} (discharge). The indicated capacities were calculated based on the total mass of anode material (i.e., including both carbon and Si). It is not surprising that the composite fibrous anodes with higher Si content have larger initial storage capacity of Li ions. In the first cycle, the discharge capacity of these Si-rich composite anodes was close to the theoretical value while their charge capacity was even higher. Such phenomena are commonly seen during initial battery tests and are believed to be the result of consumption of Li ions during the SEI formation. The small plateau around 0.75 V on the first charging curve of all three anodes indicates the decomposition of the electrolyte solution and the formation of the solid electrolyte interphase (SEI) over the electrode surface for the first time. For the same reason, low coulombic efficiency is found for all three anode types in the first few cycles, with resulting coulombic efficiencies (i.e., discharge capacity/charge capacity) of 70.5% (50 wt.% Si anode), 71.1% (40 wt.% Si anode), and 71.4% (25 wt.% Si anode).

Starting from the second cycle, a second type of plateau appears on the charge and discharge curves of these Si-rich anodes at voltages of ~ 0.25 V (charge) and ~0.50 V (discharge) respectively. This plateau can be attributed to the phase transformations between different Si-Li states during the lithiation and delithiation processes. After the establishment of a stable SEI, the coulombic efficiency quickly recovered to nearly 100% and remained high afterwards (**Figure 4-6d**). Like other carbon- or silicon-based anodes, a gradual shrinking of this plateau and capacity loss were also found here for all three types of Si-rich composite anodes during cycling. The composite fibrous anodes with 25 wt.% and 40 wt.% Si show similar plateau shrinkage and capacity decay dynamics, despite their different specific capacity values (**Figure 4-6a&6b**). For example, after the

10th cycle, the discharge capacity of composite fibrous anodes fell ~12% for both composite anodes (1524 mAh g^{-1} for anodes with 40 wt.% Si and 1289 mAh g^{-1} for anodes with 25 wt% Si). After 50 cycles, this value became 1132 mAh g^{-1} (anodes with 40 wt% Si) and 940 mAh g^{-1} (anodes with 25 wt.% Si), respectively. The composite fibrous anode with 50 wt.% Si had the fastest shrinking of the voltage plateau and largest loss percentage of the specific capacity. As shown in **Figure 4-6c**, its discharge capacity declined to 1674 mAh g^{-1}, or 70% of its initial capacity after only 10 cycles. After 50 cycles, this value dropped to 1198 mAh g^{-1}, or 50% of its initial capacity.

Such capacity loss dynamics are better depicted by the cycling plots of LIBs. As shown in **Figure 4-6d**, the specific capacity loss for the anodes with 50 wt.% Si content shows a steep slope, differing from the curves shown by the other two types of anodes. Its specific capacity value dropped below that of the anodes with 40 wt.% Si after just 75 cycles, and even below the anodes with 25 wt.% Si after only 125 cycles. The other two anode types showed a similar rate of decay of their specific capacities. After 10 cycles, the retention ratio of the specific capacity was 87% (for anodes with 40 wt.% Si) and 88% (for anodes with 25 wt.% Si) of each of the anodes' respective initial values. After 50 cycles, the retention capacity dropped to 65% (for anodes with 40 wt.% Si) and 64% (for anodes with 25 wt.% Si). The decay rate of the specific capacity for these two types of composite fibrous anodes was sustained with only minor variations. This indicates that the two anodes experienced similar lithiation and/or delithiation during all testing cycles. Such similar cycling performance (barring the actual initial capacity value) is to be expected, given the similar morphology of those composite fibrous anodes: connected branch structures comprised of short Si nanofibers are seen in both composites (**Figure 4-**

3e&3b), while the anode with 50 wt.% Si shows many large Si islands instead (**Figure 4-3h**). Long-term cycling stability was also examined on the composite fibrous anodes with 40 wt.% Si. As shown in **Figure 4-6d**, for over 250 cycles, their specific capacity retains ~900 mAh g^{-1} with only 10% additional loss (from cycle 50 to cycle 250).

Relatively slow decay of the specific capacity was observed for all three composite fibrous anodes during cycling rate tests (**Figure 4-6e**), but the situation was different among anodes with different silicon contents. The anodes with relatively low silicon content (e.g., 25 wt%) largely sustained the charge/discharge capacity with only minor variations. Among the anodes with higher silicon content, the difference was more severe for those with 50 wt% Si than the ones of 40 wt% Si. The specific charge/discharge capacity could be largely recovered after the current rate was sequentially increased from 0.1C to 0.5C, 1C, and 2C, then reduced back to 0.1C. It seems that a consistent cycling performance was easier to achieve with a charge and discharge capacity of ~1000 mAh g^{-1} or lower, given that the silicon nanoparticles and the produced composite nanofibers are well dispersed without obvious aggregates (such as in the anodes with 25 wt.% Si). This indicates that the key factor for stable lithiation or delithiation comes from those active materials with appropriate dimensions in nanometer scale. Large domains will lead to electrode pulverization issues, loss of reversible capacity, and cycling instability. Unlike the largely matched charge/discharge capacity order observed at small current rates (0.1C and 0.5C), elevated current rates (1C and 2C) caused scrambled capacity order, with anodes of 50 wt.% Si carrying similar or slightly lower capacity than those having 40 wt.% Si (**Figure 4-6e**). The presence of extra carbon skin on the composite nanofiber bundles derived from the PAN coating indeed helps

retain more lithiation capacity. Compared to the anode made only of PVA/Si nanofibers with 25 wt% Si, those encapsulated in PAN microfibers achieve higher specific capacity at various charge rates (a capacity difference of ~330 mAh g^{-1} for 0.1C, ~300 mAh g^{-1} for 0.5C, ~200 mAh g^{-1} for 1C, and ~80 mAh g^{-1} for 2C), as shown in **Figure 4-6e**.

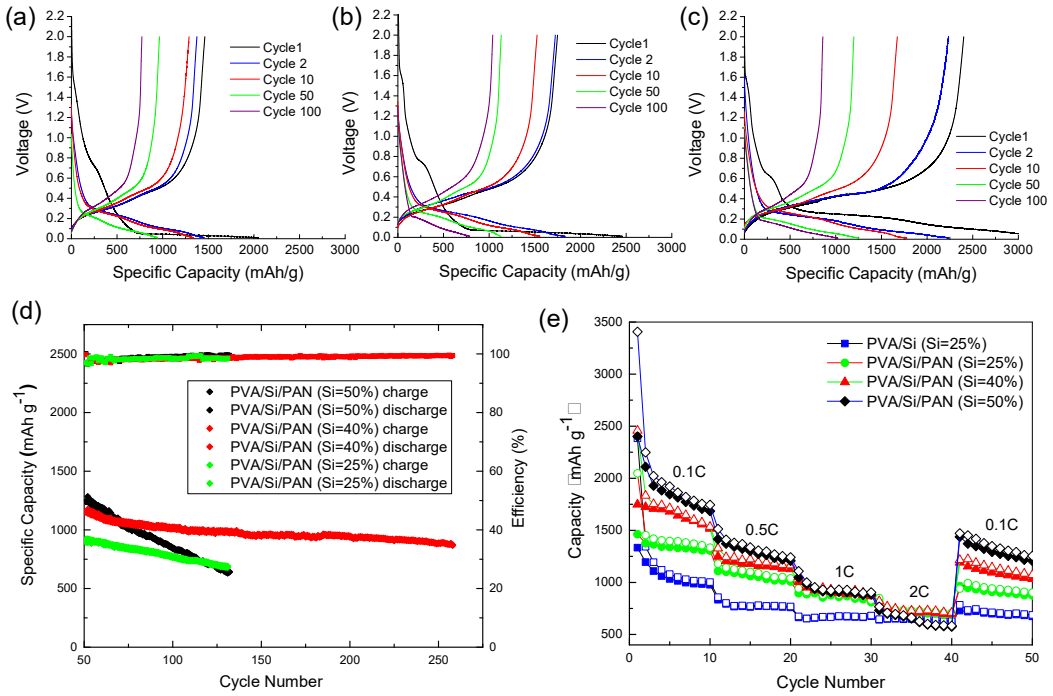

Figure 4-6: (a-c) The voltage profiles for the 1st, 2nd, 10th, 50th, and 100th galvanostatic charge/discharge cycles of nanofibers-in-microfibers composite anodes with a Si ratios of 25% (a), 40% (b), and 50% (c). Different charging rates (d) and cycling performances and coulombic efficiency (e) of those PVA/Si/PAN fibers of various Si contents.

Our new method enables the production of fibrous composites with better, silicon-rich anodes in competition against those made of a physical mixture of conductive carbon and silicon nanoparticles. It carries high silicon content that approaches maximal processing allowance for original polymer/silicon suspensions while maintaining porous nanofibers for higher capacity without electrode pulverization. Besides the needed electrical conductivity, the fibrous morphology within the composite fiber mats serves as

a flexible 3D current collector. In this unique nanofiber-in-microfiber configuration, the branched, short silicon nanofibers with thin carbon skin and the mesopores they create appropriately manage the volume expansion and stress induced when lithium alloys with silicon. The outer PAN shell around the PVA/silicon nanofiber bundles provides extra carbon coating to protect the silicon from further oxidation during fiber processing. It also creates a confined microenvironment around the silicon/carbon nanofibers to limit the permeability and contact of electrolytes to silicon during cycling. This helps mitigate the fading of capacity, which is believed to be attributed to mixed effects on the progressive increase of the SEI thickness and loss of electron conduction pathways that lead to dead silicon formation. Although significantly lessened in composites with relatively high silicon content (e.g., 40 wt.%), heterogeneous pulverization could not be completely avoided in anodes with ultrahigh silicon content (i.e., 50 wt.% or higher) for the same reasons mentioned earlier about capacity fading, particularly when more of the micrometer size silicon domains present lose the unique configuration (i.e., short Si nanofiber bundles wrapped in long carbon microfibers), making the composite similar to those carbon/silicon blended anodes. Nonetheless, both higher Li ion storage capacity and better cyclic stability are achieved when this unique composite fiber configuration is held with a silicon content of 40 wt.% or less.

4.4 Conclusions

A new nanofiber-in-microfiber, silicon-rich composite anode was prepared through a coaxial electrospinning, in which PVA/silicon suspension flows in the middle and a PAN/DMF solution serves as the sheath stream. The produced 3D fibrous anodes with high silicon content help leverage the capacity performance of current LIBs towards

commercial transport cell requirements. The high-quality, nonwoven carbon microfibers derived from the PAN outer shell provide structural protection for the short, silicon-rich nanofibers inside and prevent further oxidation of silicon during fiber processing. Together with the thin carbon skin over silicon/carbon nanofiber bundles inside, the microfiber mats form an electrically conductive network to serve as the 3D current collector to promote Li ion transport and charge transfer during charge/discharge processes. Simultaneously, short silicon nanofibers and the mesoporous buffering spaces among them help effectively mitigate the induced stress in silicon nanoparticles initialized by the volume change during Li insertion and extraction. All these features of this nanofiber-in-microfiber composite anode together effectively balance issues between electrode pulverization and high reversible capacity, leading to promising electrochemical performance and capacity retention for silicon-rich anodes to move forward with commercialization. The unique processing strategy for these hybrid fibrous composites with high solid content offers a new scalable route to manufacture composite nanomaterials and promises broad applications beyond LIBs.

CHAPTER 5

UPCYCLING DRINK BOTTLE WASTE TO BALL-SHEET INTERCALATED CARBON STRUCTURES FOR SUPERCAPACITOR APPLICATIONS

5.1 Introduction

Our heavy dependence on and excessive consumption of fossil fuels has led to global challenges of environmental pollution and climate change. It urges our mission in the search for alternative clean energy resources like wind, ocean, and solar power on a much larger scale in the near future (Bose *et al*., 2010). Efficient, effective, and economical storage of the generated clean energy is crucial to sustainable deployment, as many of them have varying characteristics (Deng *et al*., 2014). The supercapacitor is a favored energy storage system for its fast charge/discharge rates, high power density, and long cycle life (Wang, 2018; Liu *et al*., 2020; Mehtab *et al*., 2019; Huang *et al*., 2014). Studies have shown that the electrode material itself and its architecture features such as large surface area, rich active sites, and good electrochemical conductivity are critical to achieve superior electrochemical performance for supercapacitors. Among different supercapacitor materials, carbon materials of various formats dominate due to their excellent conductivity, rich active sites, and strong chemical stability (Salanne *et al*., 2016; Zhi *et al*., 2013; Zhang *et al*., 2009; Pandolfo *et al*., 2006). Three-dimensional porous activated carbon materials that are prepared from physical or chemical activation

processes of various types of carbonaceous sources including wood, coal, and biomass (e.g., plant and animal debris) carry huge specific surface area (e.g., ~3000m^2/g) and numerous hosting sites, but unfortunately only moderate conductivity (Marichi *et al*., 2018; Du *et al*., 2019; Xia *et al*., 2019). One-dimensional (e.g., carbon fibers) or two-dimensional (e.g., graphene) carbon materials generally have high electrical conductivity in a connected network, but relatively limited surface area and high cost/ low manufacturing capacity. Zero-dimensional carbon sources such as carbon nanoparticles (Zhang *et al*., 2009) can provide flexible specific surface area attributed to their tunable size, size distribution, and shape (Genc *et al*., 2017). However, their discrete nature requires assistance of conductive non-active additives or other carbon structures to have a working electrode. Coupling different carbon materials seems to be the strongest solution due to the potential inheritance of traits from each individual carbon format to achieve superior storage capacity, high conductivity, and cycling stability. Many reported methods involve multiple steps to prepare electrodes of those sophisticated carbon structures. For example, in a 0- and 2-dimensional carbon material combination, the 0- and 2-dimensional carbon material are synthesized separately. This is followed by delaminating the 2D carbon sheets mechanically (e.g., sonication) and/or chemically (e.g., adding surfactant), dispersing 0D carbon materials on the surface of a 2D carbon nanosheet, and re-stacking them into a ball-sheet architecture, in which 0D carbon is intercalated in the gaps of 2D carbon nanosheets. Unfortunately, the manufacturing of 0- and 2-dimensional carbon material combinations face great challenges in the aggregation of 0D and 2D carbon materials because of their large surface energy and strong

interactions. As a result, the actual integration status often varies largely from the ideal, leading to diversified electrochemical performance of the finished electrodes.

Herein we investigate a one-step synthesis of zero-dimensional carbon quantum dots that are grafted to the surface of thin 2D carbon sheets and intercalated between those layers to form a connected conductive network as supercapacitor electrodes. To retain the sustainable nature of our technology, we adopted plastic waste such as the discarded drinking bottles that are made of polyethylene terephthalate (PET) as our carbon source during the hydrothermal synthesis of this ball-sheet carbon structure (designated as "PBSC" in later discussions). Within a single step, we successfully produced thin 2D carbon sheets on which carbon quantum dots (CQDs) of 1-2 nm are well dispersed. After drying and activation, the received carbon colloids with their unique ball-sheet carbon architecture are coated on the surface of a nickel foam substrate for electrochemical testing. Their supercapacitor performance is then investigated by cyclic voltammetry (CV), galvanostatic charge-discharge (GCD) and electrochemical impedance spectroscopy (EIS) measurement. In this method, CQDs provide the necessary conductivity with their graphitic core, large surface area, and active sites to host ions for their rich surface defects/ligands. The 2D carbon sheets avoid large aggregations of CQDs and build up a connected, conductive carbon network necessary for a working electrode of supercapacitors. As the formation of the 0D CQDs and 2D carbon sheets occurs simultaneously in the same synthesis solution, the surface energy of individual carbon objects (both CQDs and carbon sheets) is greatly suppressed by their surrounding environment so that CQDs are naturally confined between the new formed 2D carbon sheets and retain their even dispersion status after drying. In this way, the challenges of

dispersion and intercalation seen in other 0D carbon in 2D structure are wisely avoided. Aside from its advantages of easy manufacturing and effective architecture for electrical energy storage, the upcycling of plastic waste into clean energy materials may also promote clean energy and environmental sustainability. As the No. 1 plastic product and waste (accounting for about 8% of all plastic products (Barriocanal *et al*., 2005)), we expect our efforts towards new utilization of the PET drinking bottle waste will promote the collection and recycling of plastic waste with economic intensives and help move towards the closed-loop life cycle of plastics.

5.2 Experimental

5.2.1 Materials and Reagents

Pure polyethylene terephthalate (PET) was purchased from Sigma-Aldrich. Samples of commercial PET were cut from drinking water bottles. Nitric acid (70%) and ethanol were purchased from Fisher Scientific. Ethylene glycol and isopropyl alcohol (99%)(IPA) were purchased from Sigma Aldrich. All chemicals and reagents were used as received without further purification.

5.2.2 Ball-sheet PET Carbon Structure Synthesis

A new drinking water bottle was cut into pieces. Each PET sample of 0.5g was loaded in a 50-mL PPL-lined autoclave, in which 10 mL of DI water, 2 mL of nitric acid (71%), and 2 mL ethanol (99%) were added. The hydrothermal synthesis was carried out at 200℃ for 8 hrs. The received black solution was first washed using DI water, followed by centrifugation at 3,500 rpm for multiple times until pH ≥ 6. The carbon samples were then dried in a vacuum oven overnight at 70℃ and the resulting solid sample was designated as $PBSC_{C2H5OH}$ (PET Ball-Sheet Carbon with C_2H_5OH). Two other ball-sheet

carbon samples were also made for comparison purposes: one was prepared by replacing ethanol with ethylene glycol and the other involved isopropyl alcohol during the hydrothermal synthesis (designated as $PBSC_{HOC2H4OH}$ and $PBSC_{IPA}$, respectively).

5.2.3 Material Characterization

The size and structure of PBSCs were characterized by scanning electron microscopy (SEM, Hitachi S-4800), transmission electron microscopy (TEM, JEOL 1400, JEOL), and high-resolution TEM (HRTEM, Hitachi H-9500, Hitachi). Fourier transform infrared spectra (FT-IR) of dried PBSCs were recorded to identify the functional groups on the surface (Thermo Scientific SMART FT-IR spectrometer). X-ray photoelectron spectroscopy (Scienta Omicron XPS) analysis was done to reveal the chemical state of the as-synthesized PBSCs. The X-ray photoelectron spectroscopy (XPS) analysis was done on a Scienta Omicron instrument with the following operation conditions: 10 sweeps for the survey scans and 200 sweeps for each of C 1s, O 1s, and N 1s detailed scans. The pass energy was set to 40 eV with a step size of 0.2 eV and a dwell time of 200 milliseconds for all samples. The optical properties of PBSCs were measured using photoluminescence spectroscopy (ISS, K2 Multifrequency Phase Fluorometer).

5.2.4 Preparation of PBSC Electrode Sheet

The $PBSC_{PET/C2H5OH}$ samples were first mixed with 6M KOH (mass ratio: 1:6) and calcined in nitrogen gas at 550℃ for 2h for surface activation. The activated $PBSC_{C2H5OH}$ were then washed using DI water and centrifugation until pH ≥ 6. After discarding the supernatant, samples were dried under vacuum at 70℃ overnight.

The resultant solid ((~0.5g) was mixed with polyvinylidene fluoride (PVDF) and super P carbon black at a mass ratio of 80 ： 10 ： 10 in N-methylpyrrolidone (NMP).

The paste was then blade-coated onto a foamed nickel sheet with an area of ~1 cm^2 (this gives a load mass about 5 mg). After drying at 80 ℃ for 12 h, the prepared electrode was placed in an electrochemical cell that was filled with a solution of 6M KOH electrolytes. A three-electrode system was adopted with platinum rod and calomel electrodes as the counter electrode and reference electrode respectively.

5.2.5 Electrochemical Performance Tests

CHI 760e was used for most electrochemical tests, which were done at room temperature with the voltage window set between - 1.1-0 V. After the galvanostatic charge/discharge test, the specific capacitance was calculated according to **Eq. 5-1**:

$$C_g = \frac{I\Delta t}{m\Delta V} \qquad \textbf{Eq. 5-1}$$

where C_g is the specific capacitance of electrode mass (F/g); I is the current (A); Δt is the discharge time (s); ΔV is the voltage (V); and m is the mass of the active material in the working electrode (g).

Electrochemical impedance spectroscopy (EIS) measurements were conducted on Autolab PGSTAT302N electrochemical workstation (Metrohm, Switzerland). The ac perturbation signal was set at 10 mV with a frequency range of 10^{-2}-10^5Hz. The test solution was 5 mmol/L $K_3Fe(CN)_6/K_4Fe(CN)_6$ (1:1) solution containing 0.1mol/L KCl.

5.3 Results and discussion

5.3.1 Morphology and Surface Characterization

The morphology of the $PBSC_s$ was characterized by SEM and TEM. The SEM image shows a flake-like morphology of the carbon samples after the hydrothermal treatment of PET drinking bottle waste (**Figure 5-1a**). The TEM image revealed many tiny CQDs dispersed on those thin carbon flakes (**Figure 5-1b**). Further analysis finds

that the size of these CQDs vary from 0.8 to 2.0 nm with an average diameter of 1.4 nm (**Figure 5-1c**). The high-resolution TEM (HR-TEM) image shows that those CQDs have clear crystalline lattice fringes that spread over the whole particles (**Figure 5-1d**). The lattice spacing was found to be ~0.21 nm, attributed to the (100) in-plane lattice of graphene, suggesting that those particles are assembled individual CQDs, not PET debris of incomplete transformation.

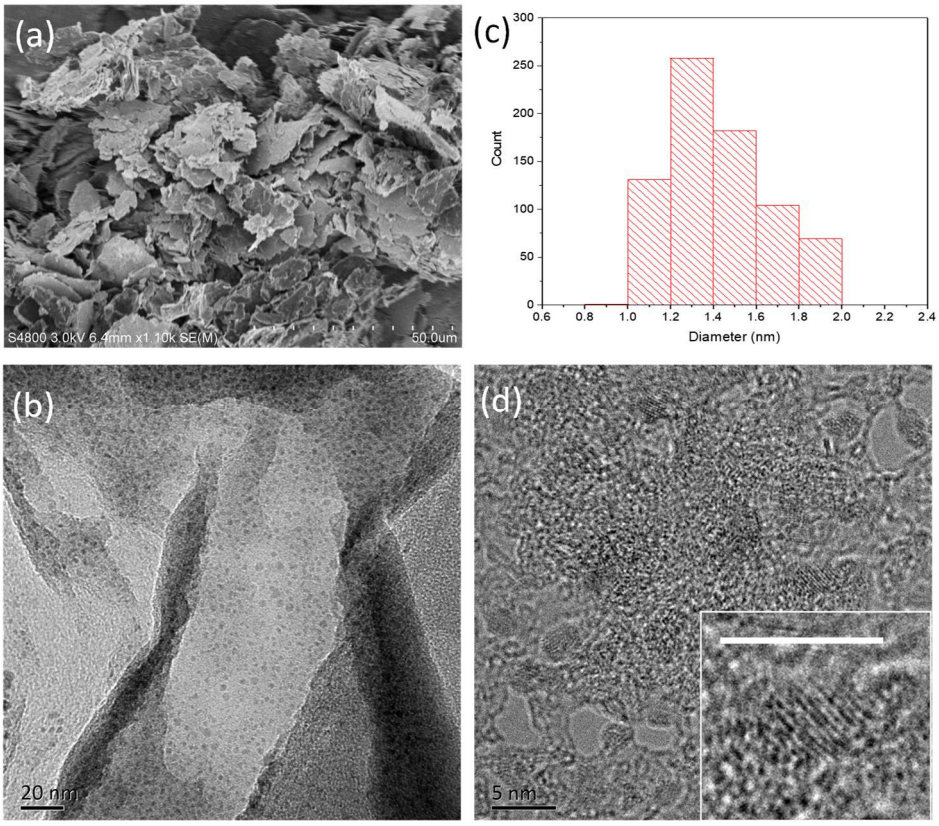

Figure 5-1: SEM (a), TEM (b), and HR TEM (d) images of $PBSC_{C2H5OH}$. Panel c shows the histogram of particle size measurement of those PET PBSCs. The inset of panel (d) is a high-magnitude image of $PBSC_{C2H5OH}$ in the HR TEM image.

XPS spectra clearly display that carbon, oxygen, and nitrogen are the three major elements of these PBSCs derived from PET waste, as shown in **Figure 5-2a**. Similar atomic compositions were found in both samples, while $PBSC_{C2H5OH}$ has slightly higher

nitrogen dopant than $PBSC_{HOC2H4OH}$ (N 1s: 6.1 at% for $PBSC_{C2H5OH}$; 4.3 at% for $PBSC_{HOC2H4OH}$). To reveal the chemical states of these three elements, further detailed XPS scans of C 1s, O 1s, and N 1s were conducted. In both PBSC samples, three major deconvoluted peaks (located at ~284eV, ~285eV, and ~28 eV) were found in the C 1s spectra (**Figure 5-2b**), which are each associated with C=C/C-C, C-O/C-N, and C=O groups, respectively. While the two PBSC samples have similar numbers of C=O bonds, fewer C=C/C-C bonds or benzene ring structures were found in the $PBSC_{C2H5OH}$ samples. A larger deconvoluted peak at 285 eV, which represents the C-N or C-O bonds, is found in the C 1s spectrum of the same PBSC sample. This might be due in part to the higher nitrogen doping in the framework of CQDs and the formation of more C-N bonds in the carbon rings. The spectrum of the $PBSC_{C2H5OH}$ sample shows a higher portion of C-O bond peak (532.6 eV) than the $PBSC_{HOC2H4OH}$ sample (**Figure 5-2c**). Considering the similar levels of C=O groups (or possible ester groups in the carbon chains) in both samples, the larger portion of C 1s peak at 285 eV for $PBSC_{C2H5OH}$ is likely a mixed contribution of more C-N and C-OH bonds. To further identify the format of nitrogen in those PBSCs, high-resolution spectra of N 1s (**Figure 5-2d**) were collected. Three deconvoluted peaks identified at 398.5 eV, 399.5 eV, and 400.5 eV were found. This indicates that nitrogen atoms were doped in those PBSCs as pyridinic, pyridone, and pyrrolic nitrogen structures. No oxidized nitrogen bonds such as oxidized pyridine nitrogen (near 402-405 eV) or $-NO_2$ groups (near 405 eV) were found in those PBSC samples. These observations are consistent with the increased C-N peak (near 285.0 eV) in the C1s spectrum. Pyrrolic nitrogen bonds dominate among the C-N bonds in the $PBSC_{C2H5OH}$ sample, while pyridine nitrogen bonds dominate in the $PBSC_{HOC2H4OH}$

sample. These findings also match with the larger number of C=C/C-C bonds in the C 1s peak of the $PBSC_{HOC2H4OH}$ sample and larger portion of C-N/C-O bonds in the C 1s peak of the $PBSC_{C2H5OH}$ sample. The XPS results clearly indicate that PBSCs with nitrogen dopant were successfully synthesized from PET plastic waste and their surfaces were functionalized with C-OH, COOH, C-NH, and O=C-NH< groups.

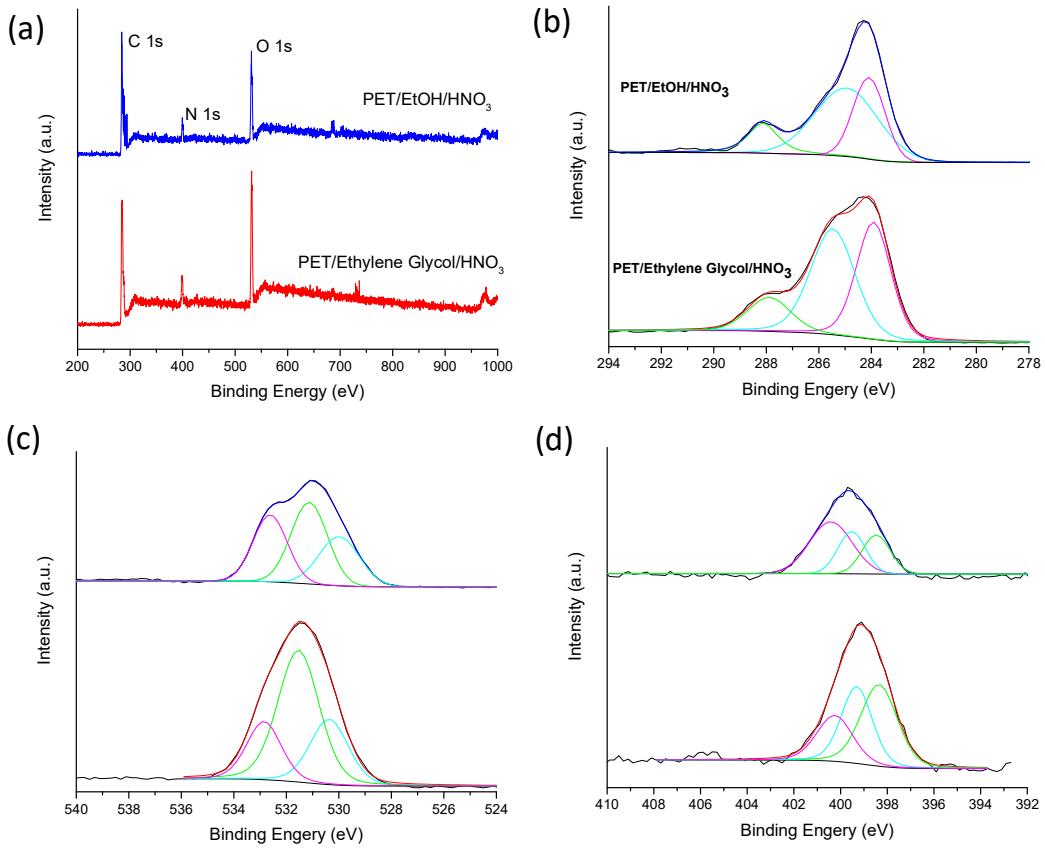

Figure 5-2: XPS spectra of PBSCs derived from PET involving ethanol and ethylene glycol: (a) survey scan, (b-d) detailed scans of C 1s (b), O 1s (c), and N 1s (d).

FTIR was also used to examine the function groups of these synthesized PBSCs. The spectra of $PBSC_{C2H5OH}$ derived from both pure PET and PET drinking bottles (with additives) were measured and compared, as shown in **Figure 5-3a**. The FTIR spectra of both PBSC samples exhibit similar patterns. Typical broad stretching vibration

absorption peaks of -OH are shown between 3000-3750 cm^{-1}, suggesting the existence of a large number of such groups. There is a corresponding strong absorption peak for the in-plane bending vibration of phenolic OH near 1400 cm^{-1}. This indicates that the -OH group in those PBSC samples appear as both phenolic and carboxyl structures and imply the existence of many benzene rings. The peaks at 1075 and 1120 cm^{-1} can be attributed to the stretching vibration of C=O lactone, suggesting that some ester bonds may be retained in PBSCs after the hydrothermal reactions. Another C=O stretching vibration peak (originated near 1722 cm^{-1}) was shifted to 1711 cm^{-1} due to the π-π interactions and pyrrole rings in the hydrocarbon structure, further confirming the formation of benzene structures in $PBSC_{C2H5OH}$. The peak near 1605-1621 cm^{-1}, caused by the C=C stretching vibrations, and the peak near 740 cm^{-1}, attributed to the out of plane bending vibration of hydrogen from the disubstituted benzene rings, both support our claim of substituted benzene rings. The remaining small peaks located between 750 ~ 1000 cm^{-1} are attributed to other out of plane CH bending vibrations on the carbon skeletons of the PBSCs, particularly the one located near 730 cm^{-1} for CH from benzene rings. A C-N stretching vibration at 1285 cm^{-1} and broad peak centered at 3400 cm^{-1} are both very clear examples of nitrogen bonds, specifically -NH groups, in received PBSCs. When comparing the aforementioned PBSCs to those derived by adding ethylene glycol instead (i.e., $PBSC_{HOC2H4OH}$), both possess a strong peak of the -NH group at 3400 cm^{-1} (**Figure 5-3b**), but the C-N stretching vibration at 1285 cm^{-1} is much stronger in the $PBSC_{C2H5OH}$ than $PBSC_{HOC2H4OH}$. As for the functional groups associated with benzene rings, some are stronger in $PBSC_{C2H5OH}$ (e.g., C=O at 1711 cm^{-1} and Ar-CH at 740 cm^{-1}), some are weaker (e.g., C=C at 1621 cm^{-1}), and others are similar (e.g., Ar-OH at 1400 cm^{-1}).

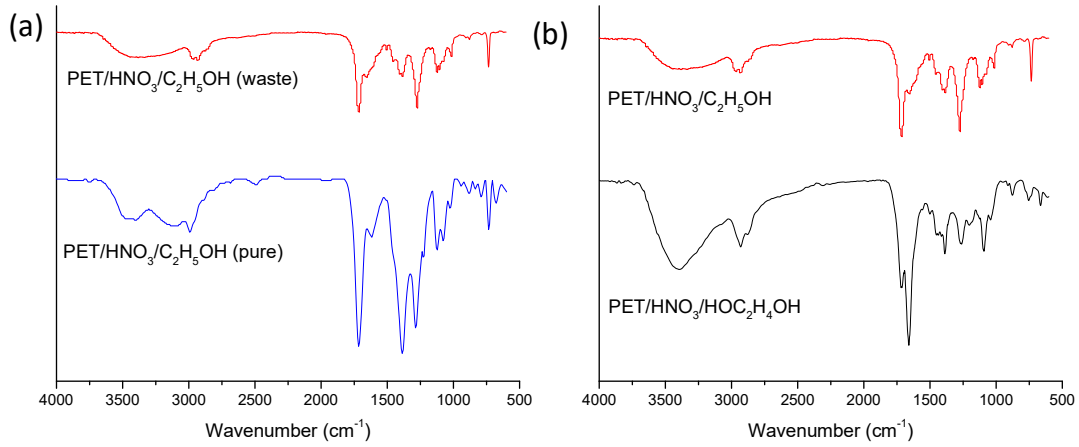

Figure 5-3: FT-IR spectra of PET PBSCs made of pure PET and PET drinking bottle waste (a) and the second precursor of ethanol or ethylene glycol (b).

5.3.2 Photoluminescence of PBSCs

The photoluminescence of the as-prepared PBSCs was measured next. Under the optimal concentration, a strong luminescence signal with an emission peak centered near 425 nm was found after being excited by a UV laser light of 300 nm (**Figure 5-4a**). The emitted fluorescence signal of these PBSCs was continuously enhanced when applying an excited light with a longer wavelength until it reached 340 nm. When illuminated under an even longer wavelength (from 360 nm to 440 nm), the PBSCs exhibited fading intensity of their fluorescence emission (**Figure 5-4a**). This was accompanied by a slow but clear redshift of the peak center. The photoluminescence signal of $PBSC_{HOC2H4OH}$ showed a change in trend similar to that seen in $PBSC_{C2H5OH}$, as shown in **Figure 5-4b**: the emission is visibly enhanced until reaching a maximum under an excited light of 360 nm, followed by signal decline afterwards. The centers of the emission peak also shift to the long side of the wavelength for the $PBSC_{HOC2H4OH}$ sample. Overall, the quantum yield of these two types of PBSCs are similar (**Figure 5-4c**).

The effect of increasing temperature during hydrothermal synthesis on the quality of the produced PET $PBSC_{C2H5OH}$ from 160ºC to 220ºC under the same acidity was also examined. As shown in **Figure 5-4d**, the photoluminescence signals of $PBSC_{C2H5OH}$ products were significantly enhanced when elevating the temperature of the hydrothermal synthesis, even as it approached the maximum allowance of autoclaves (i.e., 240ºC). Like in other hydrothermal reactions, the rise of the reaction temperature led to a quick buildup of the pressure in the autoclave. Considering the balance of energy consumption cost, safety, and quantum efficiency, we chose to use PBSCs made at 200ºC in most of our experiments and did not explore higher synthesis temperature. However, we do believe there should be an optimal temperature for this hydrothermal synthesis. According to the common carbonization theories, higher temperature promotes the necessary dehydrogenation, condensation, and rearrangement of the hydrocarbon reactants to form an aromatic structure during the hydrothermal reactions; however, too high a temperature could accelerate those reactions to the point that significant agglomeration may occur among the formed polyaromatic clusters. Severe aggregation will lead to a size growth beyond the critical quantum photoluminescent dimensions (i.e., several nanometers). As a result, photons will be trapped in carbon nanoparticles and quickly fade away, leading to the previously mentioned decline in photoluminescence intensity.

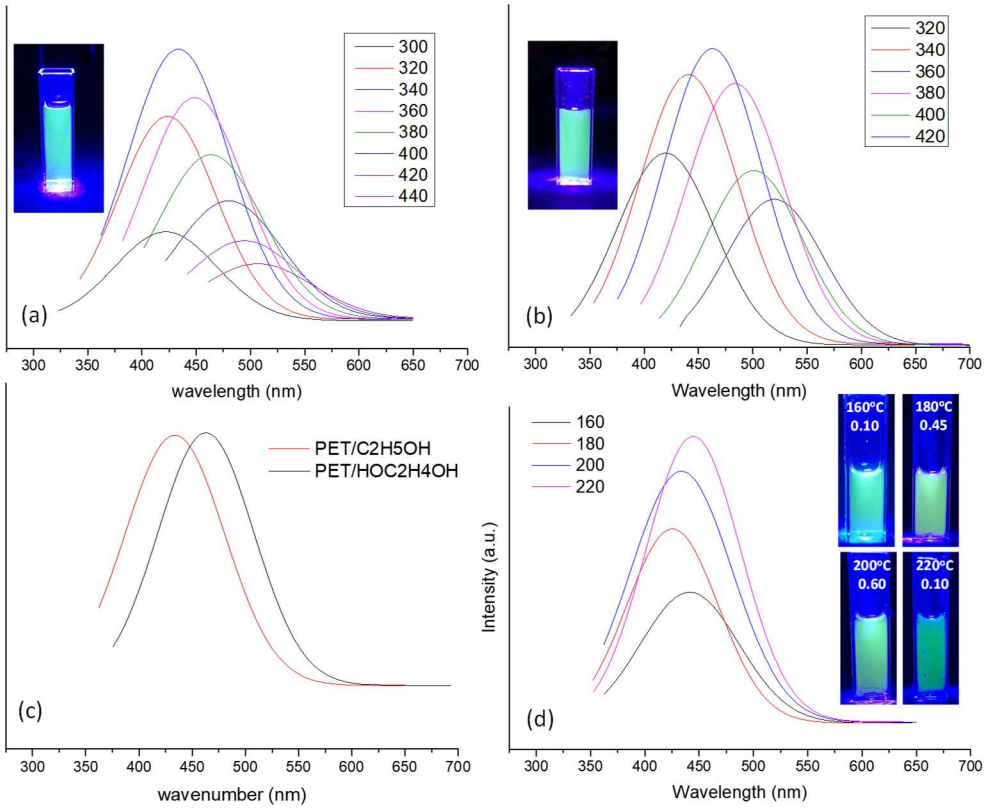

Figure 5-4: The steady-state emission spectra of $PBSC_{C2H5OH}$ (a) and $PBSC_{HOC2H4OH}$ (b) under laser of different excitation wavelengths. The photoluminescence signal comparison of two types of PBSCs at maximum luminescence (c) and the luminescence dependence of the as-prepared $PBSC_{C2H5OH}$ samples with various synthesis temperatures (d).

5.3.3 Supercapacitor Performance of PBSC Electrodes

The electrochemical capacitance of electrodes made from PBSCs was evaluated in a three-electrode cell with platinum rod and calomel electrodes as the counter electrode and reference electrode respectively. The tests were done in a 6M KOH electrolyte solution at room temperature with a voltage window set between -1.1-0 V. As shown in **Figure 5-5a**, the galvanostatic charge-discharge (GCD) curves of those PBSC electrodes exhibit some derivations from the ideal triangular shape, but very little iR drop. This indicates a strong pseudo capacitance for PBSC electrodes. At a charge rate of 1 A/g, the $PBSC_{C2H5OH}$ whose synthesis involved ethanol showed much higher specific capacitance

(239 F/g) than that involving ethylene glycol (150 F/g) or isopropanol (75 F/g). By increasing the scan rate, a capacitance drop was observed in the PBSC electrodes just like in many other supercapacitor electrodes. Under a current density of 2 A/g, the specific capacity of the $PBSC_{C2H5OH}$ electrode descended to 198 F/g, but remained the highest among all three electrodes (at 2 A/g, $PBSC_{HOC2H4OH}$ fell to 99 F/g, and $PBSC_{IPA}$ to 30 F/g). When examined in a broader charge rate range (from 1 A/g to 50 A/g), the capacity of the $PBSC_{C2H5OH}$ electrode decreased slowly to 198 F/g (2 A/g), 168 F/g (5 A/g), 147 F/g (10 A/g), 129 F/g (20 A/g), and 96 F/g (50 A/g), as shown in **Figure 5-5b** (Note: the corresponding current densities are given in the brackets). $PBSC_{C2H5OH}$ electrodes synthesized at different hydrothermal temperatures were further compared on their electrochemical performance to decide the optimal synthesis conditions. As seen in **Figure 5-5c**, the $PBSC_{C2H5OH}$ synthesized at 200ºC shows the largest specific capacitance, though the differences in capacity between the three samples are not large. As plastic waste usually carries 10% or less additives other than the polymer itself in their manufacturing recipe, we further compared the performance of the $PBSC_{C2H5OH}$ electrodes made from both pure PET and PET drinking water bottle waste. The galvanostatic charge/discharge curves of $PBSC_{C2H5OH}$ from different purities display a similar shape and achieve similar specific capacitance (**Figure 5-5d**). This suggests that the real PET drinking bottle waste could be directly used to make supercapacitors with reliable electrochemical performance. Extra purification step might not be necessary. To further evaluate the potential practical use of $PBSC_{C2H5OH}$ electrodes made of plastic waste in supercapacitors, their long-term cycling stability was further tested. As shown in **Figure 5-5e**, after 12,000 cycles, approximately 98% of its initial specific capacitance

was retained at the charge rate of 2 A/g. To mimic their application under real conditions, three units of such electrodes were assembled and connected in series to power a red-light LED (2.4 V), as shown in **Figure 5-5f**. After charging, the red LED was powered for nearly 5 min before the luminescence decay was noticed. These observations demonstrate the excellent behaviors of the $PBSC_{C2H5OH}$ electrode as a supercapacitor electrode.

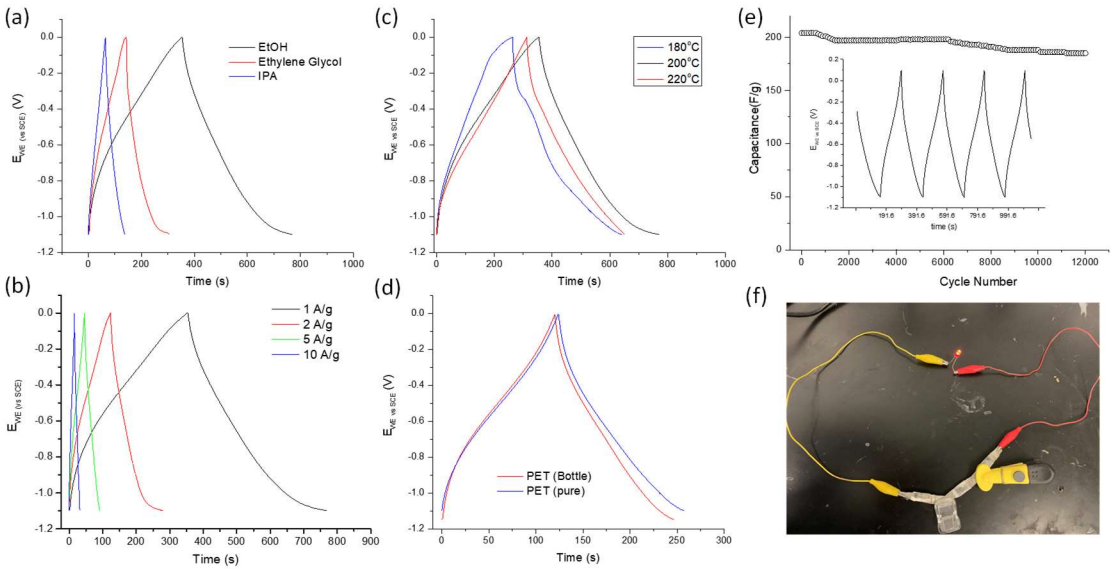

Figure 5-5: Galvanostatic charge-discharge curves of electrodes made of PBSCs in 6M KOH solution (a-d): (a) the electrochemical performance for PBSCs synthesized with ethanol, ethylene glycol, and IPA involvement at 1 A/g current density, (b) the performance of the PBSCs at different current densities from 1 A/g to 10 A/g, (c) the performance of the PBSCs synthesized at different temperatures (i.e., 180 $℃, 200\ ℃, and\ 220\ ℃$) at 1 A/g current density, and (d) the performance comparison between the pure PET and waste PET (at a current density of 2 A/g). (e) Cycling stability test at a current density of 2 A/g, and (f) demonstration of LED lit with assembled supercapacitor units.

To further reveal the electrochemical behaviors at the electrode-electrolyte interface, EIS tests were done on PBSC electrodes. A Nyquist plot was made to extract information on charge transfer, heterogeneity on electrode interfaces, derivation from ideal capacitor, and ion diffusion. As shown in **Figure 5-6a**, a typical curve with a

semicircle followed by a straight line is shown in the Nyquist diagrams of both a fresh PBSC electrode and the same one cycled after 12000 times. Their EIS patterns are almost identical, confirming our early observation of its superior long-term stability. Using Zview2 software, an equivalent circuit model that includes one solution resistor (R_1), one charge transfer resistor (R_2), one non-ideal constant phase element (CPE), and one Warburg element (W) was applied to fit the EIS data in each case (**Figure 5-6b**). The small values of R_1 indicate the low resistance in both the solution and at the electrode/electrolyte interface. The rapid charge transfer at the electrode/electrolyte interface is further confirmed by the small value of R_2. A total resistance of 2.544 **Ω** ± 13% for $R_1 + R_2$ indicates an overall excellent electrical conductivity of these $PBSC_{C2H5OH}$ electrodes. The large Warburg impedance value (W) reflects that ion diffusion on these PBSC electrodes is also effective. The "N" value of the CPE represents the surface heterogeneity of those electrodes to an ideal double-layer capacitor, and their slight deviation from 1.0 in $PBSC_{C2H5OH}$ electrodes reveals that, though it significantly increases the total host sites for ions, the presence of CQDs between the 2D carbon sheets does not add much tortuosity to the migration pathways of ions that is often seen in common porous materials. The values of R_2 and the N value of CPE also prove the electrochemical behaviors of our PBSC electrodes to be quite reversible. The minimal value variation of these elements after cycling suggests that the migration of ions and electrons did not change much after long-term cycling, which is consistent with our earlier observations of stability and excellent capacitance retention in these electrodes. In comparison, the EIS pattern in the Nyquist plot of the $PBSC_{HOC2H4OH}$ electrode shifts significantly (**Figure 5-6c**). Solution resistance and charge transfer resistance were found

to be larger for the $PBSC_{HOC2H4OH}$ electrode (4.233 Ω ± 6% for $R_1 + R_2$) than that made of $PBSC_{C2H5OH}$, as shown in **Figure 5-6c**. The electrode also derives more from an ideal, reversible capacitor based on the fitting parameters of its equivalent circuit model elements (e.g., R_2 and "N" value of CPE). These results confirm that $PBSC_{C2H5OH}$ electrodes show excellent electrical conductivity and consequently superior electrochemical performance.

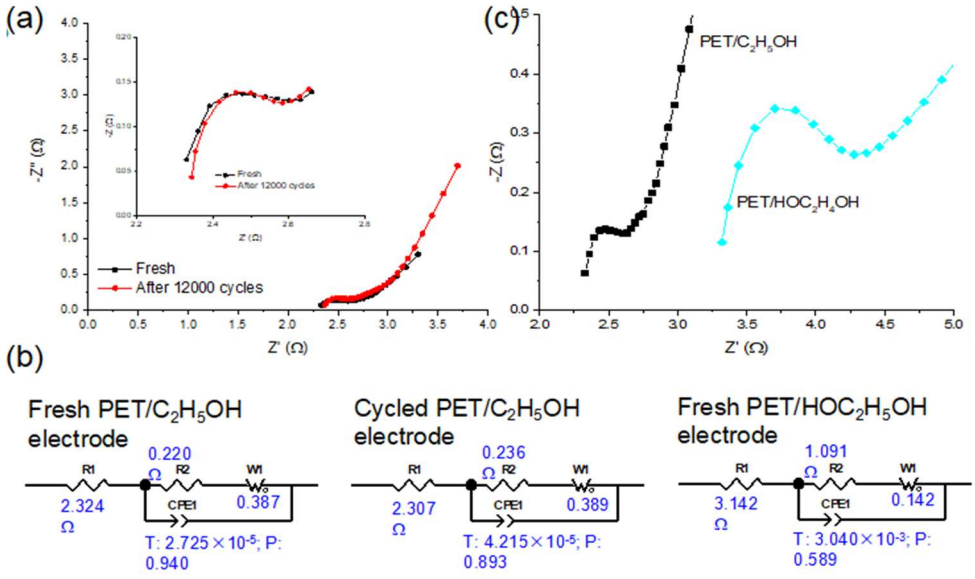

Figure 5-6: (a) Nyquist plots and (b) the corresponding fitting on an equivalent circuit of electrodes made of $PBSC_{C2H5OH}$: fresh and after 12000 cycles; (c) Nyquist plots of corresponding fitting on an equivalent circuit of electrodes made of fresh $PBSC_{C2H5OH}$ and $PBSC_{HOC2H4OH}$. The impedance spectrum was done with a voltage amplitude of 10mV and a frequency range of 0.01Hz ~ 100kHz.

5.4 Conclusions

Through hydrothermal reactions, PET plastics were successfully transformed into CQDs and conductive carbon sheets simultaneously, with the former well dispersed and intercalated in the latter, and modified as a connected ball-sheet conductive carbon network. With the help of nitric acid and ethanol, the original PET structure was

reformed into a condensed carbon skeleton packed with benzene rings and small functional clusters of -OH, -COOH, -NH, and O=C-NH< groups grafted on its surface. The received products showed strong photoluminescence under UV and near visible light excitation. More importantly, the unique carbon structure exhibits excellent electrical conductivity and superior capacity to host ions when assembled as a supercapacitor electrode. A specific capacity of 237 F/g and 198 F/g was achieved at the charge rate of 1 A/g and 2 A/g, respectively, which drops slowly when under an even higher charge rate. Excellent long-term cycling stability was also found with a 98% capacity retention percentage. As these accomplishments were seen in electrodes fashioned from real drinking bottle waste, this method of production provides increased economic incentive to upcycle plastic waste and create a close-loop clean energy utilization system.

CHAPTER 6

CONCLUSIONS AND FUTURE WORK

6.1 Conclusions

We introduced a new type of core-shell structure made of halloysite/sulfur composites to act as the cathode material of Li-S batteries. Inside this cathode, the short halloysite nanotubes were etched and assembled into halloysite cage clusters, forming nano-scale spaces which helped confine sulfur and inhibit the dissolution and migration of polysulfides in a liquid electrolyte solution. A layer of carbon film was added to the surface of the halloysite by carbonizing glucose to improve the overall conductivity of the composites. When used as the cathode of Li-S batteries, a specific capacity of 710 mAh/g was achieved at medium discharge rate. The cycle stability was also improved, with about 84% of the starting capacity retained after more than 250 cycles.

For the anode materials, a nanofiber-in-microfiber silicon/carbon composite was prepared via a unique coaxial electrospinning setup followed by carbonization of polymer fibers. In this silicon-rich composite, the outer PAN layer holds the fiber network structure so that it can be used as a three-dimensional current collector to promote lithium ion transport and charge transfer during charge and discharge processes. This PAN derived carbon shell is composed of an ultrathin carbon skin with rich silicon content, which protects the short silicon-rich nanofibers from pulverization and enhances their conductivity. The short silicon-rich nanofibers inside microfibers provide the majority of

Li^+ hosting sites, and, together with the mesoporous buffer spaces between them, form a conductive network to effectively alleviate the induced stress in silicon nanoparticles caused by the volume change during the lithiation and delithiation processes. This unique processing strategy provides a new and scalable way to manufacture high silicon content anodes with hybrid fiber composites that can effectively handle the volume change issues of silicon and the accompanied rapid decay of capacity during cycling.

To create supercapacitor electrodes, we used commercial drinking bottle waste to create a unique connected ball-sheet conductive carbon network through a one-step hydrothermal synthesis. With the addition of ethanol and nitric acid, the plastic waste was successfully transformed into highly conductive carbon sheets and carbon quantum dots with rich defects and high surface area. The newly formed carbon structure carried numerous -OH, -COOH, -NH and O=C-NH groups on the carbon quantum dots, and remaining unreacted PET was transformed into a layered carbon skeleton. Under the excitation of UV and near visible light, the products showed strong photoluminescence. Most importantly, this unique carbon structure showed excellent conductivity and a high specific capacity to host ions after being assembled into supercapacitor electrodes. At charging rates of 1 A/g and 2 A/g, the specific capacity reached 237 F/g and 198 F/g, respectively, which decreased very slowly even under higher cycling rates. The long-term cycle stability was found to be excellent, with a capacity retention rate of 98% at a current rate of 2 A/g.

6.2 Future Work

In Li-S batteries with halloysite/sulfur cathodes, halloysite accounts for a large proportion of the entire cathode weight. Due to the non-conductive nature of halloysite, a low specific capacity (calculated based on the electrode mass) is produced after assembling it into a battery. To solve this problem, we would suggest using halloysite only as a sacrificial template. After being coated with a glucose layer and carbonized, halloysites could most likely be etched away with a mixture of HF and HCl. This way only the outer carbon skin coated on the halloysite surface is left. The later formed composite electrode will therefore be much lighter but still carry the large hollow tubular structure of halloysites. The total pore volume will also be increased as the space previously taken up by halloysites is cleared and more sulfur can be loaded. Another feasible suggestion is pre-lithiation of the composite electrodes. During the first discharge (e.g., lithium insertion) step, electrolytes form a SEI layer on the electrode surface, resulting in large loss of the specific capacity of Li-S batteries in the first cycle. To help improve the first-cycle Coulomb efficiency of the cathode, the composite electrode material can be lithiated prior to the loading of sulfur. This could be achieved by dissolving a lithium salt like $Li@Li_2CO_3$ in solvent and then loading it into the etched halloysite lumen. This way the loss of lithium ions during the SEI formation can be reduced.

Of the modernly available anode materials, silicon seems the strongest competitor due to its ultra-high theoretical specific capacity. This theoretical specific capacity alone makes silicon worthy of scientific exploration. However, the volume change of silicon between the lithiation and delithiation processes is also the largest of all viable lithium

storage materials. The use of nanosized silicon was found to have less pronounced volume change and shorten the transport distance of lithium ions to solid silicon, resulting in a faster charging cycle. The nanofiber-in-microfiber structure is obtainable through electrospinning, fiber stabilization, and carbonization. It's possible that the encapsulated silicon oxide could be removed through hydrofluoric acid (HF) etching and simultaneously form a porous structure. If the structural stability of the fiber material remains unchanged, the porous structures could further effectively reduce the volume change during lithiation. The pre-lithiation method prescribed above may also be applied here to the silicon/carbon-based material, as the loss of surface-active lithium on the silicon anode is more serious than that of the cathode.

In the supercapacitor electrode study, the ball-sheet carbon structure was successfully manufactured with the PET from drinking bottle waste. It is worthwhile to consider the modification and different resources of the structured carbon to further increase its capacitance. It is possible that PET could be replaced by other plastics, such as PA, PP, PE, PMMA, etc. The differences in conductivity and porosity of different carbon chains are worthy of further investigation. Further, research which replaces ethanol, the second precursor in this ball-sheet carbon structure, with other small molecules like EDA, IPA, etc., should be done to investigate how different types and numbers of functional groups will affect the supercapacitor performance. The introduction of metal ions commonly used in supercapacitors such as Mn^{2+} and Co^{2+}, could further help to improve the redox reactions and should also be investigated. With better understanding of the transformation mechanisms of plastic waste into useful structured carbon, electrodes made of carbon materials produced from plastic wastes (like

those made in this simple one-step hydrothermal method) may further boost the power density and electrochemical performance of the assembled supercapacitors.

BIBLIOGRAPHY

Abdullayev, E. et al. “Enlargement of Halloysite Clay Nanotube Lumen by Selective Etching of Aluminum Oxide.” ACS Nano, vol. 6, 2012, pp. 7216-26.

Agubra, et al. “Composite Nanofibers as Advanced Materials for Li-ion, Li-O2 and Li-S Batteries.” Electrochimica Acta, vol 192, 2016, pp. 529-50.

Ahmad, et al. “Development in Energy Storage System for Electric Transportation: A Comprehensive Review.” Journal of Energy Storage, vol 43, 2021, 103153.

Ahmadi, Leila, et al. “Energy Efficiency of Li-ion Battery Packs Re-Used in Stationary Power Applications.” Sustainable Energy Technologies and Assessments, vol. 8, 2014, pp. 9-17.

Alas, Melis Ozge, et al. “Feeling the Power: Robust Supercapacitor from Nanostructured Conductive Polymer Fostered with Mn2+ and Carbon Dots.” Nanoscale, vol. 11, 2019, pp. 12804-16.

Armand, M., et al. “Building Better Batteries.” Nature, vol. 451, 2008, pp. 652-7.

Aurbach, D., et al. “On the Surface Chemical Aspects of Very High Energy Density, Rechargeable Li-Sulfur Batteries.” *Journal of The Electrochemical Society*, vol. 156, 2009, pp. 694-702.

Bao, Weizhai, et al. “Facile Synthesis of Graphene Oxide @ Mesoporous Carbon Hybrid Nanocomposites for Lithium Sulfur Battery.” Electrochimica Acta, vol. 127, 2014, pp. 342-8.

Barchasz, C., et al. “New Insights Into the Limiting Parameters of the Li/S Rechargeable Cell.” Journal of Power Sources, vol. 199, 2012, pp. 322-30.

Barriocanal, C., et al. “PET Recycling for the Modification of Precursors in Carbon Materials Manufacture.” Journal of Analytical and Applied Pyrolysis, vol. 73, Issue 1, 2005, pp. 45-51.

Bose, B.K., et al. “Global Warming: Energy, Environmental Pollution, and the Impact of Power Electronics.” IEEE Industrial Electronics Magazine, vol. 4, 2010, pp. 6-17.

Chae, et al. ”Performance and Cost of Materials for Lithium-Based Rechargeable Automotive Batteries.” Nat Energy, vol. 3, 2018, pp. 267–278.

Chan, C. K, et al. “Solution-Grown Silicon Nanowires for Lithium-Ion Battery Anodes.” ACS Nano, vol. 4, 2010, pp. 1443-50.

Chan, C. K., et al., “High-Performance Lithium Battery Anodes Using Silicon Nanowires.” Nature Nanotechnology, vol. 3, 2008, pp. 31-5.

Chang, Chia Chi, et al. “Si Electrodes for Li-Ion Batteries—A New Way to Look at an Old Problem.” Bulletin of the Chemical Society of Japan, vol. 94, 2021, pp. 454-62.

Chang, Chiachi, et al. “Effect of Carbon Dots on Supercapacitor Performance of Carbon Nanohorn/Conducting Polymer Composites.” *Bulletin of the Chemical Society of Japan*, vol. 94, Issue 2, 2021, pp. 454-62.

Chen, et al. “Applications of Lithium-Ion Batteries in Grid-Scale Energy Storage Systems.” Transactions of Tianjin University, vol. 26, 2020, pp/ 208–17.

Chen, et al. “Four-Layer Tin–Carbon Nanotube Yolk–Shell Materials for High-Performance Lithium-Ion Batteries.” *ChemSusChem*, vol 7, 2014, pp. 1407-14.

Chen, H., et al. “Monodispersed Sulfur Nanoparticles for Lithium-Sulfur Batteries with Theoretical Performance.” Nano Letters, vol. 15, 2015, pp. 798-802.

Cheng, Kl., et al. “Electrochemical Performance of a Nickel-Rich LiNi0.6Co0.2Mn0.2O2 Cathode Material for Lithium-Ion Batteries Under Different Cut-Off Voltages.” Int. J. Miner. Metall. Mater., vol. 24, 2017, pp. 342–51.

Choi, S., et al. “Challenges Facing Lithium Batteries and Electrical Double-Layer Capacitors.” Angewandte Chemie Int. Ed., vol. 51, 2012, pp. 9994-10024.

Chung, S. H., et al. “Current Status and Future Prospects of Metal-Sulfur Batteries.” Advanced Materials, vol. 31, 2019, p. 1901125.

Chung, Sheng-Heng, et al. “Electrochemically Stable Rechargeable Lithium-Sulfur Batteries with a Microporous Carbon Nanofiber Filter for Polysulfide.” Advanced Energy Materials, vol. 5, 2015, p. 1500738.

Demir, C.R, et al. “Hydrothermal Carbon Spheres Containing Silicon Nanoparticles: Synthesis and Lithium Storage Performance.” Chemical Communications, vol. 32, 2008, pp. 3759-61.

Deng, D., et al. “One-Step Synthesis of Polycrystalline Carbon Nanofibers with Periodic Dome-Shaped Interiors and their Reversible Lithium-Ion Storage Properties.” Chemistry of Materi*als*, vol. 19, 2007, pp. 4198-204.

Deng, F., Liu, H. et al. “Harnessing renewable energy in cloud datacenters: opportunities and challenges.” in IEEE Network, vol. 28, 2014, pp. 48-55. doi: 10.1109/MNET.2014.6724106.

Dorfler, S., et al. “High capacity vertical aligned carbon nanotube/sulfur composite cathodes for lithium-sulfur batteries.” Chem. Commun., vol. 48, 2012, pp. 4097-4099.

Endo, M., et al. “Recent development of carbon materials for Li ion batteries.” Carbon, vol. 38, 2000, pp.183-197.

Evers, S., et al. “New Approaches for High Energy Density Lithium-Sulfur Battery Cathodes.” Journal of Chemical Research, vol. 46, 2012, pp. 1135-1143.

Gao, J., et al. ‘Effects of Liquid Electrolytes on the Charge-Discharge Performance of Rechargeable Lithium/Sulfur Batteries: Electrochemical and in-Situ X-ray Absorption Spectroscopic Studies,” The Journal of Physical Chemistry C, vol. 115, 2011, pp. 25132-25137.

Genc, Rukan, et al. “High-Capacitance Hybrid Supercapacitor Based on Multi-Colored Fluorescent Carbon-Dots.” Nature, Article number: 11222, 2017.

Glotov, A., “Core/Shell Ruthenium-Halloysite Nanocatalysts for Hydrogenation of Phenol.” Ind. Eng. Journal of Chemical Research, vol. 56, 2017, pp. 14043-14052.

Guo, J., et al. “Lithium-sulfur battery cathode enabled by lithium-nitrile interaction.” Journal of the American Chemical Society, vol. 135, 2013, pp. 763-767.

Gupta, A., et al. “Designing Advanced Lithium-Based Batteries for Low-Temperature Conditions.” Adv. Energy Mater. vol. 10, 2020, 2001972.

Hao, L., et al. “Carbonaceous electrode materials for supercapacitors.” Advanced Materials, vol. 25, 2013, pp.3899-3904.

Hari, Raj, et al. “TiO2 shielded Si nano composite anode for high energy Li-ion batteries: the morphological and structural study of electrodes after charge-discharge process.” Electrochimica Acta, vol. 326, 2019, Article number: 134981.

Hari, Ral, et al. “TiO2 shielded Si nano composite anode for high energy Li-ion batteries: the morphological and structural study of electrodes after charge-discharge process.” Electrochimica Acta, vol. 326, 2019, Article number: 134981.

Helen, M., Reddy, M., et al.” Single step transformation of sulphur to Li2S2/Li2S in Li-S batteries.” Sci Rep vol. 5, 2015, 12146.

Huang, et al. “Synthesis and microwave absorption properties of coralloid core-shell structure NiS/Ni3S4@PPy@MoS2 nanowires.” Journal of Colloid and Interface Science, vol 599, 2021, pp. 262-270.

Huang, Ke-Jing, et al., "Hydrothermal synthesis of molybdenum disulfide nanosheets as supercapacitors electrode material." Electrochimica Acta, vol. 132, 2014, pp. 397-403.

Huang, Y. X., et al. "Sustainable activated carbon fiber from sawdust by reactivation for high-performance supercapacitors." Journal of Materials Science, vol. 52, 2016, pp. 478-488.

Hwang, T. H., Lee, Y.M., et al. "Electrospun Core-Shell Fibers for Robust Silicon Nanoparticle-Based Lithium-ion Battery Anodes." Nano. Lett., vol. 12, 2012, pp. 802-807.

Islam, M., et al. "Study on the electrochemical reaction mechanism of NiFe2O4 as a highperformance anode for Li-ion batteries." ACS Applied Materials & Interfaces, vol. 9, 2017, pp. 14833-14843.

Ito, K., "Novel Cross-Linking Concept of Polymer Network: Synthesis, Structure, and Properties of Slide-Ring Gels with Freely Movable Junctions." Polym J, vol. 39, 2007, pp. 489-499.

Jayaprakash, N., et al. "Porous Hollow Carbon@Sulfur Composites for High-Power Lithium-Sulfur Batteries." Chem. Int. Ed, vol. 123, 2011, pp. 6026-6030.

Jeong, G., et al. "Prospective materials and applications for Li secondary batteries." Energy. Environ Sci, vol. 4, 2011, pp.1986-2002.

Jia, H., et al. "Hierarchical porous silicon structures with extraordinary mechanical strength as high-performance lithium-ion battery anodes." Nat Commun, vol. 11, 2020, Article number: 1474.

Jiao, X., et al. "Highly Energy-Dissipative, Fast Self-Healing Binder for Stable Si Anode in Lithium-Ion Batteries." Adv. Funct. Mater. vol. 31, 2021, 2005699.

Jurewicz, K., et al. "Capacitance properties of ordered porous carbon materials prepared by a templating procedure." Journal of Physics and Chemistry of Solids, vol. 65, 2004, pp. 287- 293.

Kady, F. E., et al. "Laser scribing of high -performance and flexible graphene -based electrochemical capacitors." Science, vol. 335, 2012, pp. 1326-1330.

Kasavajjula, U., et al. "Appleby, Nano- and bulk-silicon-based insertion anodes for lithium-ion secondary cells." Journal of Power Resource., vol. 163, 2007, pp.1003-1039.

Kerr, P. F., "Formation and Occurrence of Clay Minerals." Clay and Clay Miner., vol. 1, 1952, pp. 19-32.

Kim, C., et al. “Electrochemical characterization of electrospun activated carbon nanofibres as an electrode in supercapacitors.” Journal of Power Resource. vol. 142, 2004, pp. 382-388.

Kim, Do Kyung, “Spinel LiMn2O4 Nanorods as Lithium Ion Battery Cathodes.” Nano Lett., vol. 8, 2008, pp. 3948-3952.

Kim, H.J., et al. “Controlled Prelithiation of Silicon Monoxide for High Performance Lithium-Ion Rechargeable Full Cells.” Nano Letters, vol. 16, 2016, pp. 282-285.

Kim, Kyoung Hwan, et al. “Sulfur infiltrated mesoporous graphene-silica composite as a polysulfide retaining cathode material for lithium-sulfur batteries.” Carbon, vol. 69, 2014, pp. 543-551.

Kim, S., et al. “Silicon-Rich Carbon Hybrid Nanofibers from Water-Based Spinning: The Synergy Between Silicon and Carbon for Li-ion Battery Anode Application.” Chem ElectroChem, vol. 1, 2014, pp. 220-226.

Lazzara, G, et al. “An assembly of organic-inorganic composites using halloysite clay nanotubes.” Curr. Opin. Colloid Interface Sci., vol. 35, 2018, pp. 42-50.

Lee, J.T., et al. “Sulfur-infiltrated micro-and mesoporous silicon carbide-derived carbon cathode for high-performance lithium sulfur batteries.” Advanced Materials, vol. 25, 2013, pp. 4573-4579.

Li, et al. “Electrospun hollow nanofibers for advanced secondary batteries.” Nano Energy, vol 39,2017, pp. 111-139.

Li, G., et al. “Self-formed hybrid interphase layer on lithium metal for high-performance lithium-sulfur batteries.” ACS Nano, vol. 12, 2018, pp. 1500-1507.

Li, H., et al. “A High Capacity NanoSi Composite Anode Material for Lithium Rechargeable Batteries.” Electrochem Solid-State Lett, vol. 2, 1999, pp.547-549.

Li, J., et al. “Ultrathin mesoporous Co3O4 nanosheet arrays for high-performance lithium-ion batteries.” ACS Omega, vol. 3, 2018, pp. 1675-1683

Li, S., et al. “Developing High-Performance Lithium Metal Anode in Liquid Electrolytes: Challenges and Progress” Adv. Mater. vol. 30, 2018, 1706375.

Li, Y., et al. “Structure control and performance improvement of carbon nanofibers containing a dispersion of silicon nanoparticles for energy storage.” Carbon, vol. 51, 2013, pp. 185-194.

Li, Z., et al. “Status and prospects in sulfur-carbon composites as cathode materials for rechargeable lithium-sulfur batteries.” Carbon, vol. 92, 2015, pp. 41-63.

Liang, C., et al. “Hierarchically structured sulfur/carbon nanocomposite material for high-energy lithium battery.” Chemistry of Materials, vol. 21, 2009, pp. 4724-4730.

Liang, Xiao, et al. “A nano-structured and highly ordered polypyrrole-sulfur cathode for lithium-sulfur batteries.” Journal of power resource, vol. 196, Issue 16, 2011, pp. 6951-6955.

Lin, Y., et al. “Natural halloysite nano-clay electrolyte for advanced all-solid-state lithium-sulfur batteries.” J. Nano Energy, vol. 31, 2017, pp. 478-485.

Liu, Lei, et al. “High-performance all-inorganic portable electrochromic Li-ion hybrid supercapacitors toward safe and smart energy storage.” Energy Storage Materials, vol. 33, 2020, pp. 258-267.

Liu, M., et al. “Functionalized halloysite nanotube by chitosan grafting for drug delivery of curcumin to achieve enhanced anticancer efficacy.” J. Chemistry of Materials, B vol. 4, 2016, pp. 2253-2263.

Liu, N., Wu, H., et al. “A Yolk-Shell Design for Stabilized and Scalable Li-Ion Battery Alloy Anodes.” Nano Lett, vol. 12, 2012, pp. 3315-3321.

Liu, Tingting, et al. “Synthesis of MnO2-graphene composites with enhanced supercapacitive performance via pulse electrodeposition under supergravity field.” Journal of Solid-State Chemistry, vol. 215, 2014, pp. 160-166.

Liu, Y., et al. “Biomass-swelling assisted synthesis of hierarchical porous carbon fibers for supercapacitor electrodes.” ACS Applied Materials & Interfaces, vol. 8, 2016, pp. 28283-28290.

Lun, P., et al. “Enhanced ionic conductivity in halloysite nanotube-poly(vinylidene fluoride) electrolytes for solid-state lithium-ion batteries.” RSC Adv., vol. 8, 2018, pp. 34232-34240.

Luo, W., et al.” Surface and Interface Engineering of Silicon-Based Anode Materials for Lithium-Ion Batteries.” Adv. Energy Mater., vol 7, 2017, pp. 1701083.

Luo, Xianyou Luo, et al. “A review of charge storage in porous carbon-based supercapacitors.” New Carbon Materials, Vol. 36, 2021, pp. 49-68.

Lvov, Y., et al. “Halloysite clay nanotubes for loading and sustained release of functional compounds.” Advanced Materials, vol. 28, 2016, pp. 1227-1250.

Ma, Lin, et al. “Nanomaterials: Science and applications in the lithium-sulfur battery.” Nano Today, vol. 10, 2015, pp. 315-338.

Ma, Y., et al. “Biomass-derived dendritic-like porous carbon aerogels for supercapacitors.” Electrochimica Acta, vol. 210, 2016, pp. 897-904.

Magasinski, A, et al. “High-performance lithium-ion anodes using a hierarchical bottom-up approach.” Nat Mater, vol. 9, 2010, pp. 353-358.

Manthiram, A., et al. “Rechargeable lithium-sulfur batteries,” Chem. Rev., vol. 114, 2014, pp. 11751-11787.

Manthiram, Arumugam, et al. “In Charge of the World: Electrochemical Energy Storage.” J. Phys. Chem. Lett. vol. 4, 2013, pp. 1295-1297.

Mao, Lu, et al. “Surfactant-stabilized graphene/polyaniline nanofiber composites for high performance supercapacitor electrode.” J. Chemistry of Materials, 2012, vol. 22, pp. 80-85.

Marichi, R. B., et al. “Efficient, Sustainable, and Clean Energy Storage in Supercapacitors Using Biomass-Derived Carbon Materials.” Handbook of Ecomaterials Springer, Cham. 2017, pp. 1-26.

Mehtab, Tahira, et al. “Metal-organic frameworks for energy storage devices: Batteries and supercapacitors.” Journal of Energy Storage, vol. 21, 2019, pp. 632-646.

Mikhaylik, Y. V., et al. “Polysulfide shuttle study in the Li/S battery system,” Soc., vol. 151, 2004, pp. 1969-1976.

Mohamad, K., et al. “Fabrication and electrochemical characterization of graphene-oxide supercapacitor electrodes with activated carbon current collectors on graphite substrates.” Computers & Electrical Engineering, vol. 85, 2020, pp. 106678.

Moses, Anthony W., “Surface properties of LiCoO2, LiNiO2 and LiNi1−xCoxO2.” Applied Surface Science, vol. 253, 2007, pp. 4782-4791.

Nava, Rocío, et al. “Centrifugal Spinning: An Alternative for Large Scale Production of Silicon-Carbon Composite Nanofibers for Lithium Ion Battery Anodes.” ACS Appl. Mater. Interfaces 2016, vol. 8, pp. 29365-29372.

Nelson, Paul A., et al. “Modeling the Performance and Cost of Lithium-Ion Batteries for Electric-Drive Vehicles.” Third Edition. United States: N. p., 2019.

Nikita, V,. et al. “sp2-sp3-Hybridized Atomic Domains Determine Optical Features of Carbon Dots.” ACS Nano,vol. 13, 2019, pp. 10737-10744.

Owoseni, O., et al. “Tuning the wettability of halloysite clay nanotubes by surface carbonization for optimal emulsion stabilization.” Langmuir, vol. 31, 2015, pp. 13700-13707.

Pandolfo, G., et al. “Carbon properties and their role in supercapacitors.” Journal of power sources, vol. 157, 2006, pp. 11-27.

Park, C. M., et al. “Li-alloy based anode materials for Li secondary batteries.” Chem. Soc. Rev., vol. 39, 2010, pp.3115-3141.

Placke, et al.” Lithium ion, lithium metal, and alternative rechargeable battery technologies: the odyssey for high energy density.” J Solid State Electrochem, vol 21, 2017, 1939–1964.

Ravindran, Madhurambal, et al. “Thermal, UV and FTIR spectral studies in alkali metal cinnamates.” Journal of Thermal Analysis and Calorimetry, vol. 100. 2010, pp. 811-815.

Ravindranath, R. A., et al. “Polyethylene terephthalate—I. Chemistry, thermodynamics and transport properties.” Chemical Engineering Science, vol. 41, Issue 9, 1986, pp. 2197-2214,

Raza, Nadeem, et al. “Recent advances in bimetallic metal-organic framework as a potential candidate for supercapacitor electrode material.” Coordination Chemistry Reviews, vol. 430, 2021, Article number: 213660.

Ryu, Hoon-Hee, et al.” Reducing cobalt from lithium-ion batteries for the electric vehicle era.” Energy and Environmental Science, vol. 14, 2021, pp. 844-852.

Salanne, M., et al. “Efficient storage mechanisms for building better supercapacitors.” Nature Energy, vol. 1, 2016, pp. 16070.

Saliger, R. et al. “High surface area carbon aerogels for supercapacitors.” Journal of Non-Crystalline Solids, vol. 225, 1998, pp. 81-85.

Shacklette, L.W., et al. “Secondary batteries with electroactive polymer electrodes.”Synthetic Metals, Vol. 18, 1987, pp. 611-618.

Shukla, A. K., et al. “Electrochemical Supercapacitors: Energy Storage beyond Batteries.” Current Science, vol. 79, no. 12, Temporary Publisher, 2000, pp. 1656-1661.

Sliwak, A., et al. “Nitrogen-doped reduced graphene oxide as electrode material for high rate supercapacitors.” Applied Surface Science, vol. 399. 2016, pp. 265-271.

Song, J. X., et al. “Advanced sulfur cathode enabled by highly crumpled nitrogen-doped graphene sheets for high-energy-density lithium-sulfur batteries.” Nano Letters, vol. 16, 2016, pp. 864.

Song, J. X., et al. “Strong lithium polysulfide chemisorption on electroactive sites of nitrogen-doped carbon composites for high-performance lithium-sulfur battery cathodes.” Angewandte Chemie. Int., Ed. vol. 54, 2015, pp. 4325.

Su, Y. S., et al. “A new approach to improve cycle performance of rechargeable lithium-sulfur batteries by inserting a free-standing MWCNT interlayer.” Chem. Commun., vol. 48, 2012, pp. 8817-8819.

Su, Y. S., et al. “Lithium-sulphur batteries with a microporous carbon paper as a bifunctional interlayer.” Nature Communications, vol. 3, 2012, pp. 1166.

Sun, Peng., et al. “Ultrathin MnO2 nanoflakes deposited on carbon nanotube networks for symmetrical supercapacitors with enhanced performance.” Journal of Power Resource., vol. 341,2017, pp. 27-35.

Sun, Z., et al. “Sandwich-structured graphite-metallic silicon@C nanocomposites for Li-ion batteries.” Electrochimica Acta, vol. 191, 2016, pp. 306.

Szczech, J. R., et al. “Nanostructured silicon for high-capacity lithium battery anodes.” Energy Environ. Sci., vol. 4, 2011, pp.56-72.

Tan, G., et al. “Burning lithium in CS2 for high-performing compact Li2S-graphene nanocapsules for Li-S batteries.” Nature Energy, vol. 2, 2017, Article number: 17090.

Tan, Kangmiao, et al. “Empowering smart grid: A comprehensive review of energy storage technology and application with renewable energy integration.” Journal of Energy Storage, vol. 39, 2021, Article number: 102591.

Tarascon, J. M., et al. “Issues and challenges facing rechargeable lithium batteries.” Nature, vol. 414, 2001, pp.359-367.

Thackeray, M., et al. “Electrical energy storage for transportation—approaching the limits of, and going beyond, lithium-ion batteries.” Energy Environ. Sci., vol. 5, 2012, pp. 7854-7863.

Thackeray, M., et al. “Electrical energy storage for transportation—approaching the limits of, and going beyond, lithium-ion batteries.” Energy Environ. Sci., vol. 5, 2012, pp.7854-7863.

Thathiana, Benavides Pahola, et al. “Exploring Comparative Energy and Environmental Benefits of Virgin, Recycled, and Bio-Derived PET Bottles.” ACS Sustainable Chemistry & Engineering, vol. 6, 2018, pp. 9725-9733.

U.S. Environmental Protection Agency Plastics: Material-Specific Data.

Veerakumar, Pitchaimani, et al. “Research Progress on Porous Carbon Supported Metal/Metal Oxide Nanomaterials for Supercapacitor Electrode Applications.” Ind. Eng. Chem. Res. vol. 59, 2020, pp. 6347-6374.

Wang, C., et al. “Sulfur-amine chemistry-based synthesis of multi-walled carbon nanotube-sulfur composites for high performance Li-S batteries.” Chem. Commun., vol. 50, 2014, pp. 1202-1204.

Wang, D., et al. “Carbon-sulfur composites for Li-S batteries: status and prospects.” Chemistry of Materials, vol. 1, 2013, pp. 9382-9394.

Wang, et al. “Highly uniform silicon nanoparticle/porous carbon nanofiber hybrids towards free-standing high-performance anodes for lithium-ion batteries.” Carbon, vol 82, 2015, pp. 337-345.

Wang, H., et al. “Graphene-wrapped sulfur particles as a rechargeable lithium-sulfur battery cathode material with high capacity and cycling stability.” Nano Letters, vol. 11, 2011, pp. 2644-2647.

Wang, H., Yang Y., et al. “Graphene-w rapped sulfur particles as a rechargeable lithium-sulfur battery cathode material with high capacity and cycling st ability.” J. Nano Lett, vol. 11, 2011, pp. 2 644- 2 647.

Wang, Heng, et al. “A novel zinc-ion hybrid supercapacitor for long-life and low-cost energy storage applications.” Energy Storage Materials, vol. 13, 2018, pp. 1-7.

Wang, J., et al. “A novel conductive polymer-sulfur composite cathode material for rechargeable lithium batteries.” Advanced Materials, vol. 14, 2002, pp. 963-965.

Wang, J.Z., Lu, L., et al. “Sulfur-graphene composite for rechargeable lithium batteries.” Journal of Power Resource., vol. 196, 2011, pp. 7030- 7034.

Wang, Y., et al. “Foamed mesoporous carbon/silicon composite nanofiber anode for lithium ion batteries.” Journal of Power Resource., 2015, vol. 281, pp. 285-292.

Weimin, Du, et al. “Designing synthesis of porous biomass carbon from wheat straw and the functionalizing application in flexible, all-solid-state supercapacitors.” Journal of Alloys and Compounds, vol. 797, 2019, pp. 1031-1040.

WeiSeh, Z., et al. “Sulphur-TiO2 yolk-shell nanoarchitecture with internal void space for long-cycle lithium-sulphur batteries.” Nature Communications, vol. 4, 2013, pp. 1331.

Wu, F., et al. “Sulfur-polythiophen e composite cathode materials f or rechargeable lithium batteries.” Electrochem Solid-St at e Lett, vol. 13, 2010, pp. A29- A31.

Wu, H., et al. “Designing nanostructured Si anodes for high energy lithium ion batteries.” Nano Today, vol. 7, 2012, pp. 414-429.

Wu, H., et al. “Engineering empty space between Si nanoparticles for lithium-ion battery anodes.”Nano Lett, vol. 12, 2012, pp. 904-909.

Xia, Chunlei , et al. “Evolution and Synthesis of Carbon Dots: From Carbon Dots to Carbonized Polymer Dots.” Advanced Science, vol. 6, 2019, pp. 1901316

Xie J., et al. “Comparing One- and Two-Dimensional Heteronanostructures as Si-Based Li Ion Battery Anode Material.” ACS Nano, vol. 5, 2011, pp. 9225-9231.

Xin, S., et al. “Smaller sulfur molecules promise better lithium-sulfur batteries.” Journal of the American Chemical Society, vol. 134, 2012, pp. 18510-18513.

Xu, W. L., et al. “Composite Silicon Nanowire Anodes for Secondary Lithium-Ion Cells.” J. Electrochem Soc,vol. 157, 2010, pp. 41-45.

Xu, X., et al. “Spindle-like mesoporous α-Fe2O3 anode material prepared from MOF template for high-rate lithium batteries.” Nano Letters, vol. 12, 2012, pp.4988-4991.

Yamin, H., et al. “Lithium sulfur battery: oxidation/reduction mechanisms of polysulfides in THF solutions,” J. Electrochem. Soc., vol. 135, 1988, pp. 1045-1048.

Yang, W., et al. “Ferrous sulfide-assisted hollow carbon spheres as sulfur host for advanced lithium-sulfur batteries.” Chem. Eng. J., vol. 326, 2017, pp. 1040-1047.

Ye, et al.” Engineering of Yolk/Core–Shell Structured Nanoreactors for Thermal Hydrogenations.” Small vol 17, 2021, pp.1906250.

Yin Lihong, et al. “3-dimensional hierarchical porous activated carbon derived from coconut fibers with high-rate performance for symmetric supercapacitors.” Materials & Design, vol. 111, 2016, pp. 44-50.

Yin, L., et al. “A novel pyrolyzed polyacrylonitrile- sulfur@MWCNT composite cathode material for high-rate rechargeable lithium/ sulfur batteries.” J. Mater Chem, vol. 21, 2011, pp. 6807- 6810.

Yoshio, M., et al. “Electrochemical behaviors of silicon-based anode materials.” Journal of Electrochemical Society, vol. 149, 2002, pp. 1598.

Yu, N., et al. “High-performance fiber-shaped all-solid-state asymmetric supercapacitors based on ultrathin MnO2 nanosheet/carbon fiber cathodes for wearable electronics.” Advanced Energy Materials, vol. 6, 2016, Article number: 1501458

Zhang, et al.” Challenges and Recent Progress on Silicon-Based Anode Materials for Next-Generation Lithium-Ion Batteries.” Small Struct., vol 2, 2020, pp.2100009.

Zhang, L. L., et al. “Carbon-based materials as supercapacitor electrodes.” Chemical Society Reviews, vol. 38, 2009, pp. 2520-2531.

Zhang, Miao, et al. “Latest development of nanostructured Si/C materials for lithium anode studies and applications.” Energy Storage Materials, vol. 4, 2016, pp. 1-14.

Zhang, Wei-Jun, et al. “Structure and performance of LiFePO4 cathode materials: A review.” Journal of Power Resource., vol. 196, 2011, pp. 2962-2970.

Zhang, X. W., et al. “Electrochemical performance of lithium ion battery, nano-silicon-based, disordered carbon composite anodes with different microstructures.” Journal of Power Resource.,vol. 125, 2004, pp.206-213.

Zhang, Xiaosong, et al. “A facile method to fabricate a porous Si/C composite with excellent cycling stability for use as the anode in a lithium ion battery.” Chemical Communications, vol. 55, 2019, pp. 13438-13441.

Zhang, Y., et al. “Composite anode material of silicon/graphite/carbon nanotubes for Li-ion batteries.” Electrochimica Acte, vol. 51, 2006, pp. 994-5000.

Zhang, Y., et al. “Functionalized activated carbon prepared form petroleum coke with high-rate supercapacitive performance.” Journal of Materials Research, vol. 31, 2016, pp. 3723-3730.

Zhang, Yin, et al.” Functionalization-assistant ball milling towards Si/graphene anodes in high performance Li-ion batteries.” Carbon,vol. 181, 2021, pp. 300-309.

Zhang, Yong, et al. “Progress of electrochemical capacitor electrode materials: A review.” International Journal of Hydrogen Energy, vol. 34, Issue 11, 2009, pp. 4889-4899.

Zhao, H., et al. “Chain-Elongated Ionic Liquid Electrolytes for Low Self-Discharge All-Solid-State Supercapacitors at High Temperature.” ChemSusChem, vol. 14, 2021, Article number 3895.

Zheng, G., et al. “Hollow carbon nanofiber-encapsulated sulfur cathodes for high specific capacity rechargeable lithium batteries.” Nano Letters, vol. 11, 2011, pp. 4462-4467.

Zhi, M, et al. “Nanostructured carbon-metal oxide composite electrodes for supercapacitors: A review.” Nanoscale, vol. 5, 2013, pp. 72.

Zhou, J., et al. “Biomass-Derived Carbon Materials for High-Performance Supercapacitors: Current Status and Perspective.” Electrochem. Energ. vol. 4, 2021, pp. 219-248.

Zhou, Nan, et al. “Interconnected structure Si@TiO2 -B/CNTs composite anode applied for high-energy lithium ion batteries.” Applied Surface Science, vol. 500, 2020, Article number: 144026.